Graduate Theses and Dissertations

Graduate School

2009

Baseband receiver algorithms for 4G co-channel femtocells

Mustafa Sahin
University of South Florida

Follow this and additional works at: http://scholarcommons.usf.edu/etd

Part of the American Studies Commons

www.manaraa.com

Baseband Receiver Algorithms for 4G Co-Channel Femtocells

by

Mustafa Emin Şahin

A dissertation submitted in partial fulfillment
of the requirements for the degree of
Doctor of Philosophy
Department of Electrical Engineering
College of Engineering
University of South Florida

Major Professor: Hüseyin Arslan, Ph.D.
Richard D. Gitlin, Sc.D.
Dmitry Goldgof, Ph.D.
Ravi Sankar, Ph.D.
Stephen Suen, Ph.D.

Date of Approval:
November 4, 2009

Keywords: Cognitive radio, energy detection, inter-carrier interference, iterative
cancellation, MIMO, OFDMA, opportunity detection, user separation.

DEDICATION

To my beloved wife *Müberra*

ACKNOWLEDGEMENTS

First, I would like to thank my advisor Dr. Hüseyin Arslan for his guidance, encouragement, and continuous support throughout my Ph.D. studies. It has been a privilege to have the opportunity to do research as a member of Dr. Arslan's research group. I wish to thank Dr. Richard D. Gitlin, Dr. Dmitry Goldgof, Dr. Ravi Sankar, and Dr. Stephen Suen for serving in my committee and for offering their valuable feedback. I hope to be able to benefit from their profound knowledge and experience in the future, as well. I also want to thank Dr. Venkat Bhethanabotla for chairing my defense.

I am grateful to Dr. Ismail Güvenç not only for advising me throughout our two-year collaboration with NTT DOCOMO, but also for his sincere friendship. I also want to acknowledge Dr. Fujio Watanabe and Dr. Moo-Ryong Jeong from DOCOMO USA Labs for their support and their direct contributions to this dissertation.

I owe much to my friends Dr. Hisham Mahmoud, Dr. Serhan Yarkan, Dr. Hasari Çelebi, Dr. Tevfik Yücek, Ibrahim Demirdöğen, Hasan Basri Çelebi, Abdullah Hatahet, Murad Khalid, Omar Zakaria, Ismail Bütün, Sabih Güzelgöz, Sadia Ahmed, Ali Görçin, Evren Terzi, Dr. Bahattin Karakaya, Dr. Celal Çeken, Ali Rıza Ekti, Özgür Yürür, Çağatay Talay, and Hazar Akı. We shared so many things with them over the years that we spent together. They also taught me so many virtues. Sincere friendship to start with, unselfishness, tolerance, and helpfulness. I am grateful to them for making me a better person.

I also want to express my gratitude to my friends in the Turkish community in Tampa, FL, especially to Salih Erdem, Şener Gültekin, Erdoğan Bulut, Levent Dağıstanlı, Erdem Önsal, and Salim Erdem for their support to us, students, whenever we need it. Graduate student life would be much less bearable if they were not there.

My sincere appreciation goes to my parents and my elder sister for bringing me up, leading me to the right direction, and always encouraging me for pursuing higher degrees. It is not possible to thank them enough, but I want them to know that I will be grateful to them throughout my life. I also want to thank my parents in law as well as my brother in law, Ahmet, for their kindness to me and their continuous support.

Last, but by no means least, my deepest gratitude goes to my wife, Müberra, for her love, all the sacrifices she made, her firm support, her vast patience, and her steady encouragement for more than five years now. If she did not have such a deep understanding and tolerance for the hardships of being the wife of a Ph.D. student, I could not even try to obtain this degree. I want to thank her from my heart for everything she has been doing.

TABLE OF CONTENTS

i

iv

LIST OF TABLES

LIST OF FIGURES

vii

LIST OF ACRONYMS

3G	3rd generation
3GPP	3rd Generation Partnership Project
4G	4th generation
AWGN	additive white Gaussian noise
BER	bit error rate
BPSK	binary phase shift keying
BS	base station
CCI	co-channel interference
CDMA	code division multiple access
CFO	carrier frequency offset
CP	cyclic prefix
CR	cognitive radio
CSG	closed-subscriber-group
DAC	digital to analog converter
DFT	discrete Fourier transform
DL	downlink
fBS	femtocell base station
FDMA	frequency division multiple accessing
FFT	fast Fourier transform
fMS	femtocell mobile station
GA	Gaussian approximation
ICI	inter-carrier interference
IEEE	Institute of Electrical and Electronics Engineers

IF	intermediate frequency
ITU	International Telecommunication Union
LMMSE	linear minimum mean-square error
LMS	least-mean-square
LTE	long term evolution
mBS	macrocell base station
MC	multicarrier
MIMO	multiple-input multiple-Output
ML	maximum likelihood
MLSE	maximum likelihood sequence estimation
mMS	macrocell mobile station
MP	multipath
MS	mobile station
NB	narrowband
NBI	narrow-band interference
OFDMA	orthogonal frequency division multiple access
PAPR	peak-to-average-power ratio
PFA	probability of false alarm
PHY	physical layer
PMD	probability of missed detections
PN	pseudo noise
PUSC	partially used sub-channeling
QPSK	quadrature phase shift keying
RF	radio frequency
ROC	receiver operating characteristic
RTD	round trip delay
SAS	subcarrier assignment scheme

SC-FDMA	single carrier frequency division multiple accessing
SER	symbol error rate
SINR	signal-to-interference-plus-noise ratio
SIR	signal-to-interference ratio
SISO	single-input single-output
SM	spatial multiplexing
SNR	signal-to-noise ratio
STC	space time coding
STTD	space-time transmit diversity
SU	secondary user
TDMA	time division multiple access
UL	uplink
VSA	vector signal analyzer
W-CDMA	wideband code division multiple access
WiMAX	worldwide interoperability for microwave access
WLAN	wireless local area network

BASEBAND RECEIVER ALGORITHMS FOR 4G CO-CHANNEL FEMTOCELLS

Mustafa Emin Şahin

ABSTRACT

The growing interest for high data rate wireless communications over the last few decades gave rise to the emergence of a number of wideband wireless systems. The resulting scarcity of frequency spectrum has been forcing wireless system designers to develop methods that will push the spectral efficiency to its limit. One such method is to have multiple systems utilize the same spectrum by allowing some unavoidable interference to occur between them. The idea of co-channel systems is tested in the industrial, scientific and medical (ISM) bands and it is found to be a very beneficial approach. Therefore, it can be foreseen that co-channel systems might be a potential solution to the growing spectral crowding problem.

Besides the systems that are designed to be co-channel, it is sometimes also possible to encounter that multiple systems occupy the same band undesirably. This kind of unintentional co-channel system scenarios might occur especially due to the dense re-use of available frequency bands. Another reason for unwanted co-channel usage might be the coexistence of third generation (3G) and fourth generation (4G) systems. Since 4G systems will probably be targeting to use the same frequency bands as their 3G counterparts, and since the transition from 3G to 4G will take some time, unintentional co-channel scenarios might be observed between the 3G and 4G systems.

This dissertation consists of baseband receiver algorithms for OFDMA-based systems that target at handling the potential co-channel interference (CCI) in various co-channel system scenarios. Three CCI avoidance and two CCI cancellation algorithms are proposed that can be applied to intentional and unintentional co-channel systems. Femtocells, which have recently been introduced as a new class of personal-use base stations that can coexist with macrocell networks in a shared spectrum manner, might constitute an appropriate example for both types of co-channel systems. Therefore, they are considered to be one of the co-existing systems in most of the algorithms presented.

CHAPTER 1

INTRODUCTION

Over the last two decades there has been an incredible increase in the demand for wireless services in the entire world. This increase lead to the emergence of a number of advanced wireless systems whose common goal is to provide a very high data rate to countless users, which requires an enormous capacity. Since the most basic way of increasing the capacity of a communication system is to increase the bandwidth, traditionally, all new emerging wireless technologies have been demanding wider bands than the existing ones. However, the frequency spectrum is a natural resource and like all other natural resources, it is not unlimited. Therefore, the crowding in the spectrum is a significant problem that is threatening the growth of wireless communications.

In order to enable a number of users to utilize a given frequency band, modern wireless systems employ multiple accessing methods. In time division multiple accessing (TDMA), users are allowed to access the spectrum at pre-determined time slots. In frequency division multiple accessing (FDMA), the available spectrum is split into a number of frequency blocks where each user is allocated one or more block. In orthogonal FDMA (OFDMA), time-frequency blocks are employed, which are made as compact as possible while maintaining the orthogonality between them, in order to maximize the efficiency of spectrum usage. In code division multiple accessing (CDMA), each user is assigned a different pseudo-noise type of code that is multiplied with the transmitted data to spread it to the available band. Multiplication with the same code in the receiver part enables separation of multiple user signals from each other. Another domain that is exploited to allow utilization of the same frequency band is the power domain. By limiting the signal powers of transmitters to a certain level, frequency reuse concept can be realized, where the same chunk of frequencies

1

are used over and over at tightly parceled cells. A final way of enabling multiple users to use the same spectrum is realized in space domain through beamforming. By employing antenna arrays rather than a single antenna, transmit and/or receive signal beams are formed that make it possible to use a given band repeatedly for users located within the same area.

The ever growing need for spectrum has been forcing wireless system designers to choose more aggressive system parameters such as narrower OFDMA subcarrier spacings, longer CDMA codes, and frequency reuse factors closer to 1. Imposing this kind of aggressive parameters on a system might result in various forms of interference such as co-channel, adjacent channel, and multi-user interferences. However, practical system applications so far have revealed that allowing interference up to a certain level helps increasing the overall efficiency of spectrum usage.

In an analogy to tolerating some interference for improving the spectral efficiency in multi-users systems, multiple systems can be made co-channel to maximize the spectral efficiency while allowing potential interference. This is the case in the industrial, scientific and medical (ISM) bands, where various different technologies such as wireless local area network (WLAN) routers, cordless phones, and microwave ovens operate. Another example for intentional use of the same spectrum by multiple sources is the multiple input multiple output (MIMO) systems. Although this kind of a system description may sound unusual for MIMO systems, since every separate transmitter branch transmits different data using the same band, a MIMO system is indeed a co-channel system on its own.

Apart from the systems that are designed to be co-channel, there are situations where more than one system's signals exist in the same band unintentionally. This is the case, for instance, in cellular systems in which all cells use the same frequency band, i.e. the frequency reuse factor is equal to 1. In such a case, at locations close to the cell borders, it is possible to observe interfering signals from multiple sources. Another potential scenario for unwanted coexistence in the same band might occur during the transition from the third generation (3G) to the fourth generation (4G) systems. Since it will take some time until
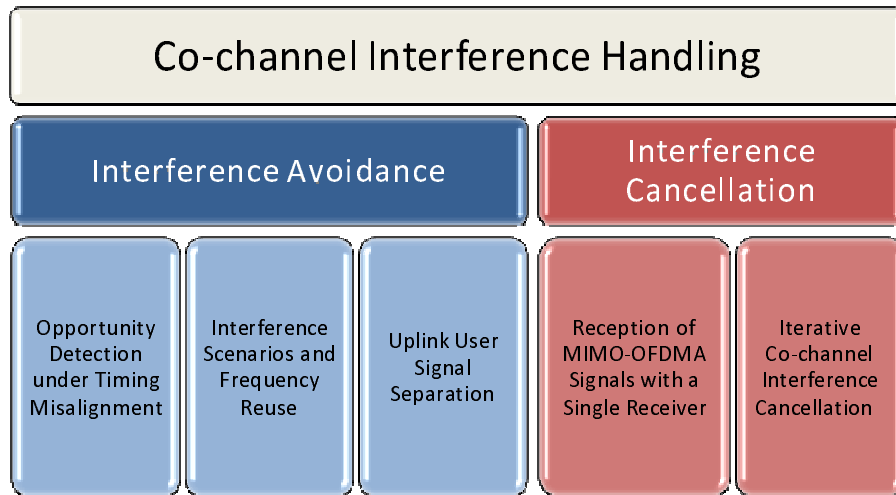
Figure 1.1 Structure of the dissertation.

all the 3G systems are substituted by 4G systems, it is expected to observe 3G and 4G systems' signals interfere with each other. The number of examples for unintentional co-channel system scenarios can be increased. The common feature of most of these scenarios is that they are more random in nature compared to the intentional co-channel systems, and hence, to deal with them is equivalently more challenging.

The baseband receiver algorithms proposed in this dissertation aim at handling the co-channel interference (CCI) that might occur both in intentional and in unintentional co-channel system scenarios. These algorithms can be classified as interference avoidance and interference cancellation methods as illustrated in Fig 1.1. In most of the presented algorithms, one of the co-channel systems is exemplified by a femtocell network. Femtocells are a recently emerged class of limited range, personal use home/office base stations (BSs) [1]- [3]. The main purpose of femtocell networks is to improve the indoor coverage of cellular networks. As it will be discussed in detail in Chapters 2 and 3, femtocells can coexist within macrocells in a split spectrum or a shared spectrum manner. The latter case constitutes an appropriate example for co-channel systems where CCI is a significant concern, and this is the reason why co-channel femtocells are a case study element throughout

3

this thesis. In the following two sections, the two classes of CCI handling methods, namely CCI avoidance and CCI cancellation, will be introduced.

1.1 Co-channel Interference Avoidance

A wireless signal has distinctive properties in various domains such as time, frequency, and space. The signals of two different systems can be distinguished from each other as long as a domain can be found in which the signals do not overlap. Interference avoidance methods aim at ensuring orthogonality between the co-channel systems, which is realized by guaranteeing that there is at least one such domain.

The orthogonality can be established in time domain by having the systems transmit at different time slots; in frequency domain by avoiding any overlap between the spectra of the systems within the same band; in code domain by assigning different PN codes to different systems; in space domain by separating the transmitted beams; and in power domain by making the footprints of the transmit antennas not overlap. It should be noted that there is a strong similarity between the co-channel interference avoidance approaches and the basic methods that are used to implement the multiple accessing schemes in wireless systems such as TDMA, CDMA, and OFDMA.

The avoidance algorithms that will be presented in this dissertation are time-frequency domain based methods. In these algorithms, co-channel systems that employ OFDMA are considered, and it is aimed to ensure that the two systems utilize mutually exclusive sets of resource blocks. In Chapter 2, two different detection methods are investigated for finding the opportunities within the uplink frequency band of an OFDMA based system with timing misalignments. An algorithm for determining the synchronization point that minimizes the inter-carrier interference due to the timing misalignments is proposed.

There might be cases where both co-channel systems are being operated by the same service provider as in the example of a macrocell-femtocell coexistence. In such a scenario, it might be considered that the macrocell shares its resource block allocation information with the femtocells in order to have them avoid CCI. In Chapter 3, an algorithm is proposed

4

for femtocells, which utilizes this information along with local spectrum sensing results to enable femtocells to determine the usable resource blocks within the macrocell spectrum both in DL and UL.

In contrast to scenarios where the two co-channel systems are in close collaboration, it might be possible that the CCI avoidance has to be performed in a semi-blind manner where the systems have information about only the very basic system parameters of the other co-channel system. In Chapter 4, we propose two algorithms that might be used for enhancing the performance in CCI avoidance. The first algorithm enables determining the size of the resource blocks employed in an uplink OFDMA signal. The second one, on the other hand, targets at separating the user signals from each other so that the close-by users' blocks can be determined and avoided more reliably.

1.2 Co-channel Interference Cancellation

In cases where there is an overlap between the two co-channel signals in all usable domains, CCI cancellation algorithms need to be employed in order to separate the signals from each other. Compared to the avoidance algorithms, the cancellation methods usually have a higher computationally complexity, and therefore, their realizability highly depends on the available digital signal processing power.

The key concept that determines the feasibility of CCI cancellation is the signal separability. Any differences in the signal properties such as the waveforms and spectra as well as the differences that the signals attain in the propagation channel such as their delays might serve as a means of signal separation [4].

It might be possible to separate two single carrier signals that overlap in all domains in the transmitter side exploiting the differences in the received signals due to the independent channels that they propagate through. A good example for signal separation by taking advantage of the difference in the wireless channels is the MIMO receivers. In this dissertation, the algorithm presented in Chapter 5 takes MIMO receivers one step further and introduces reception of MIMO signals with a single receiver. The proposed maximum

likelihood based algorithm relaxes the hardware requirement of MIMO systems but brings about a considerably higher digital signal processing necessity. The performance tests show that the proposed method is feasible for a two transmitter system, however, any similarity between the two propagation channels degrades the performance.

A more complicated scenario where signal separability might be attainable is the case of two co-channel signals one of which carries information in time domain, and the other one in frequency domain. The algorithm presented in Chapter 6 deals with this kind of a scenario and proposes an iterative cancellation method where a single antenna receiver is considered. The two co-channel signals are estimated, demodulated, and regenerated in a successive manner to yield a better estimate of the other signal. It is shown that after a limited number of iterations, a quite successful signal separation can be obtained.

Future work in this direction includes separation of co-channel signals that overlap in all readily imaginable domains such as the unintentional co-channel signals that are observed in cellular systems with frequency reuse factor equal to 1.

1.3   Dissertation Outline

This dissertation primarily consists of five algorithms each of which is covered in a separate chapter. The algorithms in Chapter 2, Chapter 3, and Chapter 4 relate to interference avoidance, while the algorithms in Chapter 5 and in Chapter 6 deal with interference cancellation. The interference avoidance related algorithms focus on opportunity detection for OFDMA-based CR systems with timing offsets, frequency reuse for femtocells, and user separation in OFDMA-based CR systems, respectively. The two interference cancellation algorithms, on the other hand, are reception of MIMO signals with a single receiver and iterative CCI cancellation. In the remainder of this section, a detailed outline of each chapter is provided.

1.3.1 Chapter 2: Opportunity Detection for OFDMA-Based Cognitive Radio Systems with Timing Misalignment

Accurate detection of spectrum opportunities within the frequency band of an OFDMA system carries critical importance for OFDMA-based cognitive radios. In this chapter, we analyze the opportunity detection performances of energy detection and ESPRIT (estimation of signal parameters by rotational invariance techniques) algorithms in the presence of timing misalignments in uplink (UL) OFDMA. For the energy detector, the statistics of subcarrier power are derived considering timing misalignments, and they are verified through computer simulations. Using these statistics, which take inter-carrier-interference (ICI) effects into account, receiver operating characteristics (ROCs) of the energy detector receiver are obtained. It is shown that energy detection has a considerably better performance than ESPRIT, especially when the subcarrier assignment changes frequently. Moreover, a closed form expression is derived for the UL-OFDMA synchronization point that minimizes the ICI. Finally, it is shown that employing resource allocation blocks with larger sizes in the primary network yields better opportunities for the cognitive radio.[1]

1.3.2 Chapter 3: Interference Scenarios and Frequency Reuse for Next-Generation Femtocell Networks

Femtocells have a strong potential for increasing the efficiency and coverage of next-generation broadband wireless networks. In this chapter, a co-channel framework for the coexistence of OFDMA based macrocell and femtocell wireless networks is proposed. It is based on utilizing the resource blocks of macrocell-associated mobile stations (mMSs) that are far away to a femtocell base station (fBS), therefore avoiding strong interference that may occur between a femtocell and close-by mMSs. An avoidance method that jointly utilizes the spectrum sensing results as well as scheduling information obtained from the macrocell base station (mBS) is introduced. Moreover, the impact of ICI from the mMSs in the uplink is discussed and evaluated through simulations.[2]

---

[1]The content of this chapter is published in parts in [5, 6].
[2]The content of this chapter is published in parts in [7].

7

1.3.3 Chapter 4: Uplink User Signal Separation for OFDMA-Based Cognitive Radios

Spectrum awareness of OFDMA based cognitive radios (CR) can be improved by enabling them to separate the primary user signals in the uplink. Assuming availability of information about the basic parameters of the primary system as well as time synchronization to the first arriving user signal, two algorithms are proposed in this chapter. The first one targets estimating the size of the frequency allocation block of the primary system. The performance of this algorithm is compared with the results of a Gaussian approximation based approach that aims to determine the probability of correct block size estimation theoretically. The second one is a semi-blind user separation algorithm, which estimates the carrier frequency offsets and time delays of each block by exploiting the cross-correlations over pilot subcarriers. A two-dimensional clustering method is then employed to group the estimates, where each group belongs to a different user. It is shown that the proposed algorithms can improve the spectrum opportunity detection of cognitive radios. Feasibility of the algorithms is proved through practical simulations.[3]

1.3.4 Chapter 5: Reception of MIMO-OFDMA Signals with a Single Channel Receiver

This chapter proposes to implement reception of MIMO-OFDMA signals using a single receiver rather than multiple receivers. For this purpose, impairments related to each of the RF front-end components are investigated. Challenges of MIMO-OFDMA reception are addressed in comparison with SISO. A complete procedure is provided to receive and do impairment estimation for WiMAX MIMO signals using a single receiver according to the IEEE 802.16 standards.[4]

---

[3]The content of this chapter is published in parts in [8, 9].

[4]The content of this chapter is published in parts in [10, 11].

1.3.5 Chapter 6: An Iterative Interference Cancellation Method for Co-Channel Multicarrier and Narrowband Systems

Coexistence of narrowband (NB) and multicarrier technologies will be a major concern in next generation wireless communication systems due to the co-channel interference problem. In this chapter, an efficient CCI cancellation method is proposed that may be utilized for improved coexistence of NB and multicarrier technologies. The method treats both co-channel signals as desired signals and enhances them in an iterative manner. In every iteration, the signals are demodulated, regenerated, and subtracted from the received signal successively in order to obtain a better estimate of the other co-channel signal. Computational complexity of the proposed method is compared in detail with the joint demodulation technique. Through computer simulations, it is shown that the proposed method has lower complexity compared to joint demodulation, and it yields significant gains in the symbol error rate (SER) performance of both the NB and multicarrier systems.[5]

---

[5]The content of this chapter is published in parts in [12, 13].

CHAPTER 2

OPPORTUNITY DETECTION FOR OFDMA-BASED COGNITIVE RADIO SYSTEMS WITH TIMING MISALIGNMENT

2.1   Introduction

Increasing spectral crowding constitutes one of the major factors that need to be taken into account when designing future wireless systems. The growing number of wireless technologies may force future systems to share the same spectrum. Cognitive radio [14] is seen as a promising approach in this direction [15, 16]. Cognitive radio introduces the concept of opportunistic spectrum usage [17] in which a secondary network utilizes unused parts of a spectrum that is owned by a primary system. Cognitive radios are required to reliably sense the spectrum opportunities in order to minimize probability of false alarms (PFA) and probability of missed detections (PMD) [18, 19]. For example, in a scenario as in Fig. 2.1, the secondary users (SUs) in the cognitive radio system need to accurately sense the spectrum opportunities in the primary network and utilize them in an optimal manner.

Third generation (3G) wireless technologies have mostly been using code division multiple access (CDMA) in their physical layers. For example, International Mobile Telecommunications 2000 (IMT-2000), which is the worldwide standard for third generation (3G) wireless technologies defined by the International Telecommunication Union (ITU), defines six standards for 3G networks, three of which are based on CDMA: Wideband CDMA, CDMA-2000, TD-CDMA/TD-SCDMA, EDGE, DECT, and WiMAX. While the first five of these standards were approved by ITU in 1999, WiMAX, which is based on orthogonal frequency division multiple access (OFDMA), was approved by the ITU in 2007. However, fourth generation (4G) of wireless communications is expected to be dominated by the

10

OFDMA technology. OFDMA has a number of advantages over the other wireless technologies such as easily managing multiple access interference and narrowband interference, enabling dynamic channel allocation, and allowing simple channel equalization in frequency domain. Therefore, we consider cognitive radios that employ OFDMA in their physical layer.

For an OFDMA based cognitive radio, spectrum opportunity can be defined as the set of subcarriers that are not utilized by the primary system. In order to take advantage of the spectrum opportunities, orthogonality to the primary system needs to be established. For such a radio, the first step in spectrum sensing is the detection of the presence of a primary user, which can be achieved utilizing the cyclic prefix (CP) or the guard band of the received signal [20]- [22]. After detecting the presence of a primary user, A threshold based detector such as in [23] can be employed for detecting the spectrum opportunities, where appropriate selection of the threshold is critical for a good detection performance. Spectrum sensing performance of energy detectors can be quantified by receiver operating characteristic (ROC) curves (see e.g. [24]). A particularly challenging scenario that has not been considered in detail in the prior art for cognitive radio systems is when some of the uplink (UL) OFDMA user signals arrive at the receiver with delays larger than the CP of the symbol (see e.g., [25]- [27], and Figs. 2.1 and 2.2). For example, in Fig. 2.2, the secondary user SU-1 communicates with SU-2 utilizing the available spectrum opportunities. However, the signals of the primary users arriving at SU-2 after the CP of SU-1 (i.e., UL signals of mobile stations MS-1 and MS-4) result in inter-symbol interference (ISI) as well as inter-carrier interference (ICI), which may considerably decrease the spectrum opportunities.

An interesting case where such a timing misalignment problem may occur is the co-existence of a femtocell network [28, 29] with a macrocell network, both of which employ OFDMA. As discussed in [30] and [31], macrocell and femtocell may coexist through either a split-spectrum approach, where both networks are assigned orthogonal bands, or a shared-spectrum approach, where unused parts of the macrocell spectrum are utilized by the femtocell that acts as a cognitive radio. In a shared-spectrum scenario, while the macrocell

11
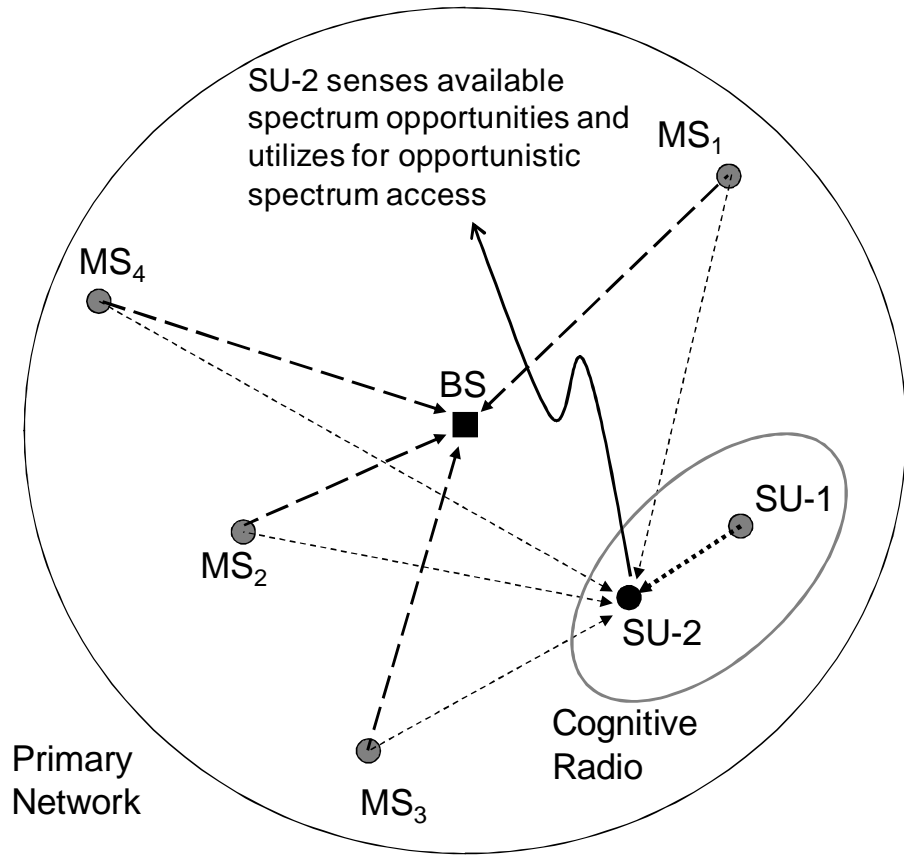
Figure 2.1 Cognitive radio scenario in consideration.
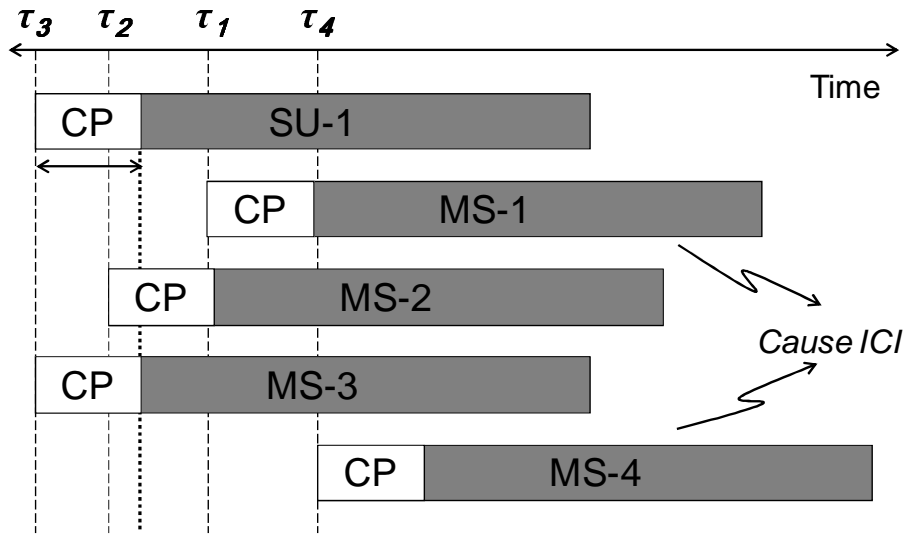
Figure 2.2 The primary network and cognitive radio signals arriving at SU-2 and the timing misalignment problem.

12

users are synchronized with the macrocell base station (BS) through initial/periodic ranging [32, 33], their signals may arrive at the femtocell BS with different delays (see [34] for an analysis of arrival times at the femtocell BS), which can make detection of spectrum opportunities by the femtocell quite challenging.

In this chapter, detection of spectrum opportunities in UL-OFDMA is investigated in the presence of considerable timing misalignment between users (see e.g. [5]). Taking into account the effects of ICI that appear as a result of timing misalignments, the statistics of the energy detector receiver are obtained, and the related ROCs for spectrum sensing are derived. Moreover, a closed form expression for the primary user distance that causes the strongest interference to the cognitive radio is obtained. Finally, optimum UL-OFDMA synchronization point that minimizes the interference to the cognitive radio is calculated[1]. Through computer simulations, opportunity detection error probabilities using the energy detector are determined for various scenarios and they are compared with the detection performance of the estimation of signal parameters by rotational invariance techniques (ESPRIT) algorithm. Impact of the primary network's resource allocation block size on the cognitive radio is also investigated using the parameters specified in LTE and WiMAX standards.

Organization of this chapter is as follows. Section 2.2 provides the system model, while Section 2.3 shortly introduces energy detection based and ESPRIT algorithm based spectrum sensing approaches and discusses the subcarrier assignment schemes in different wireless standards. In Section 2.4, the statistics of the energy detector decision variable are investigated, and the user distance yielding the highest interference is derived. In Section 2.5, ROCs with and without timing misalignment are derived for receivers that employ noise-based threshold and normalized threshold. Section 2.6 investigates the optimum synchronization point for an UL-OFDMA receiver, Section 2.7 presents the simulation results, and Section 2.8 concludes the chapter.

---

[1]Note that UL-OFDMA synchronization has been investigated in several works in the prior art (see e.g. [35] and [36] and the references therein). In this chapter, we look at the timing synchronization problem from a secondary system's perspective for minimizing interference, which has not been considered in the literature to the best of our knowledge.

13

2.2 UL-OFDMA System Model

Consider an OFDMA system with N_u users in the uplink. The sampled time domain signal at the transmitter of user i can be written as

$$x_i^{(m)}(n) = \sqrt{P_{\mathrm{tx},i}} \sum_{k \in \boldsymbol{\Gamma}_i} X_i^{(m)}(k) e^{\frac{j2\pi kn}{N}} \ , -N_\mathrm{cp} \le n \le N-1, \tag{2.1}$$

where m is the symbol index, $P_{\mathrm{tx},i}$ is the transmit power for user i, $k \in \boldsymbol{\Gamma}_i$ is the subcarrier index, $\boldsymbol{\Gamma}_i$ is the set of subcarriers of length N_i assigned to user i out of N total subcarriers, N_cp is the length of the cyclic prefix, and $X_i^{(m)}(k)$ is the data on the kth subcarrier and mth symbol of the ith user.

The time domain aggregate received signal is the superposition of signals from all users, each of which propagates through a different multipath channel and arrives at the receiver with a delay $\tilde{\delta}_i = \lceil N\tilde{\tau}_i/T \rceil$, where $\tilde{\tau}_i$ is the propagation delay experienced by user i, and T is the duration of the useful part of the symbol. Then, aggregate discrete-time received signal can be expressed as

$$y(n) = \sum_{i=1}^{N_\mathrm{u}} y_i(n) + w(n), \tag{2.2}$$

where $w(n)$ denotes the additive white Gaussian noise (AWGN), and

$$y_i(n) = \sqrt{P_{\mathrm{rx},i}} \sum_{l=0}^{L-1} \alpha_i^{(m)}(l) \sum_{m=-\infty}^{\infty} x_i^{(m)}\Big(n - D_{l,i} - m(N + N_\mathrm{cp})\Big), \tag{2.3}$$

where $P_{\mathrm{rx},i}$ is the received power for user i, L denotes the total number of multipath components (MPCs), $\alpha_i^{(m)}(l)$ is the complex amplitude of the lth MPC for user i, and $D_{l,i} = \lceil N\tau_{l,i}/T \rceil + \tilde{\delta}_i$, where $\tau_{l,i}$ is the delay of the lth MPC for user i.

If $D_{l,i} \le N_\mathrm{cp}$, it is easy to prove that the frequency domain signal for the kth subcarrier of user i is given by

$$Y_i^{(m)}(k) = \sqrt{E_{\mathrm{sc},i}} X_i^{(m)}(k) \sum_{l=0}^{L-1} \alpha_i^{(m)}(l) e^{-\frac{j2\pi k D_{l,i}}{N}} \ , \tag{2.4}$$

14

where $E_{\mathrm{sc},i}$ is the average received energy per subcarrier for user i, which is equal to $P_{\mathrm{rx},i}$. On the other hand, if $D_{l,i} > N_{\mathrm{cp}}$, the FFT window at the receiver will include signals from two consecutive symbols of the transmitted signal. As a consequence, this will result in inter-symbol interference as well as inter-carrier interference. Getting the FFT of (2.3), the received signal on the kth subcarrier of user i can be written as [27]

$$
Y_i^{(m)}(k) = \frac{\sqrt{E_{\mathrm{sc},i}}}{N} \sum_{l=0}^{L-1} \alpha_i^{(m)}(l) \Bigg\{ \sum_{n=0}^{D_{l,i}-N_{\mathrm{cp}}-1} x_i^{(m-1)}(n + N + N_{\mathrm{cp}} - D_{l,i}) e^{-\frac{j2\pi kn}{N}}
$$
$$
+ \sum_{n=D_{l,i-N_{\mathrm{cp}}}}^{N-1} x_i^{(m)}(n - D_{l,i}) e^{-\frac{j2\pi kn}{N}} \Bigg\} . \quad (2.5)
$$

After plugging (2.1) into (2.5) and some manipulation, we have

$$
Y_i^{(m)}(k) = \sqrt{E_{\mathrm{sc},i}} \sum_{l=0}^{L-1} \alpha_i^{(m)}(l) \Big\{ S_{\mathrm{d},i,l}(k) + I_{1,i,l}(k) + I_{2,i,l}(k) \Big\}, \quad (2.6)
$$

where the desired signal, interference from the same subcarrier of the previous symbol, and the total interference from other subcarriers are respectively given as

$$
S_{\mathrm{d},i,l}(k) = X_i^{(m)}(k) K_{1,i,l}(k) e^{\frac{-j2\pi k D_{l,i}}{N}} \quad (2.7)
$$

$$
I_{1,i,l}(k) = X_i^{(m-1)}(k) K_{2,i,l}(k) e^{\frac{-j2\pi k (D_{l,i}-N_{\mathrm{cp}})}{N}} \quad (2.8)
$$

$$
I_{2,i,l}(k) = \frac{1}{N} \sum_{\substack{p \in \boldsymbol{\Gamma}_i \\ p \neq k}} \underbrace{\left[\frac{1 - e^{\frac{j2\pi(p-k)(D_{l,i}-N_{\mathrm{cp}})}{N}}}{1 - e^{\frac{j2\pi(p-k)}{N}}} \right]}_{h_i(p,k)} \underbrace{\left(- X_i^{(m)}(p) e^{-\frac{j2\pi p D_{l,i}}{N}} + X_i^{(m-1)}(p) e^{\frac{j2\pi p(N_{\mathrm{cp}}-D_{l,i})}{N}} \right)}_{g_i(p)},
$$

$$
(2.9)
$$

where

$$
K_{1,i,l}(k) = \frac{N - D_{l,i} + N_{\mathrm{cp}}}{N} \times \mathcal{I}(i,k) ,
$$
$$
K_{2,i,l}(k) = \frac{D_{l,i} - N_{\mathrm{cp}}}{N} \times \mathcal{I}(i,k), \quad (2.10)
$$

15

with $\mathcal{I}(i, k)$ denoting an indicator function given by

$$\mathcal{I}(i, k) = \begin{cases} 1 \ , & \text{if } k \in \boldsymbol{\Gamma}_i \ , \\ 0 \ , & \text{if } k \notin \boldsymbol{\Gamma}_i \ . \end{cases} \tag{2.11}$$

Note that the interference terms $I_{1,i,l}(k)$ and $I_{2,i,l}(k)$ will both be zero if the received MPC is located within the CP duration. The aggregate frequency-domain signal can then be written as

$$Y^{(m)}(k) = \sum_{i=1}^{N_{\mathrm{u}}} Y_i^{(m)}(k) + W(k) \ , \tag{2.12}$$

where $W(k) \sim \mathcal{CN}\left(0, \sigma^2\right)$ is the DFT of $w(n)$, $\sigma^2 = N_0/2$, and $\mathcal{CN}\left(\mu, \sigma^2\right)$ denotes the distribution of a circularly symmetric complex Gaussian random variable with mean μ and variance σ^2.

2.3 Spectrum Sensing Techniques and Impact of Subcarrier Assignment Scheme

Different methods may be considered for the detection of spectrum opportunities in an OFDMA system. In this chapter, energy detection and ESPRIT algorithms are considered. Moreover, impact of subcarrier assignment strategy on the opportunity detection performance is evaluated.

2.3.1 Energy Detector Method

In the energy detector method, based on (2.6), we consider the following decision variable and compare it with a threshold ξ

$$P^{(m)}(k) = \left| Y^{(m)}(k) \right|^2 \underset{H_0}{\overset{H_1}{\gtrless}} \xi \ , \tag{2.13}$$

where hypothesis H_1 implies that subcarrier k is occupied, and hypothesis H_0 implies that it is not. A diagram of the energy detector method is provided in Fig. 2.3. Statistics of the

16
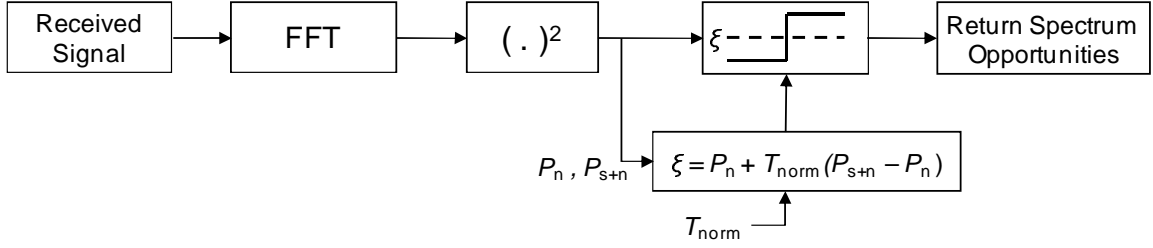
Figure 2.3 Diagram of the energy detector method.

decision variable $P^{(m)}(k)$ in the presence of timing misalignment will be discussed in more detail in Section 2.4, while possible approaches for selecting the threshold ξ are discussed in Section 2.5.

2.3.2 ESPRIT Method

ESPRIT is a high resolution signal parameter estimation algorithm that exploits the shift invariance property of signals [37]. It belongs to the class of signal subspace methods in that it relies on an eigendecomposition of the covariance matrix of the received signal [38]. The algorithm has been employed in a wide variety of applications including direction-of-arrival estimation in antenna arrays [37], channel estimation in multipath fading channels [39], and estimating the parameters of sinusoids in noise [40].

The problem of determining the occupied subcarriers in an OFDMA signal can be considered as identifying the number and frequencies of a set of sinusoids in additive noise. OFDM based signals are suitable for implementing ESPRIT because they are made shift invariant by the addition of a cyclic prefix, which means that a time shift not exceeding the CP does not alter the statistical features of the OFDM signal. Exploiting this property of the OFDM signal, carrier frequency offset estimation using ESPRIT was performed in [41]. In [42], ESPRIT algorithm was proposed for estimating the occupied subcarriers of an OFDM symbol. Although it is known that ESPRIT cannot be the optimum detection method when the maximum delay observed in the system is larger than the CP (due to the degradation in the shift invariance of OFDM symbols), in this chapter, the ESPRIT

17

www.manaraa.com

performance in an asynchronous UL-OFDMA system is simulated to provide a relative measure for the energy detection performance.

In the practical ESPRIT implementation for determining the occupied subcarriers of an OFDM symbol, the first step is to estimate the number of occupied subcarriers (N_{ocp}), which is done via the minimum descriptive length (MDL) algorithm introduced in [43]. Estimation of subcarrier frequencies, on the other hand, is performed by constructing the auto- and cross-covariance matrices of the received signal. From the received signal $y(n)$, two sample vectors $\boldsymbol{y}(n)$ and $\boldsymbol{z}(n)$ of length Υ are formed

$$
\begin{aligned}
\boldsymbol{y}(n) &= [y(n),\, y(n+1),\, \cdots,\, y(n+\Upsilon-1)], \\
\boldsymbol{z}(n) &= [y(n+1),\, y(n+2),\, \cdots,\, y(n+\Upsilon)],
\end{aligned}
\tag{2.14}
$$

where Υ is equal to $\mathcal{M} \times (N + N_{\text{cp}})$, $\mathcal{M}$ being the number of adjacent symbols with the same occupied subcarriers.

The auto-covariance matrix $\mathbf{R}_{\text{yy}}$ and cross-covariance matrix $\mathbf{R}_{\text{yz}}$ are obtained as follows

$$
\mathbf{R}_{\text{yy}} = \mathrm{E}\{\boldsymbol{y}(n)\boldsymbol{y}^*(n)\}, \text{ and } \mathbf{R}_{\text{yz}} = \mathrm{E}\{\boldsymbol{y}(n)\boldsymbol{z}^*(n)\},
\tag{2.15}
$$

where $E\{\cdot\}$ denotes the expectation operation. It is important to note that the reliability of $\mathbf{R}_{\text{yy}}$ and $\mathbf{R}_{\text{yz}}$ is directly proportional to $\mathcal{M}$. By performing an eigen-decomposition on $\mathbf{R}_{\text{yy}}$, its eigenvalues are determined, where the minimum eigenvalue $\lambda_{\mathrm{m}in}$ is the noise variance[2]. Noise power is subtracted from $\mathbf{R}_{\text{yy}}$ and $\mathbf{R}_{\text{yz}}$ to obtain

$$
\mathbf{C}_{\text{yy}} = \mathbf{R}_{\text{yy}} - \lambda_{\mathrm{m}in}\mathbf{I} \text{ and } \mathbf{C}_{\text{yz}} = \mathbf{R}_{\text{yz}} - \lambda_{\mathrm{m}in}\mathbf{Z},
\tag{2.16}
$$

where $\mathbf{I}$ is the identity matrix, and $\mathbf{Z}$ is a matrix with ones on the first subdiagonal and zeros elsewhere. The frequencies of the occupied subcarriers are yielded by the first N_{ocp}

---

[2]Note that since $\Upsilon > N_{\text{ocp}}$, $\mathbf{R}_{\text{yy}}$ is a singular matrix; hence, $\Upsilon - N_{\text{ocp}}$ of its smaller eigenvalues yield the noise variance.

18

Table 2.1 The uplink parameters used in LTE and WiMAX standards.

		WiMAX		
	LTE	PUSC 1	PUSC 2	ASP
N_{symb}	7	3	3	$N(=1,2,3,\text{or } 6)$
N_{sc}	12	4	3	$9 \times M$ (where $N \times M = 6$)
Block Size	84	12	9	54

largest generalized eigenvalues of the matrix pair $(\mathbf{C}_{\text{yy}}, \mathbf{C}_{\text{yz}})$ (The reader is referred to [40] for a step-by-step guide of the ESPRIT algorithm).

The matrix operations that it requires make the ESPRIT algorithm highly computationally complex and may induce an extended processing delay. This kind of a delay renders ESPRIT less feasible in a real-time application.

2.3.3 Subcarrier Assignment Schemes in Different Wireless Standards

In an OFDMA system, time-frequency resources are dynamically shared between users, exploiting channel variation in both frequency and time domains. The resource allocation, therefore, takes the form of one or more two-dimensional blocks, where each block is defined by N_{symb} consecutive OFDMA symbols in the time domain and N_{sc} consecutive subcarriers in the frequency domain. In the standards, the block is referred using different names; it is referred as resource block (RB) in LTE, while referred as tile or bin in WiMAX [44]-[46]. When multiple blocks constitute a resource allocation, those blocks may be either distributed or localized in the frequency domain so that frequency diversity or channel dependent scheduling can be appropriately exploited. Fig. 2.8 illustrates the uplink parameters for N_{symb} and N_{sc} that are used in different standards[3]. Note that in essence, all of the subcarrier assignment schemes (SAS) shown in Fig. 2.8 are blockwise assignments (BA) with different block sizes.

In the simulations in Section 2.7, along with the blockwise SASs used in different standards, we also consider a randomized assignment (RA). In RA, each individual subcarrier may be assigned to a different user, i.e., $N_{sc} = 1$, and N_{symb} may take any appropriate

---

[3]PUSC: partial usage of subchannels, ASP: adjacent subcarrier permutation.

19

value. In Section 2.7, we demonstrate through simulations that RA limits the amount of spectrum opportunities for a cognitive radio most, because it causes ICI to the maximum number of empty subcarriers. The SASs that provide better opportunities for the cognitive radio are the BAs that have large N_{sc} due to the lesser number of empty subcarriers affected from ICI.

2.4   Statistics of the Energy Detector Decision Variable with Timing Misalignment

In order to analyze how the timing misalignment problem affects the opportunity detection, the statistics of the decision variable in (2.13) have to be evaluated. After plugging (2.12) into (2.13), we have

$$
\begin{aligned}
P^{(m)}(k) = \left| Y^{(m)}(k) \right|^2 = \sum_{i=1}^{N_{\mathrm{u}}} \left| Y_i^{(m)}(k) \right|^2 + |W(k)|^2 \\
+ 2\mathrm{Re}\Big\{ \underbrace{ W^*(k) \sum_{i=1}^{N_{\mathrm{u}}} Y_i^{(m)}(k) }_{\mathrm{Zero-mean\ RV}} \Big\} + 2 \sum_{i=1}^{N_{\mathrm{u}}-1} \sum_{j=i+1}^{N_{\mathrm{u}}} Y_i^{*(m)}(k) Y_j^{(m)}(k),
\end{aligned}
$$

$$(2.17)$$

where the last term of (2.17) is 0 since $Y_i^{(m)}(k)$ and $Y_j^{(m)}(k)$ cannot be non-zero simultaneously. The statistics of (2.17) can be evaluated by analyzing the statistics of the individual terms as will be discussed below. To keep the expressions analytically tractable[4], we consider $L = 1$ in (2.6), and drop the multipath indices from related expressions in (2.6)-(2.9).

First, using (2.4), we may write $\left| Y_i^{(m)}(k) \right|^2$ as

$$
\begin{aligned}
\left| Y_i^{(m)}(k) \right|^2 &= E_{\mathrm{sc},i} \left| S_{\mathrm{d},i}(k) + I_{1,i}(k) + I_{2,i}(k) \right|^2 \\
&= E_{\mathrm{sc},i} \Big[\left| S_{\mathrm{d},i}(k) \right|^2 + \left| I_{1,i}(k) \right|^2 + \left| I_{2,i}(k) \right|^2 \\
&\quad + 2\mathrm{Re}\Big\{ S_{\mathrm{d},i}^*(k) I_{1,i}(k) + S_{\mathrm{d},i}^*(k) I_{2,i}(k) + I_{1,i}^*(k) I_{2,i}(k) \Big\} \Big],
\end{aligned}
$$

$$(2.18)$$

---

[4]For the derivation of the statistics of (2.17) in a multipath channel, the reader is referred to Appendix B.

20

where

$$\left|S_{\mathrm{d},i}(k)\right|^2 = \left|X_i^{(m)}(k)\right|^2 K_{1,i}^2(k), \tag{2.19}$$

$$\left|I_{1,i}(k)\right|^2 = \left|X_i^{(m-1)}(k)\right|^2 K_{2,i}^2(k), \tag{2.20}$$

$$\left|I_{2,i}(k)\right|^2 = \frac{1}{N^2}\Big(\sum_{\substack{p\in\boldsymbol{\Gamma}_i\\p\neq k}}\left|h_i^2(p,k)\right|\left|g_i^2(p)\right| + \mathrm{Re}\Big\{\underbrace{\sum_{\substack{p\in\boldsymbol{\Gamma}_i\\p\neq k}}\sum_{\substack{q\in\boldsymbol{\Gamma}_i\\q\neq k,q\neq p}} h_i^*(p,k)h_i(q,k)g_i^*(p)g_i(q)}_{\mathrm{Zero-mean\ RV}}\Big\}\Big),$$
$$\tag{2.21}$$

$$S_{\mathrm{d},i}^*(k)I_{1,i}(k) = X_i^{*(m)}(k)X_i^{(m-1)}(k)K_{1,i}(k)K_{2,i}(k)e^{\frac{j2\pi k N_{\mathrm{cp}}}{N}}, \tag{2.22}$$

$$S_{\mathrm{d},i}^*(k)I_{2,i}(k) = \frac{1}{N}X_i^{*(m)}(k)K_{1,i}(k)e^{\frac{j2\pi k D_{l,i}}{N}}\sum_{\substack{p\in\boldsymbol{\Gamma}_i\\p\neq k}} h_i(p,k)g_i(p), \tag{2.23}$$

$$I_{1,i}^*(k)I_{2,i}(k) = \frac{1}{N}X_i^{*(m-1)}(k)K_{2,i}(k)e^{\frac{j2\pi k(D_{l,i}-N_{\mathrm{cp}})}{N}}\sum_{\substack{p\in\boldsymbol{\Gamma}_i\\p\neq k}} h_i(p,k)g_i(p), \tag{2.24}$$

with, as indicated in (2.9),

$$g_i(p) = -X_i^{(m)}(p)e^{-\frac{j2\pi p D_{l,i}}{N}} + X_i^{(m-1)}(p)e^{\frac{j2\pi p(N_{\mathrm{cp}}-D_{l,i})}{N}}, \tag{2.25}$$

$$h_i(p,k) = \frac{1 - e^{\frac{j2\pi(p-k)(D_{l,i}-N_{\mathrm{cp}})}{N}}}{1 - e^{\frac{j2\pi(p-k)}{N}}} \ , \ \text{and} \ \ h_i^2(p,k) = \frac{1 - \cos\Big(\frac{2\pi(p-k)(D_{l,i}-N_{\mathrm{cp}})}{N}\Big)}{1 - \cos\Big(\frac{2\pi(p-k)}{N}\Big)} \ . \tag{2.26}$$

Note that (2.22)-(2.24) as well as the indicated terms in (2.17) and (2.21) are zero-mean random-variables (RVs). Then, the mean of (2.17) can be evaluated as

$$\mathrm{E}\Big\{P^{(m)}(k)\Big\} = \sum_{i=1}^{N_{\mathrm{u}}}\mathrm{E}\Big\{\left|Y_i^{(m)}(k)\right|^2\Big\} + n_{\mathrm{d}}\sigma^2 \ , \tag{2.27}$$

where n_{d} denotes the degree of freedom (DOF) of noise terms, and calculation of $\mathrm{E}\Big\{\left|Y_i^{(m)}(k)\right|^2\Big\}$ will be discussed in Appendix A.

21

On the other hand, the variance of (2.17) is

$$\mathrm{Var}\Big\{ P^{(m)}(k)\Big\} = \sum_{i=1}^{N_{\mathrm{u}}} \mathrm{Var}\Big\{\Big|Y_i^{(m)}(k)\Big|^2\Big\} + 2n_{\mathrm{d}}\sigma^4 + 8n_{\mathrm{d}}\sigma^4 \sum_{i=1}^{N_{\mathrm{u}}} \mathrm{E}\Big\{\Big|Y_i^{(m)}(k)\Big|^2\Big\}, \qquad (2.28)$$

where the variances of the first two terms are straight-forward, and the variance of the third term is calculated as

$$\mathrm{Var}\Big\{ 2\mathrm{Re}\Big\{ W^*(k)\sum_{i=1}^{N_{\mathrm{u}}} Y_i^{(m)}(k)\Big\}\Big\}$$

$$= \mathrm{E}\Big\{ 4W^2(k)\Big(\sum_{i=1}^{N_{\mathrm{u}}}\big|Y_i^{(m)}(k)\big|^2 + \sum_{i=1}^{N_{\mathrm{u}}-1}\sum_{j=i}^{N_{\mathrm{u}}} Y_i^{*(m)}(k)Y_j^{(m)}(k)\Big)\Big\} \qquad (2.29)$$

$$= 8n_{\mathrm{d}}\sigma^4 \sum_{i=1}^{N_{\mathrm{u}}} \mathrm{E}\Big\{\Big|Y_i^{(m)}(k)\Big|^2\Big\}. \qquad (2.30)$$

Hence, calculation of $\mathrm{E}\Big\{\Big|Y_i^{(m)}(k)\Big|^2\Big\}$ and $\mathrm{Var}\Big\{\Big|Y_i^{(m)}(k)\Big|^2\Big\}$ are sufficient for obtaining the statistics of (2.17) as in (2.27) and (2.28), as will be illustrated for different modulation schemes in Appendix A.

2.4.1   User Distance Yielding the Strongest Interference

The ICI power from a certain user is scaled by the received signal energy from that user, $E_{\mathrm{sc},i}$, as indicated in (15). However, in (15), the distance-dependency of the received signal energies was not explicitly taken into account, and it was assumed that $E_{\mathrm{sc},i}$ is a given parameter. However, in practice, both the received signal's delay and energy depend on the distance between the user and the secondary receiver.

Assuming a single tap channel, user delays are directly proportional to the user distances (d_i) through $D_{1,i} = \frac{d_i}{cT_s}$, where c is the speed of light, and T_s is the sampling time. Moreover, $E_{\mathrm{sc},i}$ also depends on d_i through $E_{\mathrm{sc},i} = \frac{\lambda^2}{(4\pi)^2 d_i^\gamma}P_{\mathrm{tx}}$, where λ is the wavelength of the transmitted signal, and γ is the path loss exponent. Since the impacts of d_i on $D_{1,i}$ and $E_{\mathrm{sc},i}$ are inversely proportional to each other[5], it is expected that the interference power will

---

[5] $D_{1,i}$ increases linearly with d_i, and $E_{\mathrm{sc},i}$ decreases with γth power of d_i.

be maximized at a certain distance and then will start decreasing with d_i. Determining the d_i that causes the strongest interference might be useful for certain practical applications. An example can be a femtocell that has access to the subcarrier allocation map of the primary system as well as to the locations of the primary users (through its backbone connection to the primary system). If the femtocell knows that users that are located at/around a specific distance cause the highest interference, it can avoid using the empty subcarriers that are adjacent to these users' subcarriers. Therefore, we analytically derived a closed-from expression for the user distance that causes the strongest interference.

Through simulations, it is determined that $\sum_{k \neq p} I_{1,i}^2(k)$ is negligible compared to $\sum_{k \neq p} I_{2,i}^2(k)$. Hence, the derivation is based on finding the distance where $I_{2,i}^2(k)$ (ICI) is maximized. The total interference power that is caused by a certain subcarrier p, summed over all empty subcarriers, is given by

$$\sum_{k \neq p} I_{2,i}^2(k) = \frac{\lambda^2}{(4\pi)^2 d_i^2} \frac{2}{N^2} \sum_{k \neq p} h_i^2(p, k) \; . \tag{2.31}$$

Replacing d_i with $cD_{1,i}T_s$, (2.31) can be rewritten as

$$\sum_{k \neq p} I_{2,i}^2(k) = \frac{2}{\left(4\pi f N T_s D_{1,i}\right)^2} \sum_{k \neq p} h_i^2(p, k) \; , \tag{2.32}$$

where f is the carrier frequency of the system. Differentiating (2.32) with respect to $D_{1,i}$ one obtains

$$\frac{d \sum_{k \neq p} I_{2,i}^2(k)}{d D_{1,i}} = \frac{2}{\left(4\pi f N T_s\right)^2} \Bigg(-\frac{2}{D_{1,i}^3} \sum_{k \neq p} \frac{1 - \cos\left(\frac{2\pi(p-k)(D_{1,i} - N_{\mathrm{cp}})}{N}\right)}{1 - \cos\left(\frac{2\pi(p-k)}{N}\right)}$$
$$+ \frac{1}{D_{1,i}^2} \sum_{k \neq p} \frac{\sin\left(\frac{2\pi(p-k)(D_{1,i} - N_{\mathrm{cp}})}{N}\right)}{1 - \cos\left(\frac{2\pi(p-k)}{N}\right)} \frac{2\pi(p-k)}{N} \Bigg). \tag{2.33}$$

23

The point where the ICI power is maximum can be found by equating (2.33) to 0, which yields

$$\frac{2}{D_{1,i}} \sum_{k \neq p} \frac{1 - \cos\left(\frac{2\pi(p-k)(D_{1,i}-N_{\text{cp}})}{N}\right)}{1 - \cos\left(\frac{2\pi(p-k)}{N}\right)} = \sum_{k \neq p} \frac{\sin\left(\frac{2\pi(p-k)(D_{1,i}-N_{\text{cp}})}{N}\right)}{1 - \cos\left(\frac{2\pi(p-k)}{N}\right)} \frac{2\pi(p-k)}{N}. \qquad (2.34)$$

The trigonometric terms in (2.34) can be approximated using Taylor series expansion under the condition that the inputs of $\cos(x)$ and $\sin(x)$ satisfy $-1 < x < 1$. Although this condition is met only for very small values of $(p - k)$, approximation is still useful since ICI is not significant for large values of $(p - k)$. Substituting the sine and cosine functions in (2.34) with the first two terms of their Taylor expansion, i.e. $\cos(x) \approx 1 - \frac{x^2}{2}$ and $\sin(x) \approx x - \frac{x^3}{3!}$, one obtains

$$\sum_{\substack{k=p-a \\ k \neq p}}^{k=p+a} \frac{\left(D_{1,i} - N_{\text{cp}}\right)^2}{D_{1,i}} = \sum_{\substack{k=p-a \\ k \neq p}}^{k=p+a} \left(\left(D_{1,i} - N_{\text{cp}}\right) - \frac{1}{6}\left(\frac{2\pi(p-k)}{N}\right)^2 \left(D_{1,i} - N_{\text{cp}}\right)^3 \right). \qquad (2.35)$$

where a is a small value that enables Taylor approximation and needs to be set inversely proportional with N_{cp}. Empirically, it is found that $\frac{N}{2N_{\text{cp}}}$ is an appropriate value for a. Utilizing summation formulas, one obtains

$$2a \frac{D_{1,i} - N_{\text{cp}}}{D_{1,i}} = 2a - \frac{1}{6}\left(\frac{2\pi\left(D_{1,i} - N_{\text{cp}}\right)}{N}\right)^2 \frac{a(a+1)(2a+1)}{3} , \qquad (2.36)$$

which, after some manipulations, leads to

$$D_{1,i}^3 - 2N_{\text{cp}}D_{1,i}^2 + N_{\text{cp}}^2 D_{1,i} - \frac{36N_{\text{cp}}}{\left(\frac{2\pi}{N}\right)^2(a+1)(2a+1)} = 0 . \qquad (2.37)$$

Note that two roots of (2.37) constitute a complex conjugate pair, and the third root is a real number, which yields the d_i causing the highest ICI. As it will be verified in Section 2.7, it is found that a quite accurate approximation for $D_{1,i}$ that yields the highest interference is $2N_{\text{cp}}$.

2.5 Receiver Operating Characteristics

For the detection of occupied subcarriers, we consider two types of threshold-based techniques for selecting ξ in (2.13) in this chapter: noise-based threshold (NBT) and normalized threshold (NT). While the threshold using the first approach is set based only on the noise level, the threshold using the second approach scales with the total received signal energy.

2.5.1 Noise-based Threshold

If the noise variance σ^2 is known, the threshold that satisfies a certain PFA can be selected. When a subcarrier k is not occupied by any user, (2.13) follows a centralized Chi-square distribution, whose cumulative distribution function (CDF) is given by [47]

$$\mathrm{F}_Y(y) = 1 - e^{-y/2\sigma^2} \sum_{\kappa=0}^{M-1} \frac{1}{\kappa!} \left(\frac{y}{2\sigma^2} \right)^{\kappa} , \qquad (2.38)$$

where $M = n_{\mathrm{d}}/2$ is an integer. For complex noise, we have $n_{\mathrm{d}} = 2$, and (2.38) becomes the CDF of an exponential distribution. Then, the PFA for a certain threshold ξ as in (2.13) becomes

$$\mathrm{P}_{\mathrm{fa}}(\xi) = 1 - \mathrm{F}_Y(\xi) = e^{-\xi/2\sigma^2} , \qquad (2.39)$$

where the threshold may also be written in terms of the PFA as

$$\xi = \mathrm{F}_Y^{-1}\left(1 - \mathrm{P}_{\mathrm{fa}}\right) . \qquad (2.40)$$

When subcarrier k is occupied, on the other hand, (2.13) follows a non-centralized Chi-square distribution, whose CDF is given by [47]

$$\tilde{\mathrm{F}}_Y(y, E_{\mathrm{sc},i}) = 1 - Q_M\left(\frac{\sqrt{E_{\mathrm{sc},i}}}{\sigma}, \frac{\sqrt{y}}{\sigma} \right) , \qquad (2.41)$$

25

where $Q_M(a, b)$ is the Marcum-Q function given by

$$Q_M(a, b) = \int_b^\infty x \left(\frac{x}{a}\right)^{M-1} e^{-(x^2+a^2)/2} I_{M-1}(ax)\mathrm{d}x \ , \qquad (2.42)$$

with $I_\zeta(x)$ denoting the ζth order modified Bessel function of the first kind [47]. Then, using (2.39), probability of detection P_d corresponding to a certain P_{fa} becomes

$$P_d(P_{fa}) = 1 - \tilde{F}_Y(\xi, E_{sc,i}) = Q_M\left(\frac{\sqrt{E_{sc,i}}}{\sigma}, \frac{\sqrt{F_Y^{-1}(1 - P_{fa})}}{\sigma}\right) \ . \qquad (2.43)$$

The relationship in (2.43) that relates the P_d to P_{fa} is commonly referred as the receiver operating characteristic curves.

In the presence of ICI, since the statistics of the received power will change, the ROC performance will get worse. In particular, using again the Chi-square distribution[6] for modeling the distribution of $\left|Y^{(m)}(k)\right|^2$ along with (2.27) and (2.28), the probability of false alarm and probability of detection (PD) that will be observed in the presence of ICI and using the threshold as in (2.40) is given by

$$P_{fa,ICI}(P_{fa}) = \frac{1}{N - \sum_{i=1}^{N_u} N_i} \sum_{\substack{k=1,\dots,N,k\notin\mathbf{\Gamma}_i, \\ i\in\{1,\dots,N_u\}}} Q_M\left(\frac{\sqrt{\tilde{\mu}(k)}}{\tilde{\sigma}(k)}, \frac{\sqrt{F_Y^{-1}(1 - P_{fa})}}{\tilde{\sigma}(k)}\right), \qquad (2.44)$$

$$P_{d,ICI}(P_{fa}) = \frac{1}{\sum_{i=1}^{N_u} N_i} \sum_{\substack{k\in\mathbf{\Gamma}_i, \\ i\in\{1,\dots,N_u\}}} Q_M\left(\frac{\sqrt{\tilde{\mu}(k)}}{\tilde{\sigma}(k)}, \frac{\sqrt{F_Y^{-1}(1 - P_{fa})}}{\tilde{\sigma}(k)}\right), \qquad (2.45)$$

---

[6]In Section 2.7.2, it will be verified thorough simulations that Chi-square distribution still well models $\left|Y^{(m)}(k)\right|^2$ in the presence of ICI.

where from the mean and variance of a non-centralized Chi-square distributed random variable, we may easily obtain

$$\tilde{\mu}(k) = \text{E}\left\{\left|Y^{(m)}(k)\right|^2\right\} - \frac{n_\text{d}\text{Var}\left\{\left|Y^{(m)}(k)\right|^2\right\}}{4\text{E}\left\{\left|Y^{(m)}(k)\right|^2\right\}} \ , \tag{2.46}$$

$$\tilde{\sigma}^2(k) = \frac{\text{Var}\left\{\left|Y^{(m)}(k)\right|^2\right\}}{4\text{E}\left\{\left|Y^{(m)}(k)\right|^2\right\}} \ . \tag{2.47}$$

2.5.2 Normalized Threshold

Note that NBT discussed in the previous section does not take the received energies of the useful signals into account and selects the threshold based on the noise level. A different way of setting the threshold, which considers both noise and signal energy levels, is to utilize a normalized threshold as follows

$$\xi = P_\text{n} + T_\text{norm}\big(P_\text{s+n} - P_\text{n}\big) \ , \tag{2.48}$$

where P_n and $P_\text{s+n}$ are the average noise energy and average signal+noise energy, respectively, and $0 \leq T_\text{norm} \leq 1$ denotes the normalized threshold. P_n can practically be estimated utilizing the guard bands (GB) of the OFDMA signal. To be more specific, by averaging the energies measured over the outermost subcarriers of left and right GBs, an estimate that is affected least from the ICI can be obtained. $P_\text{s+n}$, on the other hand, can be roughly determined by averaging the energies measured over all subcarriers except the null subcarriers in the guard bands.

There is a trade-off between probability of false alarms and probability of missed detections in the selection of T_norm. A too small T_norm causes many unused subcarriers to be detected as occupied and gives rise to a high PFA, whereas a too large T_norm causes PMD to increase. An analysis of the error probability with respect to the T_norm employed is provided in Section 2.7.

27

2.6 Determining the Optimum Synchronization Point

Depending on its location relative to the primary receiver, a secondary receiver may receive UL-OFDMA signals with $(D_{1,i} - \theta) > N_{\text{CP}}$ for certain users, where θ denotes the synchronization point. Interference caused by these users may be significant, especially if the received powers of these users are comparable to users whose $(D_{1,i} - \theta) \leq N_{\text{CP}}$. This can be the case if the transmit powers of users are unequal, for example due to adaptive power allocation. In a scenario where received powers from all users are similar regardless of d_i, significant interference may be observed.

To have as many spectrum opportunities as possible, the opportunistic system has to minimize the interference that is caused by the timing mismatch. As a solution, the synchronization point can be determined according to $D_{1,i}$ of uplink users; θ may be shifted towards a later point than the intuitive synchronization point, which is the delay of the first arriving user. In practice, user location information (e.g. through GPS) might be utilized by the secondary system to estimate the $D_{1,i}$. In the following, a closed form equation for the interference minimizing synchronization point is derived, denoted by θ_{opt}. As in Section 2.4.1, the derivation is based on minimizing ICI.

Let $\mathcal{S}$ denote the point where the useful part of the received signal starts, i.e., $\mathcal{S} = \theta + N_{\text{cp}}$. Assuming a single occupied subcarrier[7] p_i from each user, and replacing the N_{cp} term in $h_i^2(p, k)$ given in (2.26) with $\mathcal{S}$, the total ICI power is given by

$$\sum_{k \neq p_i} I_{2,i}^2(k) = \sum_{i=1}^{N_u} \sum_{k \neq p_i} \frac{1 - \cos\left(\frac{2\pi(p_i - k)}{N}(D_{1,i} - \mathcal{S})\right)}{1 - \cos\left(\frac{2\pi(p_i - k)}{N}\right)} \ , \tag{2.49}$$

---

[7]Note that extension to analysis of interference caused by multiple subcarriers follows straight-forwardly through including their effects in the summation below.

where it is assumed that the $E_{\text{sc},i}$ and N_i parameters are the same for all users. Differentiating (2.49) with respect to $\mathcal{S}$ and equating it to 0, we have

$$\frac{d \sum_{k \neq p_i} I_{2,i}^2(k)}{d\mathcal{S}} = \sum_{i=1}^{N_{\text{u}}} \sum_{k \neq p_i} \frac{\sin\left(\frac{2\pi(p_i-k)}{N}(D_{1,i}-\mathcal{S})\right)}{\cos\left(\frac{2\pi(p_i-k)}{N}\right) - 1} \frac{2\pi(p_i-k)}{N} = 0 \; . \qquad (2.50)$$

Substituting the cosine and sine terms with the first two terms of their Taylor series expansion, where $p_i - a < k < p_i + a$ as explained in Section 2.4.1, we obtain

$$\sum_{i=1}^{N_{\text{u}}} \sum_{\substack{k=p_i-a \\ k \neq p_i}}^{k=p_i+a} \frac{\frac{2\pi(p_i-k)}{N}(D_{1,i}-\mathcal{S}) - \frac{1}{3!}\left(\frac{2\pi(p_i-k)}{N}(D_{1,i}-\mathcal{S})\right)^3}{-\frac{1}{2}\left(\frac{2\pi(p_i-k)}{N}\right)^2} \frac{2\pi(p_i-k)}{N} = 0 \; , \qquad (2.51)$$

which, after some manipulations, yields

$$\sum_{i=1}^{N_{\text{u}}} \sum_{\substack{k=p_i-a \\ k \neq p_i}}^{k=p_i+a} \left(-2(D_{1,i}-\mathcal{S}) + \left(\frac{2\pi(p_i-k)}{N}\right)^2 \frac{(D_{1,i}-\mathcal{S})^3}{3} \right) \qquad (2.52)$$

$$= \sum_{i=1}^{N_{\text{u}}} -4a(D_{1,i}-\mathcal{S}) + \sum_{i=1}^{N_{\text{u}}} \left(\frac{2\pi}{N}\right)^2 \frac{(D_{1,i}-\mathcal{S})^3}{3} \frac{a(a+1)(2a+1)}{3} \qquad (2.53)$$

$$= \sum_{i=1}^{N_{\text{u}}} -(D_{1,i}-\mathcal{S}) + R(D_{1,i}-\mathcal{S})^3 = 0 \; , \qquad (2.54)$$

where $R = \frac{1}{36}\left(\frac{2\pi}{N}\right)^2(a+1)(2a+1)$. Ordering the terms in (2.54) according to the powers of $\mathcal{S}$, a third order polynomial for $\mathcal{S}$ can be written as

$$N_{\text{u}}\mathcal{S}^3 - 3\sum_{i=1}^{N_{\text{u}}} D_{1,i}\mathcal{S}^2 + \left(-\frac{N_{\text{u}}}{R} + 3\sum_{i=1}^{N_{\text{u}}} D_{1,i}^2 \right)\mathcal{S} - \sum_{i=1}^{N_{\text{u}}} D_{1,i}^3 + \frac{1}{R}\sum_{i=1}^{N_{\text{u}}} D_{1,i} = 0 \; , \qquad (2.55)$$

The only real root of (2.55) is $\mathcal{S}_{\text{opt}}$, and the optimum synchronization point can be found as $\theta_{\text{opt}} = \mathcal{S}_{\text{opt}} - N_{\text{cp}}$.

A critical point is that if there is a set of users $\mathcal{I}_u$ whose $D_{1,i} < \theta_{\text{opt}}$, then the $D_{1,i}$ term in (2.55) needs to be replaced by $D_{1,i} - \theta_{\text{opt}}$ for $i \in \mathcal{I}_u$, and $\mathcal{S}_{\text{opt}}$ needs to be recalculated. This is because for $i \in \mathcal{I}_u$, the received symbol contains samples from the previous symbol,

29

and hence, ICI and ISI occur. Therefore, if $\mathcal{I}_u \neq \emptyset$, it is required to run (2.55) a second time with $D_{1,i}$ modified for $i \in \mathcal{I}_u$ to obtain the correct $\mathcal{S}$. In Section 2.7, the analytical value of θ_{opt} obtained from (2.55) will be verified with computer simulations.

2.7 Simulation Results

Extensive computer simulations are performed. In the simulations, both an AWGN channel and a realistic 6-tap multipath (MP) channel (ITU-R Vehicular A channel model) are considered. Signal-to-noise-ratio (SNR) for user i is defined as $\mathrm{E}\{E_{\mathrm{sc},i}\}/N_0$. PMD is defined as the ratio of number of subcarriers detected as unused although they are used to N. PFA, on the other hand, is the ratio of the number of subcarriers detected as used although they are unused to N. We consider a traffic model where the primary users are continuously transmitting. It is assumed that the scheduling decisions in the primary network remain the same for a certain period of time. The secondary networks sense the spectrum within a portion of this duration and utilize the spectrum opportunities before the scheduling decisions in the primary network change. The simulations target the opportunity sensing aspects of the spectrum, but how the opportunities are utilized is out of the scope of this chapter.

2.7.1 Statistics of (2.17) with Timing Misalignment

The mean and variance of (2.13) for a three user scenario are plotted in Fig. 2.4 and Fig. 2.5, where an AWGN channel is considered. It is observed that theoretical results match well with simulations. While user-1's signal arrives at the receiver with a delay smaller than the CP, user-2 and user-3's signals arrive at the receiver with delays larger than the CP. Figs. 2.4 and 2.5 show that the mean and variance of the decision variable $\left|Y^{(m)}(k)\right|^2$ in unoccupied subcarriers adjacent to the subcarriers of user-2 and user-3 are larger than the noise level due to the timing misalignment problem, which will increase the PFA. Another important observation in these figures is that the variance of the decision variable at the occupied subcarriers of a certain user may increase considerably with the delay experienced

30
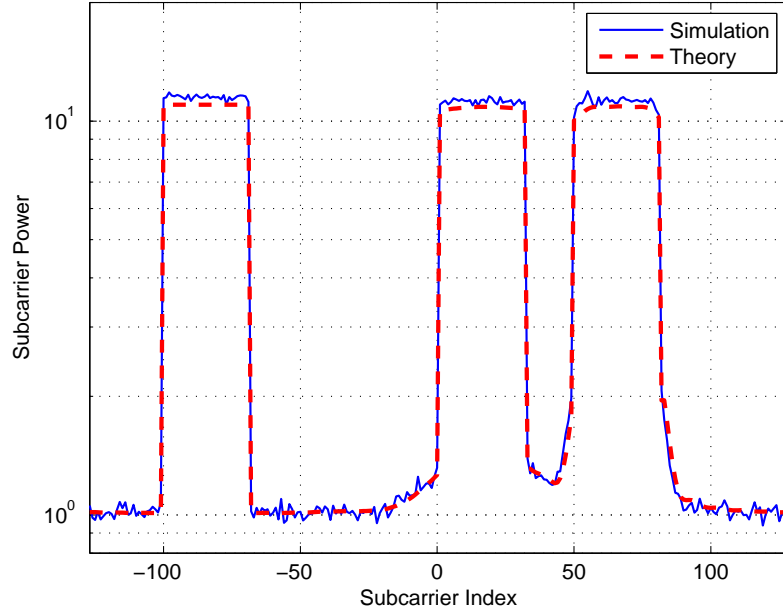
Figure 2.4 Theoretical versus simulated mean of (2.17) with timing misalignment. User delays in terms of samples are $\tilde{\delta}_1 = 10, \tilde{\delta}_2 = 40$, and $\tilde{\delta}_3 = 60$, while the CP length is equal to 32 samples. Subcarriers assigned to users are $\boldsymbol{\Gamma}_1 = [-100, -99, ..., -69], \boldsymbol{\Gamma}_2 = [1, 2, ..., 32], \boldsymbol{\Gamma}_3 = [50, 51, ..., 81]$, respectively.

by that user, which will impact the probability of detection of the occupied subcarriers. How these factors affect the ROCs will be demonstrated in the next section.

2.7.2 Receiver Operating Characteristics With and Without ICI

The ROCs for the three-user scenario in Fig. 2.4 are illustrated in Fig. 2.6 and Fig. 2.7 for two different SNR levels. Both theoretical and simulation results are shown for NBT, while only simulation results are included for NT with $T_{\text{norm}} \in \{0.2, 0.6\}$. For theoretical NBT, (2.43) is used when all the users' delays are within the CP (no ICI), while (2.44) and (2.45) are used if any of the users' delays are larger than the CP (with ICI). The theoretical plots are well aligned with the simulation results, and it is seen that the Chi-square distribution well models the distribution of $\left| Y^{(m)}(k) \right|^2$ with or without ICI. For NBT, when the propagation delay experienced by the users exceeds the CP, the PD corresponding to a certain PFA decrease for all scenarios due to ICI.

31
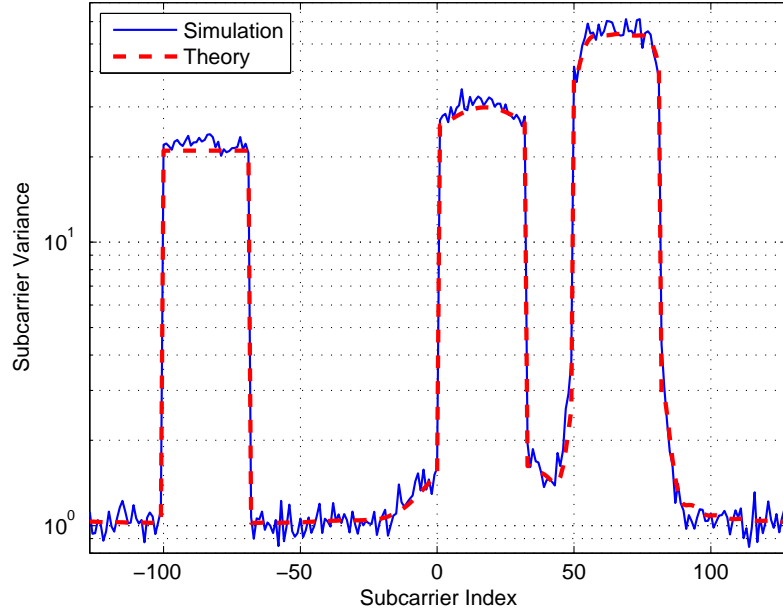
Figure 2.5 Theoretical versus simulated variance of (2.17) with timing misalignment.

When the NTs are used, on the other hand, the thresholds are not specifically conditioned on the PFA values (captured by the x-axis on the plots), but they are set adaptively based on (2.48). Then, the simulation results are averaged over several realizations in order to obtain the average PFA and PD values for a given normalized threshold, which are plotted in Fig. 2.6 and Fig. 2.7. It is observed that when the NT in (2.48) is used, the receiver operates somewhere on the corresponding ROC curves (PD versus PFA relation captured by equations (2.43)-(2.45)) at the same SNR. Note that for larger received signal energies, the threshold ξ increases when an NT is used (i.e., the threshold is set adaptively), while it is constant for NBT. Hence, by using NT, the PFA may be decreased with some acceptable degradation in the PD. For example, for $E_{\mathrm{sc},i}/\sigma^2 = 7$ dB and $T_{\mathrm{norm}} = 0.6$ (with no ICI), we have (PFA, PD) $\approx (0.140, 0.920)$ for NT. When the $E_{\mathrm{sc},i}/\sigma^2$ is increased[8] to 10 dB, with NT, the (PFA, PD) $\approx (0.040, 0.983)$. On the other hand, with NBT that uses the same threshold as in the first case, we would have (PFA, PD) $\approx (0.140, 0.993)$, where 0.993 is only slightly larger than 0.983, but 0.040 is considerably smaller compared to 0.140. Hence,

---

[8]Noise level is kept constant and received signal energies are increased.

32
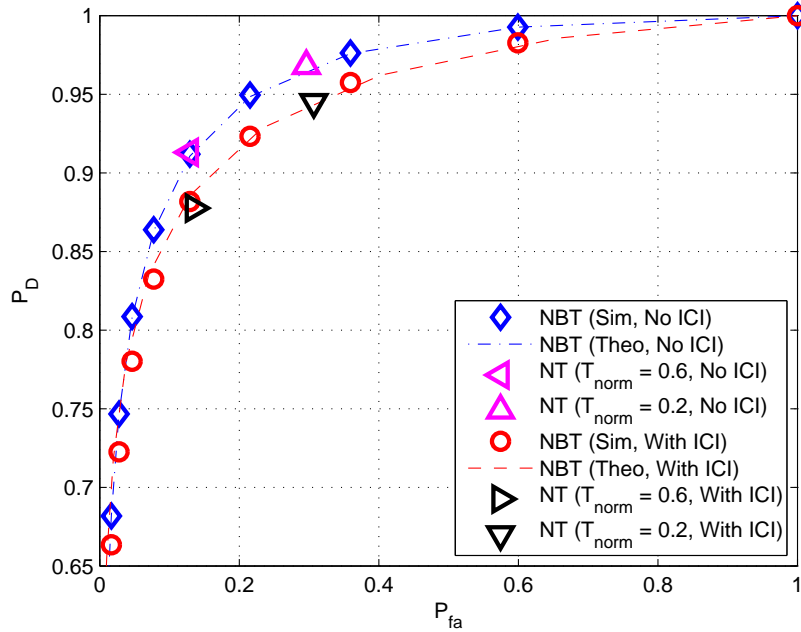
Figure 2.6 ROCs for $E_{\text{sc},i}/\sigma^2 = 7$ dB.

through using an NT, considerable improvement may be obtained in the PFA with some minor PD degradation.

2.7.3 Probability of Opportunity Detection Error with Timing Misalignment

In this section, two different subcarrier assignment schemes (SAS) are considered. The first one is a blockwise assignment (BA), where each block is defined by N_{symb} consecutive OFDMA symbols and N_{sc} consecutive subcarriers. Fig. 2.8 illustrates the blocks that are used in different standards[9]. The two BA schemes used in the simulations are WiMAX UL ASP with $N_{\text{sc}} = 9$ and $N_{\text{symb}} = 6$, and WiMAX UL PUSC with $N_{\text{sc}} = 4$ and $N_{\text{symb}} = 3$. The other SAS considered is a randomized assignment (RA), where each individual subcarrier may be assigned to a different user. The RA scheme employed in the simulations has $N_{\text{sc}} = 1$ and $N_{\text{symb}} = 6$. Although not used in any standard, this RA scheme is included in our simulations to investigate the effect of using small number of subcarriers as an assignment unit.

---

[9]PUSC: partial usage of subchannels, ASP: adjacent subcarrier permutation.

33
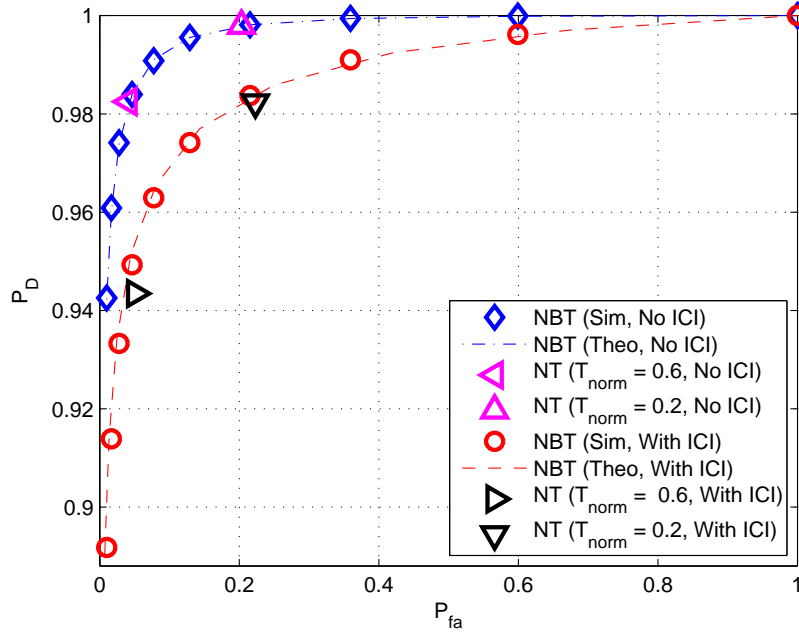
Figure 2.7 ROCs for $E_{\mathrm{sc},i}/\sigma^2 = 10$ dB.

In the simulations, error probability in opportunity detection is computed as the sum of PMD and PFA. For all assignment schemes used, the occupancy rate of the subcarriers is kept at 50% to have equal contribution from PMD and PFA to the total error probability. The maximum delay that the latest arriving user signal can have is $\tau_{\max}$ and it is considered to be between 0 μs and 60 μs, where $\tilde{\tau}_i \sim \mathcal{U}(0, \tau_{\max})$ for all users. Note that $\tau_{\max}$ values greater than 11.2 μs exceed the CP duration.

Fig. 2.9 and Fig. 2.10 demonstrate the error probability for $\tau_{\max}$ values up to 60 μs both for RA and BA, for block sizes 4×3 and 9×6 (shown in Fig. 2.8(c) and Fig. 2.8(d)), respectively. The reason for excluding the simulation results for block sizes given in Fig. 2.8(a) and Fig. 2.8(b) is their numerical closeness to the other two. Both in Fig. 2.9 and in Fig. 2.10, an optimum T_{norm} is used in all cases (see [5] for a detailed analysis of obtaining optimum T_{norm} in different scenarios). It is observed that in RA, ICI has a more destructive effect on the detection performance. The two reasons for the error rates being higher in Fig. 2.10 than

34
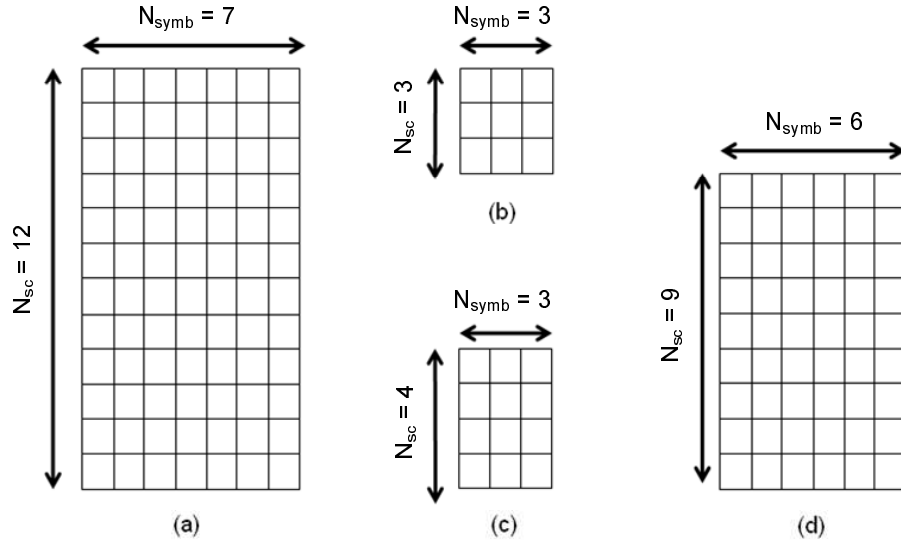
Figure 2.8 Subcarrier assignment schemes in different standards. (a) A typical resource block in LTE, (b) PUSC 1 in WiMAX, (c) PUSC 2 in WiMAX, (d) ASP in WiMAX. For the ASP mode in WiMAX, different options for the block dimensions exist, where $N_{\text{symb}} \in \{1, 2, 3, 6\}$ and $N_{sc} = 54/N_{\text{symb}}$ (i.e., number of subcarriers per block is fixed to 54).

in Fig. 2.9 are that N_{sc} is smaller leading to a higher number of affected empty subcarriers, and N_{symb} is smaller resulting in worse noise averaging.

The results of the error probability versus $\tau_{\max}$ analysis performed for the ESPRIT algorithm (for a block size of 9×6) are displayed in Fig. 2.11. It is observed that there is a considerable performance difference between RA and BA in high SNR values. For low SNR, ESPRIT performance is considerably poor regardless of the subcarrier assignment scheme or the $\tau_{\max}$ value. A comparison of the error probabilities demonstrated in Fig. 2.9 and Fig. 2.11 indicates that the ESPRIT performance is inferior to the energy detection performance with the given set of simulation parameters. The main reason for this fact is that there are only 6 symbols over which the ESPRIT algorithm needs to obtain the covariance matrices it requires. It is found that ESPRIT performance could compete with energy detection only if the same subcarrier assignment were used over a very high number of symbols, so that ESPRIT can compute the covariances reliably. The simulation results that compare

35
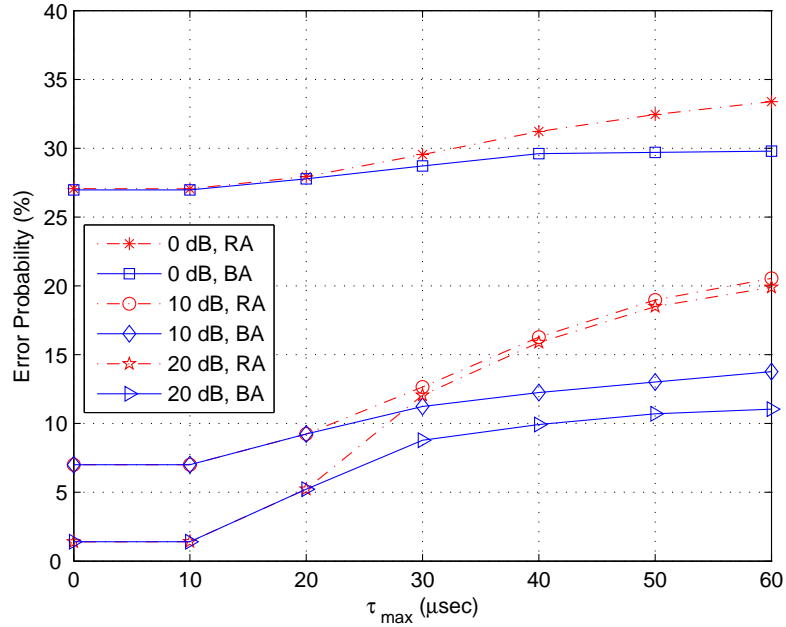
Figure 2.9 Error probability versus τ_{max} for energy detection with blockwise and randomized assignments ($N_{\text{sc}} = 9, N_{\text{symb}} = 6$).

the performances of these two algorithms up to 500 symbols for RA[10], 20 dB SNR, and $\tau_{\text{max}} = 0 \ \mu s$ are plotted in Fig. 2.12. The energy detection curves are obtained for the optimum T_{norm} value for this scenario, which is 0.05, as well as two other non-optimum values. It is shown that ESPRIT can outperform energy detection at a high number of symbols, especially when T_{norm} is not optimized. However, it is worth to note that ESPRIT becomes less desirable at higher number of symbols due to its increased computational complexity.

Another analysis is performed on the variation of the error probability with respect to T_{norm} in order to determine the optimum T_{norm} in different practical scenarios. The error probability versus T_{norm} curves are shown in Fig. 2.13 for BA and in Fig. 2.14 for RA. The curves that correspond to the lowest and highest τ_{max} values considered in the simulations (0 μs and 60 μs) are displayed for SNRs of 0 dB, 10 dB, and 20 dB, where all received

---

[10]Note that actually there is a sensing vs. throughput trade-off in cognitive radio networks, where there exists an optimal sensing time that maximizes the throughput. Due to space limitations, the reader is referred to [19] for further details.
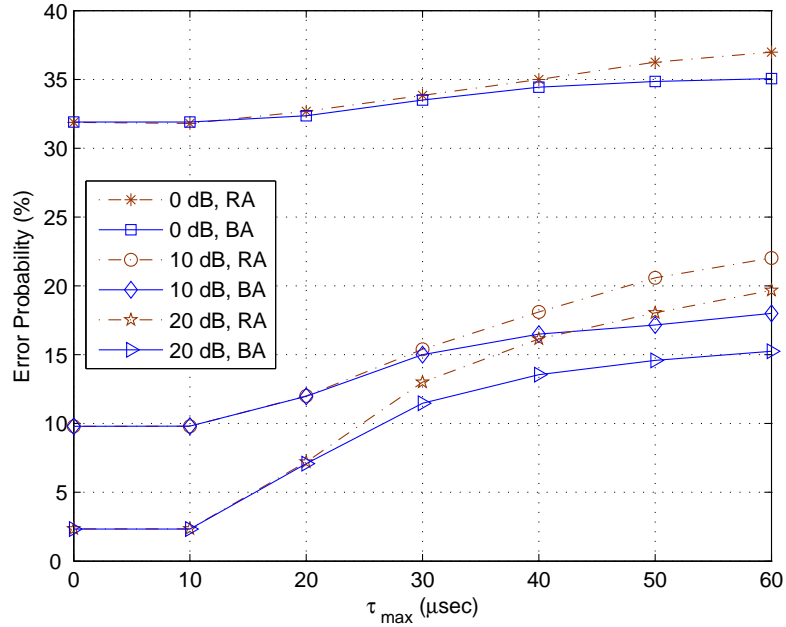
Figure 2.10 Error probability versus τ_{max} for energy detection with blockwise and randomized assignments ($N_{sc} = 4, N_{symb} = 3$).

user signals are assumed to have the same SNR. It is observed that, when SNR is high and τ_{max} is close to 0 μs, the optimum T_{norm} is around 0.05, but a decrease in the SNR or an increase in τ_{max} changes the optimum T_{norm} towards 0.5. Hence, T_{norm} may need to be set adaptively according to the SNR by utilizing the P_{s+n} and P_n measurements.

The error probability versus T_{norm} analysis is performed for different practical macrocell scenarios, as well. In these practical simulations, received user signal powers are distance-dependent due to free space path loss. It is aimed to detect subcarriers of users whose average SNR exceeds 5 dB. Fig. 2.15 shows the error probabilities obtained for BA (block size 9×6), where the distances of 12 users to the secondary receiver are shown in the legend. An important observation in Fig. 2.15 is that the optimum T_{norm} is found to be around 0.05 in all practical scenarios considered, which matched with the high SNR, low τ_{max} case in Fig. 2.14.

The variation of interference power with respect to user delay is investigated in Fig. 2.16 for both AWGN and MP channels. The delays considered are round trip delays (RTDs),
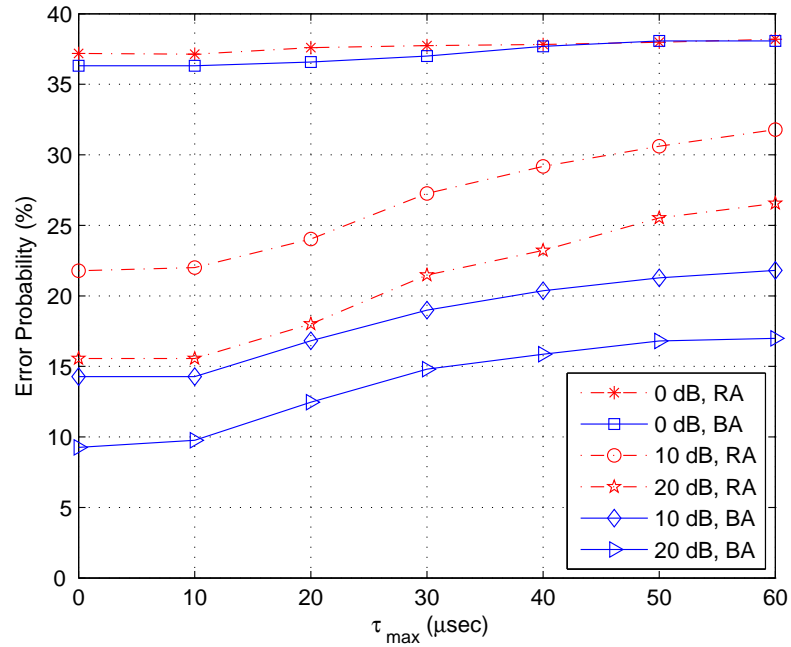
Figure 2.11 Error probability versus $\tau_{\max}$ for the ESPRIT algorithm with blockwise and randomized assignments ($N_{sc} = 9, N_{symb} = 6$).
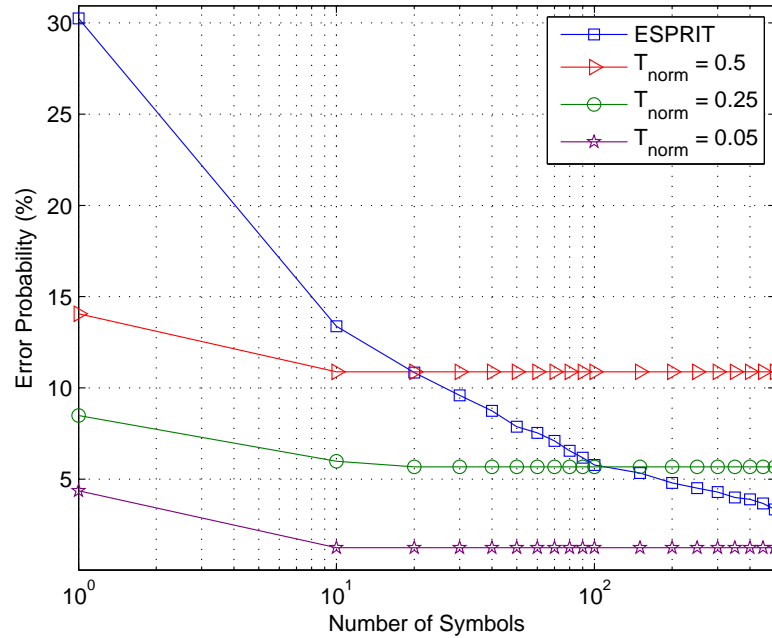
Figure 2.12 Comparison of ESPRIT and energy detection algorithms over increasing number of symbols. T_{norm} values considered for energy detection are 0.50, 0.25, and 0.05.

38
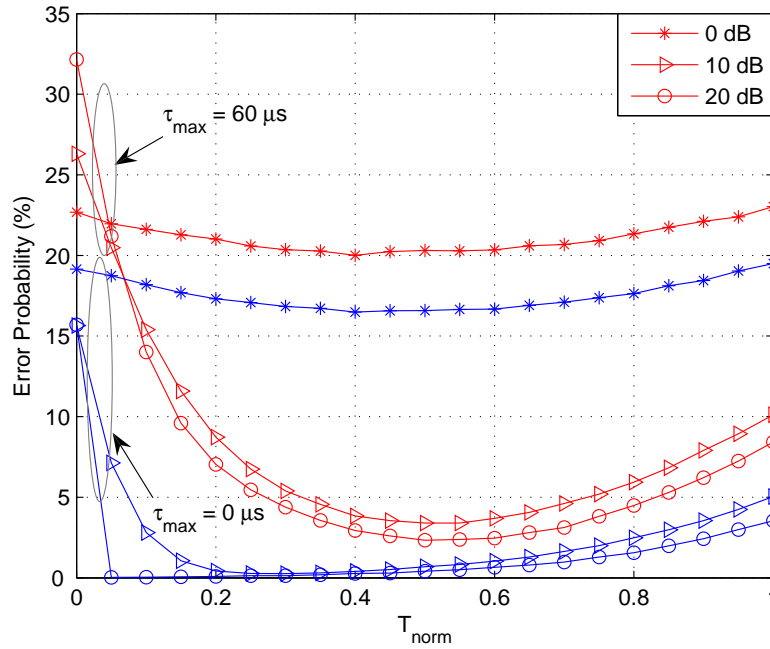
Figure 2.13 Error probability versus normalized threshold for blockwise assignment when all user SNRs are the same; $\tau_{\max} = 0\ \mu s$ and $60\ \mu s$ (for SNR = 20 dB, 10 dB, and 0 dB).
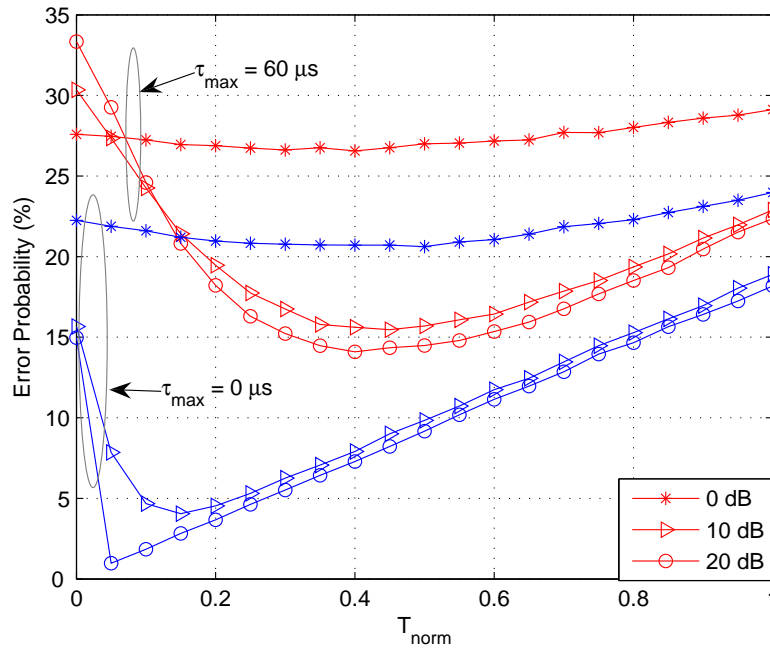
Figure 2.14 Error probability versus normalized threshold for randomized assignment when all user SNRs are the same; $\tau_{\max} = 0\ \mu s$ and $60\ \mu s$ (for SNR = 20 dB, 10 dB, and 0 dB).

39
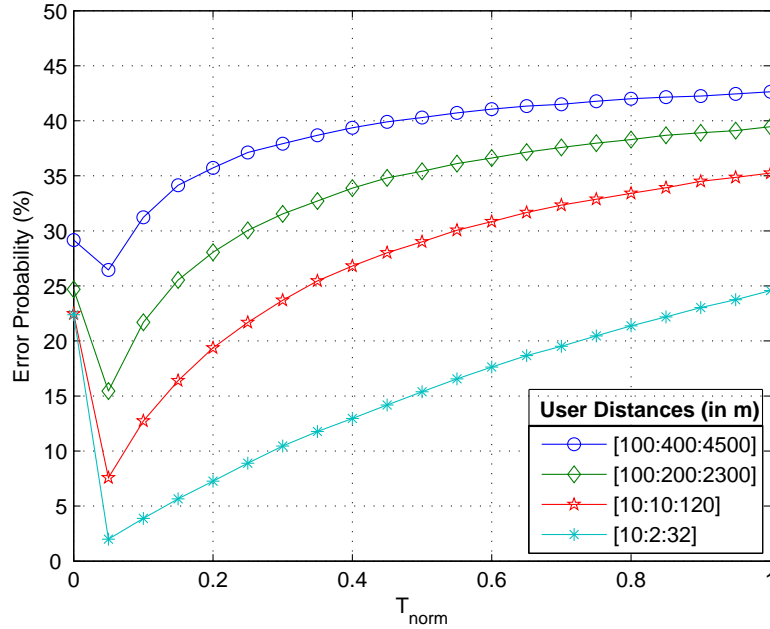
Figure 2.15 Error probability versus normalized threshold for 4 different practical scenarios.

and user signal powers are distance-dependent. Theoretical values for interference power are computed using (2.26), as well, and they validate the simulation results. Note that for the MP channel, interference power is usually higher, and interference is observed even for delays shorter than N_{cp} due to the dispersiveness of the channel. In Fig. 2.16, the delays yielding the highest interference power that are calculated using (2.37) are also indicated. It is observed that (2.37) provides very accurate estimates.

Simulation results for the variation of interference power with respect to the synchronization point (θ) are provided in Fig. 2.17 for case 1, where user distances vary from 150 m to 1800 m (in steps of 150 m), and for case 2, where user distances vary from 500 m to 1600 m (in steps of 100 m). In both cases, all user signal powers are equal. Theoretical values are also obtained using (2.49) and they are shown to match with the simulation results. It is revealed that the point where the interference is minimized (θ_{opt}) may be considerably later than the delay of the first arriving signal, and the gain that can be obtained by optimizing the synchronization point may be as high as 3 dB. In Fig. 2.17, the θ_{opt} values

40
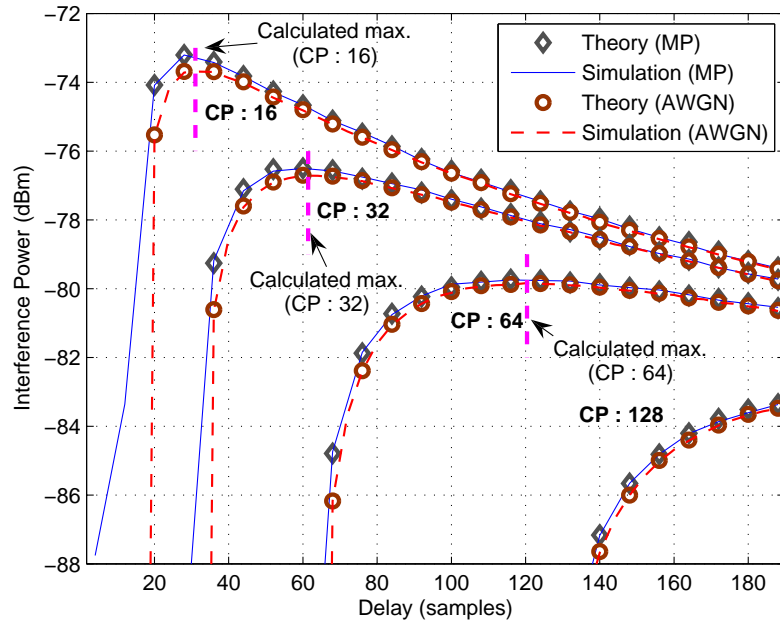
Figure 2.16 Interference versus user delay analysis.
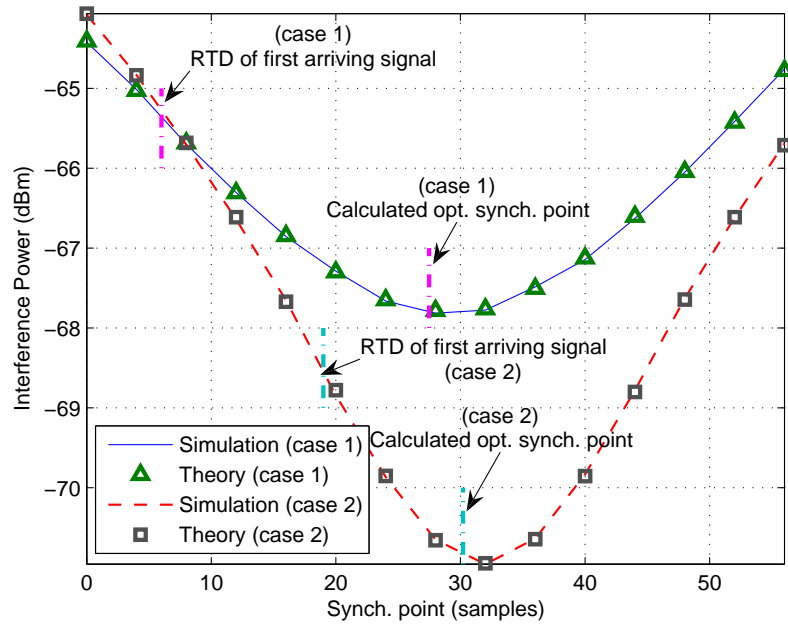
Figure 2.17 Variation of ICI power with respect to synchronization point; N_{CP}=16 samples.
Case 1) User distances (in m): [150:150:1800].
Case 2) User distances (in m): [500:100:1600].

41

derived using (2.55) are indicated, as well. It is observed that (2.55) is rather accurate in estimating θ_{opt}.

2.8 Concluding Remarks

In this chapter, the feasibility of spectrum opportunity detection in UL-OFDMA in the presence of significant timing misalignments is investigated. Energy detection algorithm is scrutinized through detailed theoretical analyses, which are verified through extensive computer simulations. Statistics of the energy detection decision variable are derived in the presence of ICI effects, and are then utilized to obtain the related ROCs. Performance of the energy detector receiver is found to be acceptable, yielding a better performance than the ESPRIT algorithm under the practical system parameters considered. A closed form expression is obtained for the optimum UL-OFDMA synchronization point that minimizes the interference on the cognitive radio. It is shown that it may be at a later point than the arrival time of the earliest primary user's signal.

CHAPTER 3

INTERFERENCE SCENARIOS AND FREQUENCY REUSE FOR NEXT-GENERATION FEMTOCELL NETWORKS

3.1 Introduction

The demand for broadband wireless data rates has been pushing the wireless technology to new horizons. The data rate requirements for the next-generation wireless networks have been specified under the standard referred as the IMT-Advanced, where, peak rates on the order of 1 Gbps are targeted for low-mobility scenarios. Femtocells, which have been recently introduced as a new class of personal-use base stations (BSs) [1]- [3], can help to achieve some of the key requirements of the IMT-Advanced standard. For example, they can improve the peak data rates by more than 40 times and the mean data rates by 200 times according to an analysis in [48]. They also eliminate coverage area problems for indoor scenarios Some other benefits of femtocells include reduced capital and operational expenditure, reduced bandwidth load and power requirements, increased average revenue per user, and deployment in operator-owned spectrum. As illustrated in Fig. 3.1, a femtocell BS (fBS) is connected to the mobile operator's core network through existing broadband Internet connection of the user. A macrocell-associated mobile station (mMS) does not have to be a dual mode terminal in order to communicate both with an fBS and a macrocell BS (mBS)[1].

Besides their uses for enhancing communications, femtocells can interact with *smart* home appliances and personal computers inside the house. This way, an fBS-centric network of home electronics can be formed, which would enable the users to remotely connect to

---

[1]Note that the abbreviations H-UE, HNB, M-UE, and NB are used in 3GPP documents for referring to femtocell mobile station (fMS), fBS, mMS, and mBS, respectively.

43

any electrical device at their homes as shown in Fig. 3.1 [2]. Femto Forum, which is a business organization established in July 2007 to promote femtocell deployments, provides some non-communication-oriented femtocell applications in [50] that might be attractive to consumers. In these exemplary applications, femtocell enables users to

- Automatically synchronize their music collection on their mobile device with their home PC when a they return home,

- Control their TV from their mobile device,

- Leave virtual fridge notes to be delivered when the recipient returns home,

- Remotely control home appliances such as air conditioning when out of the house.

---

[2]The reader is referred to [49] for an in depth discussion of controlling home appliances in a smart home environment.
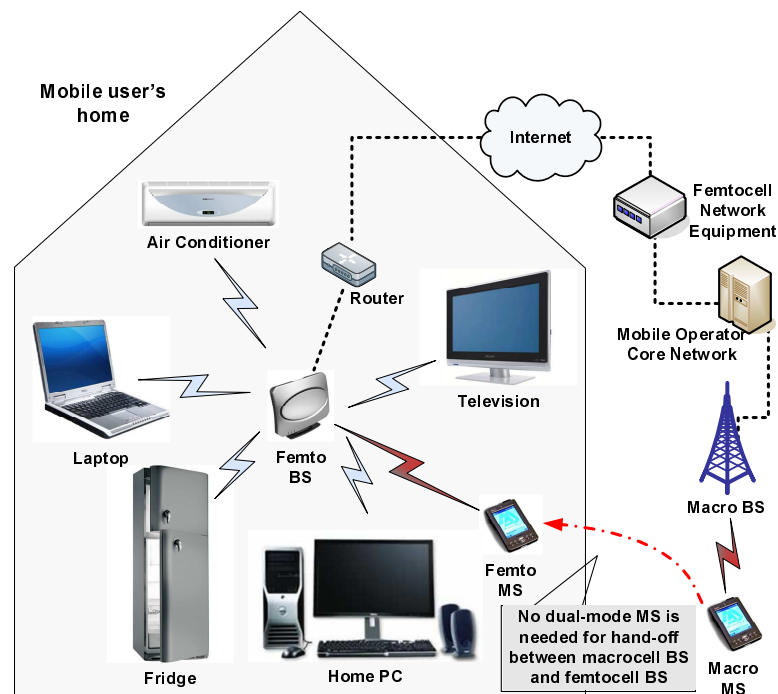
Figure 3.1 Femtocell deployment at homes. Connection between the macrocell and femtocell is established through the Internet. Home appliances can be controlled by the user through the fBS.

Femtocell networks have been studied extensively under the 3GPP standard (see e.g., [51, 52], and the references therein), where wideband code division multiple access (W-CDMA) is used as the physical layer technology. Even though system capacity and performance have been analyzed for macrocells and femtocells in the presence of co-channel interference (CCI) in [1, 3, 30], it can be said that these studies are more specific to CDMA based systems. There are only limited studies on orthogonal frequency division multiple access (OFDMA) based femtocell networks (e.g., based on the LTE or WiMAX standards[3]), which offer greater flexibility in terms of allocation of frequency resources. In this work, the focus is on the next-generation OFDMA based co-channel femtocells, which share the same spectrum with the macrocell network and aim an efficient utilization of spectrum resources while causing minimum interference to the macrocell network. Some operators summarized their views regarding LTE femtocells in the 3GPP standard as *"femtocell can actively attempt to configure its cell resources to minimize impacts to the operator-deployed cells, and to avoid interference interactions with other home cells in its vicinity"* [53] and *"in order to maximize system capacity and throughputs in the uplink, the fBS could decide to schedule its users to transmit on those resource blocks that experience the lowest other cell/channel interference"* [54].

Some related work on avoiding interference in OFDMA networks through spectrum sensing [20] and through intelligent radio resource allocation [55, 56] is available in the literature in the context of cognitive radio systems; however, these work do not consider system-specific issues related to femtocells.

Significant improvements in throughput per unit area have been demonstrated in [2] when OFDMA-based WiMAX femtocells are used (on the order of 15 times throughput improvement for dense-deployments in large cells); however, co-channel interference was stated as an important factor that limits the overall network performance. In [57], trade-offs between public access and private access were compared for WiMAX femtocells through realistic system-level simulations, and public access was shown to yield considerably larger

---

[3]WiMAX uses OFDMA both in downlink (DL) and uplink (UL), while LTE employs OFDMA in DL and single-carrier frequency division multiple access (SC-FDMA) in UL.

throughput due to reduced interference. It was discussed in [58] that the throughput of a naïve co-channel WiMAX femtocell deployment may suffer a lot from the interference; hence, an interference avoidance technique that uses a dynamic frequency planning technique was introduced, which considerably improves the throughput performance.

The major goal in this chapter is to introduce an interference avoidance framework between a femtocell and the mMSs, which is based on not using the resource blocks occupied by closely located mMSs. Availability of macrocell frequency scheduling information is considered, and this information is effectively utilized in conjunction with spectrum sensing. Moreover, inter-carrier interference (ICI) from macrocell UL to the femtocell UL is analyzed. The variation of ICI is with respect to mMS-to-fBS distance is investigated via simulations, and how ICI affects the decisions about UL spectrum opportunities at a femtocell is demonstrated.

The rest of the chapter is organized as follows. The system model is provided in Section 3.2. CCI and ICI problems in the co-channel femtocell deployment are discussed in Section 3.3. In Section 3.4, the proposed CCI avoidance framework is introduced. Simulation results are demonstrated in Section 3.5. Section 3.6 concludes the chapter.

3.2   System Model

Since both the macrocell and femtocell networks considered are OFDMA based, their signals can be modeled in the same way. Also, since the downlink signal has a model that is similar to any of the uplink user signals (except for the frequency scheduling), only the UL signal model will be given. Consider an OFDMA system with N_u users in the UL. The sampled time domain signal at the transmitter of user i can be written as

$$x_i^{(m)}(n) = \sqrt{P_{\mathrm{tx},i}} \sum_{k \in \mathbf{\Gamma}_i} X_i^{(m)}(k) e^{\frac{j 2\pi k n}{N}} \ , -N_\mathrm{cp} \leq n \leq N - 1, \tag{3.1}$$

where m is the symbol index, $P_{\mathrm{tx},i}$ is the transmit power for user i, $k \in \mathbf{\Gamma}_i$ is the subcarrier index, $\mathbf{\Gamma}_i$ is the set of subcarriers of length N_i assigned to user i out of N total subcarriers,

46

N_{cp} is the length of the cyclic prefix (CP), and $X_i^{(m)}(k)$ is the data on the kth subcarrier and mth symbol of the ith user.

The time domain aggregate received signal is the superposition of signals from all users, each of which propagates through a different multipath channel and arrives at the receiver with a delay $\tilde{\delta}_i = \lceil N\tilde{\tau}_i/T \rceil$, where $\tilde{\tau}_i$ is the propagation delay experienced by user i, and T is the duration of the useful part of the symbol. Then, aggregate discrete-time received signal can be expressed as

$$y(n) = \sum_{i=1}^{N_{\mathrm{u}}} y_i(n) + w(n), \tag{3.2}$$

where $w(n)$ denotes the additive white Gaussian noise (AWGN), and

$$y_i(n) = \sqrt{P_{\mathrm{rx},i}} \sum_{l=0}^{L-1} \alpha_i^{(m)}(l) \times \sum_{m=-\infty}^{\infty} x_i^{(m)}\Big(n - D_{l,i} - m(N + N_{\mathrm{cp}})\Big), \tag{3.3}$$

where $P_{\mathrm{rx},i}$ is the received power for user i, L denotes the total number of multipath components (MPCs), $\alpha_i^{(m)}(l)$ is the lth MPC for user i, and $D_{l,i} = \lceil N\tau_{l,i}/T \rceil + \tilde{\delta}_i$, where $\tau_{l,i}$ is the delay of the lth MPC for user i. If $D_{l,i} \leq N_{\mathrm{cp}}$, the frequency domain signal for the kth subcarrier of user i is given by

$$Y_i^{(m)}(k) = \sqrt{E_{\mathrm{sc},i}} X_i^{(m)}(k) \sum_{l=0}^{L-1} \alpha_i^{(m)}(l) e^{-\frac{j2\pi k D_{l,i}}{N}} , \tag{3.4}$$

where $E_{\mathrm{sc},i}$ is the average received energy per subcarrier for user i, which is equal to $P_{\mathrm{rx},i}$. This implies that the received symbol is only a phase rotated version of the transmitted symbol.

3.3   CCI and ICI Issues in Femtocell Deployments

3.3.1   Deployment Configurations

There are two common spectrum access approaches for femtocell deployments: 1) Dedicated channel access, and 2) Co-channel access. For dedicated channel operation, femtocells are assigned a separate channel than that of the macrocell. Even though this approach

47

mostly eliminates potential interference from the macrocell[4], frequency resources are not efficiently utilized. Co-channel deployment enables more efficient utilization of the available spectrum, where all the frequency resources of the macrocell are re-used only by the few users of the femtocell. Co-channel deployments have been commonly preferred in the prior-art works on femtocell networks due to more efficient utilization of the spectrum resources (see e.g., [1, 30, 57]). For example, [1] reports simulation results with co-channel femtocell access, where the median of the system-wide sum-throughput improves by nearly 250 b/s/Hz with respect to a scenario without femtocells. However, co-channel interference still remains a critical problem, especially for scenarios where there are mMSs in the vicinity of a femtocell. In the access mode referred as the closed-subscriber-group (CSG) mode [51], close-by mMSs are not allowed to make hand-off to the femtocell network. Especially for femtocells on the edge of the macrocell, this implies significant interference concerns between the mMSs and the femtocell. This is because during macrocell downlink, mMSs will be interfered significantly by the femtocell, while during macrocell uplink, mMSs will be causing significant interference to the femtocell (see e.g., the discussion on *dead zones* in [1]). In [3, 57], it has been shown that due to such interference problems, open access femtocells (which allow the hand-off of close-by mMSs to the femtocells) will provide better throughput compared to CSG type of femtocells. However, open-access approach may also have some concerns such as privacy issues, reduction of available bandwidth per femtocell user, extra burden on the femtocell owner's backhaul connection etc. One of the contributions of the present work is a method for handling the interference from close-by mMSs, by avoiding to use their frequency resources at the femtocell network, which will be discussed in more detail in Section 3.4.

3.3.2 CCI Scenarios for mMSs

As discussed in the previous subsection, co-channel implementation brings the advantage of efficient spectrum usage. However, it also results in CCI between the femtocell(s) and the

---

[4]Femtocells may still observe adjacent channel interference from the macrocell.

Figure 3.2 All possible interference scenarios related to femtocell communications.
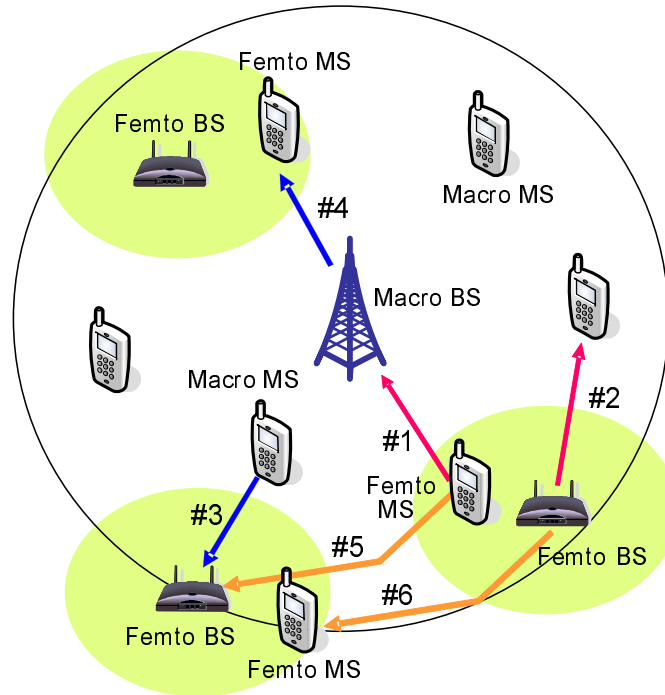
	Interference		UL-DL
	From	To	
#1	Femto MS	Macro BS	UL
#2	Femto BS	Macro MS	DL
#3	Macro MS	Femto BS	UL
#4	Macro BS	Femto MS	DL
#5	Femto MS	Other Femto BS	UL
#6	Femto BS	Other Femto MS	DL

macrocell in various ways. In Fig. 3.2, different CCI possibilities are listed according to their sources, their targets, and whether they occur in the DL or the UL. Interference scenarios #1−#2 involve the CCI caused by the femtocell network to the macrocell network, scenarios #3 − #4 involve the CCI caused by the macrocell network to the femtocell network, and scenarios #5 − #6 are the CCI scenarios between close-by femtocell networks. All these interference scenarios can be considered for both time division duplex (TDD) and frequency division duplex (FDD) systems. It should be noted that these scenarios are based on the rule that femtocell is not allowed to be in DL while macrocell is in UL (in TDD systems),

49

or femtocell cannot use the UL frequency band of the macrocell for DL (in FDD systems). In this chapter, we consider scenario #3, which is the interference to an fBS due to the UL transmission of macrocell MSs, as well as #4, which is the interference from the mBS to the fMSs.

The distance between an mMS and a femtocell network may be as large as twice the cell radius. This suggests that even with co-channel operation, CCI between a femtocell network and some far away mMSs may be insignificant. Hence, both in UL and DL, a femtocell network may intelligently utilize the resource blocks of these far away mMSs, and avoid co-channel operation with close-by mMSs in order to minimize the CCI problem. On the other hand, since mBS is located at the center of the macrocell, its distance to any particular femtocell is smaller than the cell radius. Hence, the received interference by the femtocell is considerably strong and it needs to be cancelled at the fMSs. Some recommendations for reducing these interference problems have been discussed in [51]. For example, intelligent power control techniques may be employed by an fBS to manage interference received from the macrocell or the neighboring femtocells. Open access operation is also described as a possible solution to handle interference to/from a close-by mMS. Details of the method that we propose to address CCI will be presented in Section 3.4.

3.3.3 ICI in the Uplink

A different type of interference that may be observed in next generation femtocell deployments is the inter-carrier-interference (ICI) [1, 34, 59]. It is specific to the uplink and it is caused by the timing misalignment of mMS signals at the femtocell BS. Typically, the mMSs get synchronized to the mBS in the uplink through a ranging process, where the mBS determines and announces the instant to start transmission for each mMS. Since such a synchronization mechanism is not applicable for the fBS, the mMS signals arrive at the fBS with different delays due to their different distances to the fBS, as illustrated in Fig. 3.3(b).

50

Assuming that the femtocell is synchronized to the first arriving mMS signal in the uplink, if the delays of some of the other mMSs exceed the CP of the femtocell symbol (see Fig. 3.3(c)), orthogonality between the subcarriers is lost. This causes inter-carrier interference in the resource blocks that can be reused by the femtocell network, as illustrated in Fig. 3.3(d). This is especially a critical problem for femtocells that are located closer to the macrocell edge [34] due to the increased spread of the mMS arrival times.
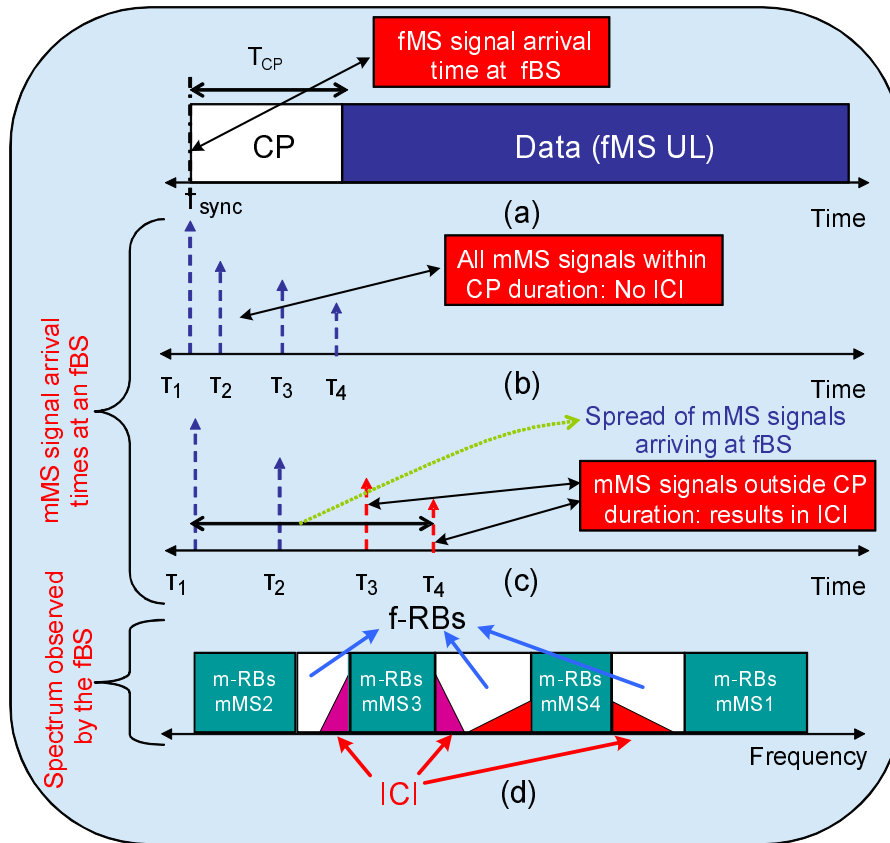
Figure 3.3   The relation between the arrival times of mMS signal delays, CP-size, and ICI. (a) Structure of a femtocell symbol, (b) Signal arrival times from four different mMSs at an fBS that are within the CP, (c) mMS signal arrival times that exceed the CP, and (d) Illustration of ICI due to delays larger than the femtocell CP size. (m-RB: Macrocell resource block, f-RB: Femtocell resource block)

When there are some $D_{l,i} > N_{\mathrm{cp}}$, the received signal on the kth subcarrier of user i can be written by getting the FFT of (3.3) as follows [27]

$$Y_i^{(m)}(k) = \frac{\sqrt{E_{\mathrm{sc},i}}}{N} \sum_{l=1}^{L} \alpha_i^{(m)}(l) \times \left\{ \sum_{n=0}^{D_{l,i}-N_{\mathrm{cp}}-1} x_i^{(m-1)}(n+N+N_{\mathrm{cp}}-D_{l,i})e^{-\frac{j2\pi kn}{N}} \right.$$
$$\left. + \sum_{n=D_{l,i-N_{\mathrm{cp}}}}^{N-1} x_i^{(m)}(n-D_{l,i})e^{-\frac{j2\pi kn}{N}} \right\} . \quad (3.5)$$

After plugging (3.1) into (3.5) and some manipulation, we have

$$Y_i^{(m)}(k) = \sqrt{E_{\mathrm{sc},i}} \sum_{l=0}^{L-1} \alpha_i^{(m)}(l) \left\{ S_{\mathrm{d},i,l}(k) + I_{i,l}(k) \right\}, \quad (3.6)$$

where the desired signal and the total ICI are respectively given as

$$S_{\mathrm{d},i,l}(k) = X_i^{(m)}(k) K_{i,l}(k) e^{\frac{-j2\pi k D_{l,i}}{N}} \quad (3.7)$$

$$I_{i,l}(k) = \frac{1}{N} \sum_{\substack{p\in\mathbf{\Gamma}_i \\ p\neq k}} \underbrace{\left[\frac{1 - e^{\frac{j2\pi(p-k)(D_{l,i}-N_{\mathrm{cp}})}{N}}}{1 - e^{\frac{j2\pi(p-k)}{N}}} \right]}_{h_i(p,k)} \underbrace{\left(-X_i^{(m)}(p)e^{-\frac{j2\pi p D_{l,i}}{N}} + X_i^{(m-1)}(p)e^{\frac{j2\pi p(N_{\mathrm{cp}}-D_{l,i})}{N}} \right)}_{g_i(p)},$$

$$(3.8)$$

where

$$K_{i,l}(k) = \frac{N - D_{l,i} + N_{\mathrm{cp}}}{N} \times \mathcal{I}(i,k) , \quad (3.9)$$

with $\mathcal{I}(i,k)$ denoting an indicator function given by

$$\mathcal{I}(i,k) = \begin{cases} 1 , & \text{if } k \in \mathbf{\Gamma}_i , \\ 0 , & \text{if } k \notin \mathbf{\Gamma}_i . \end{cases} \quad (3.10)$$

The user distance (d_i) has two opposing effects on the ICI power. Since user delays are directly proportional d_i through $D_{1,i} = d_i/(c\,T_s)$, where c is the speed of light, and T_s is the

52
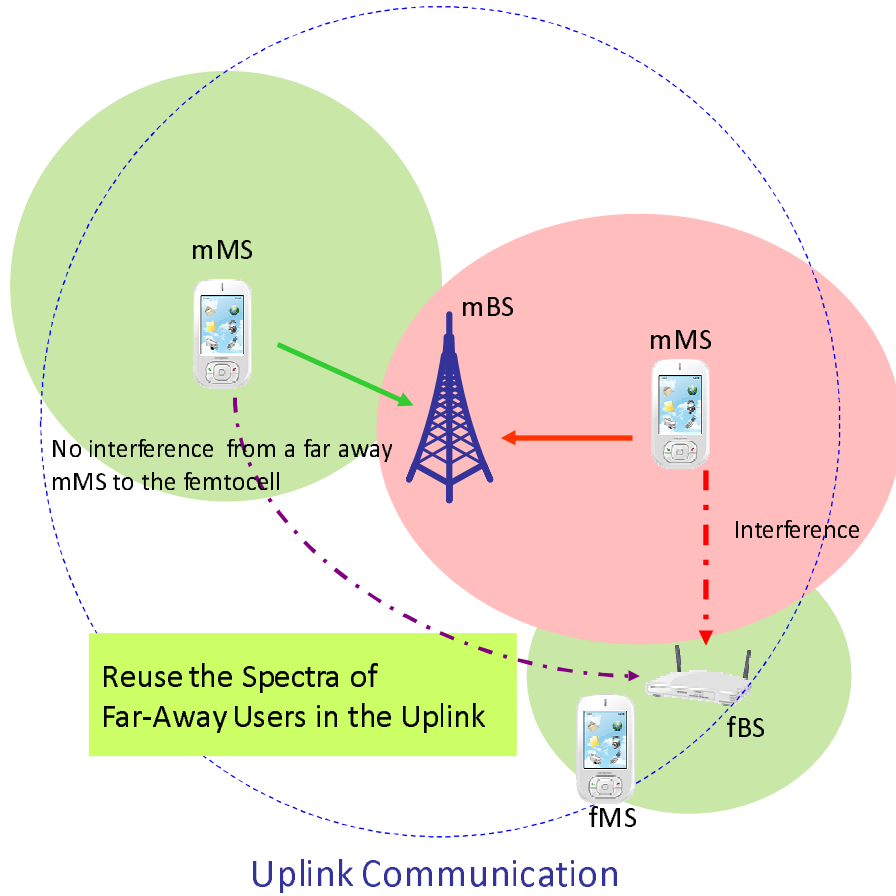
Figure 3.4 Femtocell communications in the uplink.

sampling time, a longer distance leads to a larger delay and hence a stronger ICI. On the other hand, since $E_{sc,i}$ also depends on d_i through $E_{sc,i} = P_{tx}\lambda^2/\left((4\pi)^2 d_i^\gamma\right)$, where λ is the wavelength of the transmitted signal, and γ is the path loss exponent, weaker ICI should be observed at large distances. Therefore, it is expected that the ICI power will be maximized at a certain distance and then will start decreasing with d_i.

Knowledge about the variation of received signal as well as ICI powers with respect to distance can be especially useful in the following specific scenario. Assume that the macrocell BS provides the fBSs not only with the mMS scheduling information but also with the geographical coordinates of the mMSs. Moreover, the fBSs are not capable of spectrum sensing, which means that, for determining the spectrum opportunities, they solely depend on the information that they receive from the mBS. In this scenario, the fBS

mMS

No interference from the
femtocell to a far away mMS

mBS

mMS

Reuse the Spectra of
Far-Away Users in the Downlink

fBS

fMS

Downlink Communication
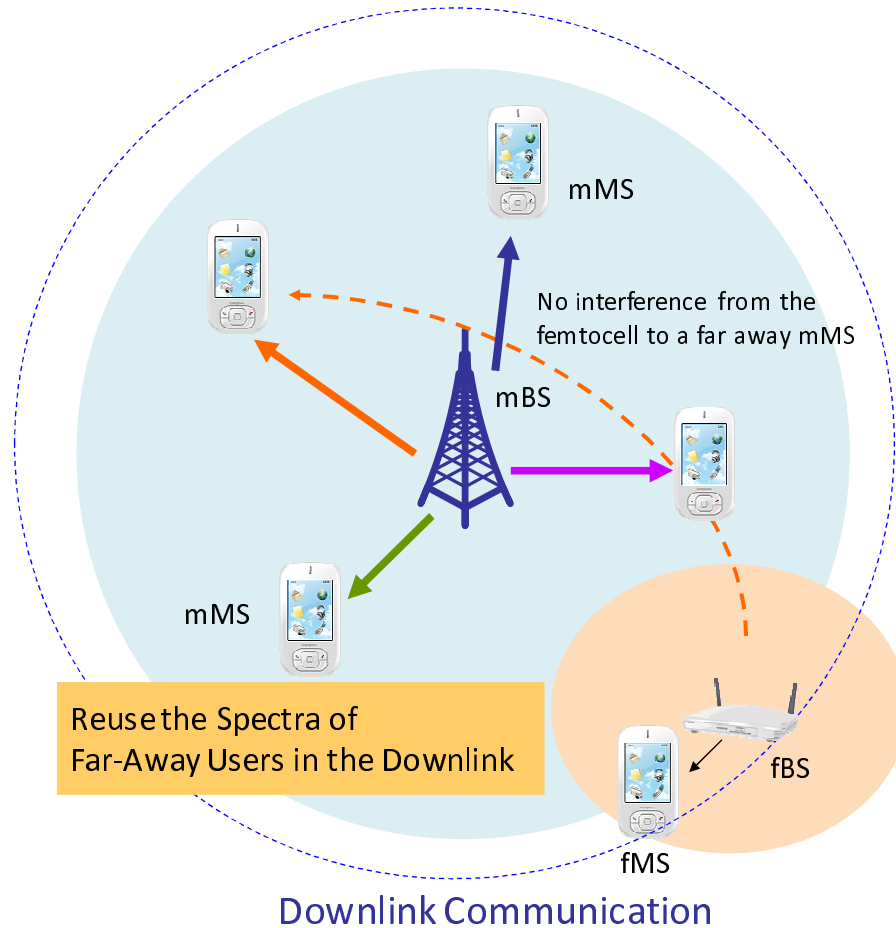
Figure 3.5   Femtocell communications in the downlink. Femtocell senses the spectrum
during UL, identifies the close by users through UL scheduling information, and avoids
using their spectrum specified in DL scheduling information.

can determine the usable occupied resource blocks according to the received signal power

versus distance information. The unoccupied resource blocks that should be avoided due

to ICI, on the other hand, can be found according to the ICI versus distance information.

3.4   Framework for Co-Channel Femtocell Operation

In a CSG femtocell deployment, the potential CCI problem between the femtocell and

mMSs both in UL and DL can be prevented by ensuring that femtocell avoids using the

macrocell resource blocks that belong to nearby mMSs as illustrated in Fig. 3.4 and Fig. 3.5
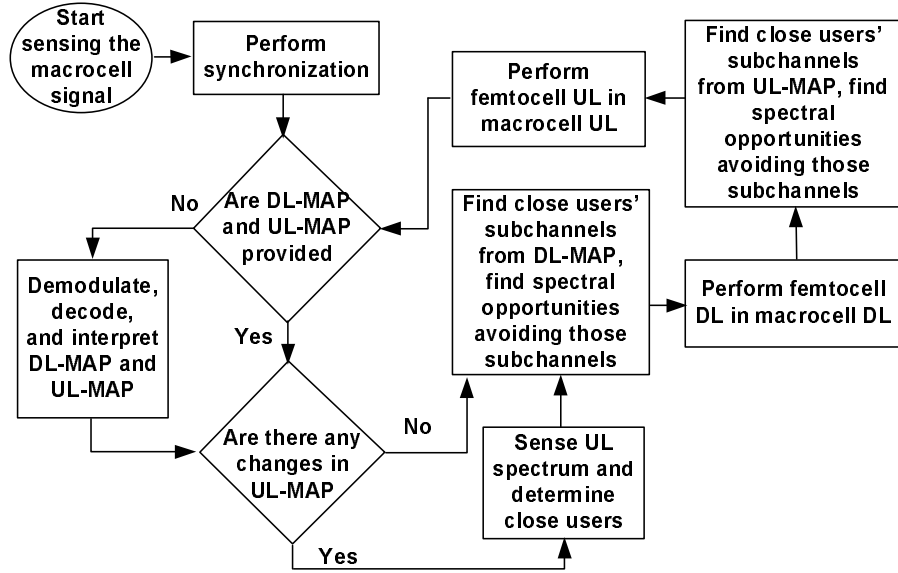
Figure 3.6 Simplified flowchart for femtocell implementation. As an example, an IEEE 802.16e WiMAX system is considered, and DL-MAP/UL-MAP information are utilized.

in a simple way. A basic flowchart of the proposed co-channel femtocell implementation is provided in Fig. 3.6.

The steps of the CCI avoidance based framework that we propose for the UL can be summarized as follows. First, the fBS receives the mMS scheduling information from the mBS. Then, it performs spectrum sensing for finding the occupied parts of the spectrum, which are supposedly the resource blocks of nearby mMSs and determines the spectrum opportunities by comparing the sensing results with the scheduling information. Finally, the fBS schedules its fMSs over the spectrum opportunities determined.

The main points of handling the CCI in the downlink, on the other hand, can be summarized as follows:

- In the uplink, fBS determines the occupied UL resource blocks via spectrum sensing and utilization of the UL scheduling information. Sources of high signal power are labeled as closely located users.

- The UL scheduling information indicates which resource blocks belong to which user. This information can be used to individually identify each closely located user.

55

- Utilizing the DL scheduling information obtained from the mBS, the DL resource blocks that belong to the identified closely located users are found.

- fBS avoids using the resource blocks of close-by users not to cause any interference to them in the DL. The interference from the mBS that hits the fMSs, on the other hand, is cancelled via advanced cancellation methods by the fMSs.

An example for the CCI cancellation methods that can be employed by the fMSs is introduced in [60], where a Least Mean Square (LMS) Maximum Likelihood Estimation (MLE) method is proposed to estimate the time varying channels and the transmitted symbols simultaneously. Also, an MLE based joint demodulation algorithm is provided in [10] for receivers with multiple antennas where availability of reliable channel estimates is assumed. A detailed discussion of these cancellation methods, however, is beyond the scope of this chapter.

In the remainder of this section, two critical steps of the proposed co-channel femtocell operation framework will be discussed.

3.4.1 Obtaining Scheduling Information from the mBS

Scheduling information of mMSs determined by an mBS indicates which resource blocks are used by which mMSs. We consider two possible methods for the fBSs to obtain the scheduling information of mMSs from the mBS. These two methods are receiving the scheduling information through the backhaul, and capturing the scheduling information over-the-air.

3.4.1.1 Communication of the Scheduling Information over the Backbone

As a first option, the fBS may obtain the scheduling information of the mMSs over the backbone. In this method, upon initialization, fBS establishes a secure and stable backhaul connection to the operator network and obtains information about the mMS resource blocks. Depending on the availability of geo-location information, the mMS scheduling information provided to an fBS can be limited to the mMSs that are at a certain neighborhood of that

56
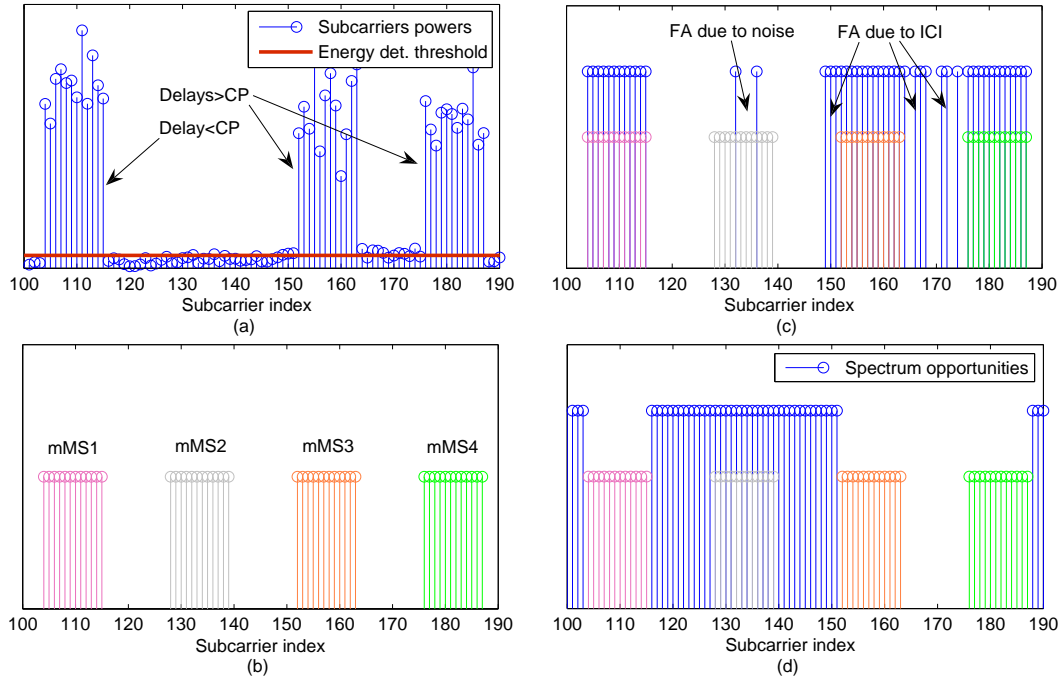
Figure 3.7 Combining scheduling information with spectrum sensing results. (a) Received subcarrier powers and the energy detection threshold, (b) Scheduling information for multiple mMSs, where an LTE resource block size of 12 subcarriers is considered. (c) Energy detection results matched with scheduling information, false alarms occur due to noise and due to ICI, (d) Spectrum opportunities detected.

fBS. The mBS needs to make and then deliver the scheduling decision well ahead of the scheduled transmission, the *ahead time* being greater than the latency of the backhaul.

Because the large ahead time makes it difficult for a channel dependent scheduler to capture instantaneous channel variation, efficiency of such a scheduler is likely to be degraded. Also delivery of scheduling information consumes precious bandwidth of the backhaul, which otherwise could be used to deliver the actual data. One possible improvement to address this efficiency problem is to make ahead scheduling decision (and accompanied sensing and comparison) only when it is necessary. For example, it can be done only in the following cases: initialization of fBSs, handoff of mMSs from/to neighboring mBSs, significant change of channel status, interference level, or resource requests, etc. Most of the other times, channel dependent scheduler could make scheduling decision considering

57

the instantaneous channel status. Resource sharing between the mBS and the fBS can be made semi-static based on the most recent scheduling that was accompanied by sensing and comparison.

Note that as an alternative to an fBS making scheduling decisions (based on its spectrum sensing results and scheduling information from the mBS), the spectrum sensing results of the femtocell may also be communicated to the macrocell network over the backhaul. Then, the macrocell network may make global scheduling decisions and communicate these back to the femtocells. However, considering large number of femtocells, communication of such information may be costly, and an autonomous operation of the femtocell to make its own scheduling decisions may be more practical.

In order to lower the burden of spectrum sensing for the femtocell and to limit the information storage and comparison overhead for the network (such as in the latter scenario discussed above), the scope of sensing, information storage, and comparison may be limited to an agreed time interval that is communicated between an fBS and the macrocell network. The agreement can be made such that the spectrum is sensed for only a certain amount of absolute time or a certain number of frames, slots, or transmission time intervals (TTIs) with respect to a particular mBS or fBS in the neighborhood. The scope of spectrum sensing can be further limited in the frequency domain to a certain set of resource blocks (RBs) or subcarriers to further decrease the burden of spectrum sensing.

3.4.1.2 Obtaining the Scheduling Information Over the Air

In the second method, the M-UE scheduling information is received from the mBS over the air. For this purpose, fBS may connect to the mBS as an M-UE, and use this connection in order to obtain the scheduling information. For example, the DL/UL-MAPs, which carry the scheduling information of the macrocell mobile stations, are not encrypted in WiMAX systems. If such information is made available over-the-air in next-generation 3GPP standards, it can be used for improving the spectrum opportunity detection results at femtocells.

58

3.4.2 Jointly Utilizing Scheduling Information and Spectrum Sensing Results

In a well designed OFDMA system, it is expected that almost all resource blocks are allocated to users. Therefore, scheduling information that the fBS obtains from the mBS would normally indicate that the spectrum is mostly occupied. However, since many of the mMSs are far away from the fBS, their resource blocks can still be utilized at the femtocell. Through spectrum sensing, an fBS can detect resource blocks that are either not used by the macrocell network, or belong to far away users.

The occupied parts of the UL spectrum can be found by simple means such as energy detection. Energy detection is performed by taking the Fourier transform of the received time domain signal $r(t)$, which yields a $1 \times N$ frequency-domain sample vector $\mathbf{r}_{\mathrm{rec}}$. Then, its magnitude squared is computed, and compared with an energy detection threshold $\xi_{\mathrm{thrs}}^{(\mathrm{ED})}$. Energy detection outputs for all the received subcarriers can be written as

$$\mathbf{\Gamma}_{\mathrm{ED}} = \mathrm{U}\Big(|\mathbf{r}_{\mathrm{rec}}|^2 - \xi_{\mathrm{thrs}}^{(\mathrm{ED})} \Big), \tag{3.11}$$

where $\mathrm{U}(\mathbf{x})$ denotes the unit step function that individually applies to all the elements of a vector $\mathbf{x}$, and $\mathbf{\Gamma}_{\mathrm{ED}}$ is a $1 \times N$ vector with elements $\in \{0, 1\}$ (a 0 implies that the subcarrier is sensed as unoccupied, while a 1 implies that the subcarrier is sensed as occupied).

Once the spectrum sensing results are available, the fBS may compare the spectrum sensing results with the UL scheduling information to decide about the spectrum opportunities. Denoting the scheduling vector of a mMS-j with $\mathbf{\Gamma}_{\mathrm{sch}}^{(j)}$ (elements of the scheduling vector are 0s and 1s), the decision for occupied resource blocks can be made as follows

$$\mathbf{\Gamma}_{\mathrm{used}} = \sum_{j=1}^{N_{\mathrm{u}}} \left\{ \mathrm{U}\bigg(\frac{\langle \mathbf{\Gamma}_{\mathrm{ED}}, \mathbf{\Gamma}_{\mathrm{sch}}^{(j)} \rangle}{||\mathbf{\Gamma}_{\mathrm{sch}}^{(j)}||_{\mathbf{1}}} - \xi_{\mathrm{jnt}} \bigg) \right\} \times \mathbf{\Gamma}_{\mathrm{sch}}^{(j)} , \tag{3.12}$$

where $\mathrm{U}(\mathbf{x})$ is the unit step function that applies to all the elements of a vector $\mathbf{x}$, $\langle \mathbf{x}, \mathbf{y} \rangle$ is the inner product of vectors $\mathbf{x}$ and $\mathbf{y}$, $||\mathbf{x}||_{\mathbf{1}}$ is the L1-norm of a vector $\mathbf{x}$, and $0 < \xi_{\mathrm{jnt}} < 1$ is a joint detection threshold. For example, if $\xi_{\mathrm{jnt}} = 0.5$, this means that at least half of the subcarriers from a scheduling vector need to be sensed as occupied through energy detection,

59

so that the mMS is identified as a nearby mMS. An empirically determined appropriate value for ξ_{jnt} is 0.75.

Spectrum sensing results are impaired with missed detections (MD) and false alarms (FA) due to additive noise. In the macrocell uplink, another reason for these impairments is the ICI that is caused by the timing misalignment. If the interference level of an mMS with an index-j is strong, it satisfies

$$\text{U}\big(\langle \mathbf{\Gamma}_{\text{ED}}, \mathbf{\Gamma}_{\text{sch}}^{(j)} \rangle / ||\mathbf{\Gamma}_{\text{sch}}^{(j)}||_{\mathbf{1}} - \xi_{\text{jnt}}\big) = 1, \tag{3.13}$$

which implies that if that mMS's delay is larger than the CP of a femtocell signal, it may also yield a strong ICI in some resource blocks leading to false alarms. Denote $\mathbf{\Pi}_{\text{int}}$ as the set of mMSs that satisfy the above equality. In order to detect if there are any resource blocks that are subject to strong ICI, the femtocell checks the neighboring resource blocks of mMSs that belong to the set $\mathbf{\Pi}_{\text{int}}$. Typically, ICI may impact only few resource blocks within the neighborhood of a certain subcarrier. Letting N_{ICI} denote the number of resource blocks where ICI may be considered as dominant, the set of resource blocks that will be checked for the presence of ICI is given by the following vector

$$\tilde{\mathbf{\Gamma}}_{\text{sch}}(N_{\text{ICI}}) = \sum_{j \in \mathbf{\Pi}_{\text{int}}} \left(\text{sign}\left[\sum_{k=-N_{\text{ICI}}}^{N_{\text{ICI}}} \mathcal{L}_{\text{shift}}\left(\mathbf{\Gamma}_{\text{sch}}^{(j)}, k \right) \right] - \mathbf{\Gamma}_{\text{sch}}^{(j)} \right), \tag{3.14}$$

where $\mathcal{L}_{\text{shift}}(\mathbf{x}, k)$ is a logical right-shift operator which shifts the elements of a bit-vector $\mathbf{x}$ in k bit positions towards right, and $\text{sign}(\mathbf{x})$ is a sign operator which operates individually on all the elements of a vector $\mathbf{x}$. Once the resource blocks that may be subject to ICI are obtained in vector $\tilde{\mathbf{\Gamma}}_{\text{sch}}(N_{\text{ICI}})$, they are compared with the energy detection threshold $\xi_{\text{thrs}}^{(\text{ED})}$ as follows

$$\mathbf{\Gamma}_{\text{ICI}} = \text{U}\left(\tilde{\mathbf{\Gamma}}_{\text{sch}}(N_{\text{ICI}}) \otimes |\mathbf{r}_{\text{rec}}|^2 - \xi_{\text{thrs}}^{(\text{ED})} \right), \tag{3.15}$$

where $\otimes$ is used to indicate a term-by-term product. Then, all the occupied resource blocks are captured by the sum $\mathbf{\Gamma}_{\text{ICI}} + \mathbf{\Gamma}_{\text{used}}$, whose complementary set yields the spectrum

60

opportunities. Note that if any information about the delays from the mMSs are available, such information can be utilized in obtaining the set $\mathbf{\Pi}_{\text{int}}$, where mMSs whose delays are within the CP-length are not included into the set since they do not cause significant ICI (they may still yield some ICI due to their multipath components).

As a simple example, consider the macrocell UL scenario illustrated in Fig. 3.7, where a resource block size of 12 subcarriers as in LTE is considered. The fBS compares the spectrum sensing results (shown in Fig. 3.7(c)) with the scheduling information (shown in Fig. 3.7(b)) to determine the resource blocks that constitute spectrum opportunities. Energy detection applied to the received signal (Fig. 3.7(a)) yields some FAs due to noise and due to ICI as shown in Fig. 3.7(c). These false alarms may or may not cause a resource block to be considered as occupied based on their number within each resource block. The spectrum opportunities found for the illustrated scenario are shown in Fig. 3.7(d), where scheduling information is plotted again for visual comparison. Note that the spectrum sensing results indicate that the received signal power for mMS2 is relatively weak because it is apparently a far-away mMS. This means that the resource blocks associated with mMS2 may be utilized by the femtocell both in the uplink and in the downlink.

3.5 Simulation Results

Computer simulations are performed to analyze the variation of ICI with respect to distance as well as to quantify the effect of ICI on the successful detection of empty parts of the spectrum.

The path loss model used in the simulations, which is derived from the Okumura-Hata model, is obtained from [52]. The model, which is applicable to small to medium cities, yields the path loss (in dB) as follows

$$L = 46.3 + 33.9 \log(f_{\text{c}}) - 13.82 \log(h_{\text{b}}) + \big(44.9 - 6.55 \log(h_{\text{b}})\big) \log(d) - F(h_{\text{M}}), \quad (3.16)$$

Table 3.1 Simulation parameters

Parameter	Value
Center frequency (f_c)	700 MHz, 2 GHz
Bandwidth (B)	5.714 MHz
FFT size	512
Symbol duration	89.9 μsec
CP sizes	1/32, 1/16, 1/8, 1/4
BS height (h_b)	30 m, 50 m
MS height (h_M)	2 m
MS transmit power	27 dBm
Antenna gain	16 dB
Wall penetration loss	15 dB
Number of Walls	1 (external)
Noise floor of fBS	-174 dBm/Hz + $10\log_{10}(B)$ = -106.43 dBm

where f_c is the center frequency, h_b is the base station height above ground, h_M is the mobile station height above ground, and $F(h_M)$ is given by

$$F(h_M) = \big(1.1\log(f_c) - 0.7\big)h_M - \big(1.56\log(f_c) - 0.8\big). \qquad (3.17)$$

Concerning the scenario at hand, h_b should be considered as the height of a femtocell BS, which is found in a high-rise building. The parameters related to wave propagation and path loss used in the simulations are mainly selected according to the values given in [3] and [52]. All simulation parameters are listed in Table 3.1.

In Fig. 3.8, the variation of the ICI power depending on the round-trip-delay (RTD) is plotted where the largest delay corresponds to a distance of 5 km. To obtain the simulated results, the resource blocks allocated to the mMS2 are randomly spread around the given spectrum, and ICI is measured by determining the total energy in the unused resource blocks. The theoretical curves, on the other hand, are plotted utilizing the expressions for ICI given in (3.8) to verify the simulation results. From the curves plotted, it can be concluded that

62

- ICI is typically close to zero for delays smaller than the CP size. Once the CP is exceeded, there is a sharp rise in the ICI, but at larger distances ICI decreases due to increased path loss.

- Under certain conditions, ICI power might be lower than the noise floor, i.e. the effect of ICI can become negligible.

To investigate how the ICI power is affected by the changes in certain important system parameters, the ICI versus delay analysis is performed for two different center frequencies and two BS heights (employing a CP size of 32 samples). The results demonstrated in show that employing a lower center frequency or having the BS at a higher location might considerably increase the received interference power.

Another analysis is performed on the error probability in detecting the occupied and unoccupied subcarriers in the received UL signal via energy detection. The error probability is computed as the sum of probability of missed detection (PMD) and probability of false
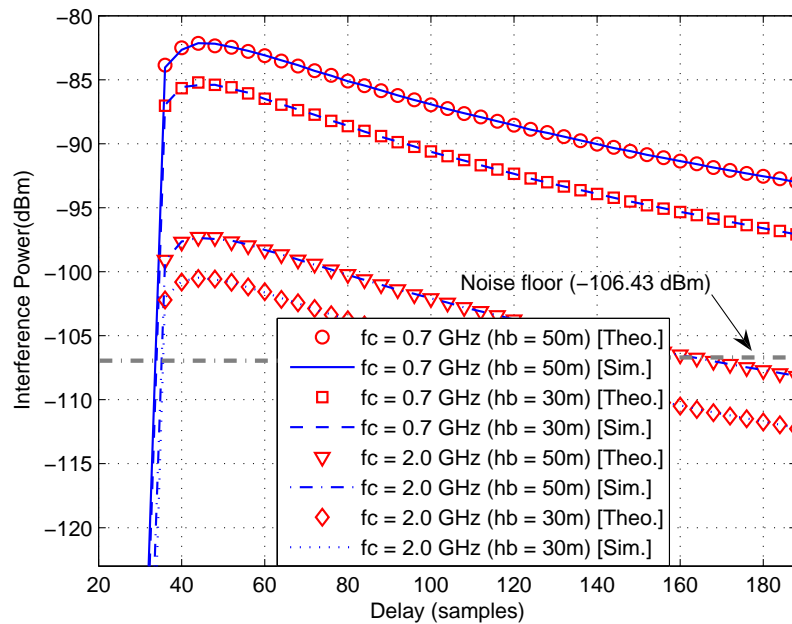
Figure 3.8 Variation of ICI power wrt. RTD for different center frequencies and femtocell BS heights.

alarm (PFA). PMD is defined as the ratio of number of subcarriers detected as unused although they are used to the total number of subcarriers N. PFA, on the other hand, is the ratio of the number of subcarriers detected as used although they are unused to N.

Two different subcarrier assignment schemes are considered. The first one is a blockwise assignment, where the two schemes used in the simulations are an LTE resource block with 12 subcarriers and 7 symbols, and a WiMAX UL PUSC tile with 4 subcarriers and 3 symbols. These schemes will be shortly denoted as 12×7 and 4×3, respectively. The other assignment scheme considered is a randomized assignment, where each individual subcarrier may be assigned to a different user. The two randomized assignment schemes employed in the simulations are 1×7 and 1×3. Although not used in any standard, these schemes are included in our simulations to investigate the effect of using small number of subcarriers as an assignment unit. The maximum RTD that the latest arriving user signal can have ($\tau_{\max}$) is considered to be between 0 μs and 60 μs, where all other user RTDs are between 0 μs and $\tau_{\max}$. Note that $\tau_{\max}$ values greater than 11.2 μs exceed the CP duration.
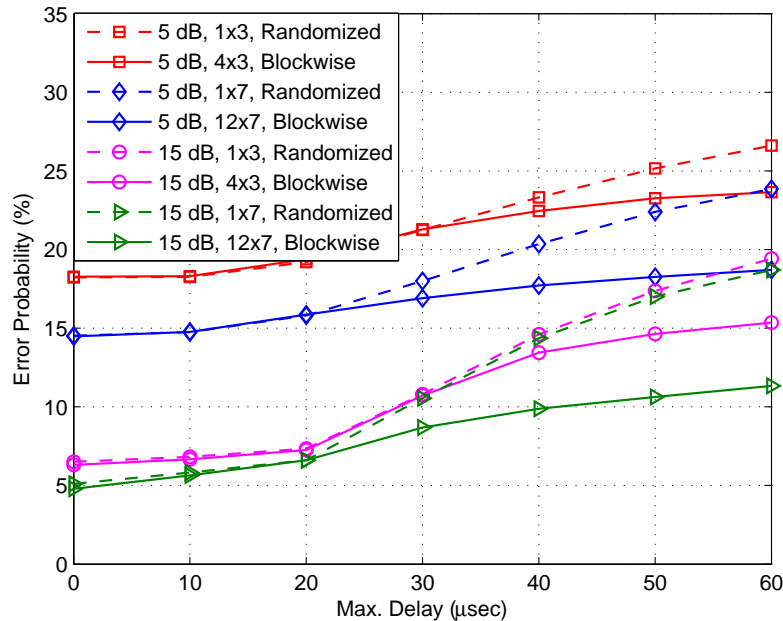
Figure 3.9 Error probability versus $\tau_{\max}$ for energy detection with blockwise and randomized assignments.

Fig. 3.9 demonstrates the related simulation results, where the signals of all 12 users are considered to have the same power. An optimum energy detection threshold is used in all cases (see [5] for a detailed analysis of obtaining the optimum threshold in different scenarios). It is observed that in randomized assignment, ICI has a more destructive effect on the detection performance. This is because in randomized assignment, each occupied subcarrier affects its adjacent subcarriers, some of which may be unoccupied. In the block-wise assignment, however, the subcarriers that are strongly affected are limited to the ones that are adjacent to each block. The two reasons for the error rates being higher for block size 4×3 compared to block size 12×7 are that number of subcarriers is smaller leading to a higher number of affected empty subcarriers, and number of symbols is smaller resulting in worse noise averaging.

3.6 Concluding Remarks

In this chapter, a framework for an OFDMA based co-channel femtocell implementation is provided for next-generation broadband wireless communication systems. Co-channel interference is avoided by determining the spectra of closely located users and not using their resource blocks both in the UL and DL. Moreover, the impact of ICI is taken into account, which occurs due to asynchronous arrivals of mMS signals to an fBS. In order to improve the spectrum sensing results, the scheduling information obtained from the mBS is utilized. The proposed framework may help in solving the interference problems observed in the CSG mode of operation in OFDMA based femtocell networks.

UPLINK USER SIGNAL SEPARATION FOR OFDMA-BASED COGNITIVE RADIOS

4.1 Introduction

Spectrum awareness is one of the fundamental features of cognitive radios (CR) [61]. It has conventionally been considered as a radio's being aware of the occupied and available frequency bands within its target spectrum [62]. It is achieved through spectrum sensing, where interference temperature is measured over the entire spectrum targeted, and the parts whose energy level exceeds a certain threshold are considered to be occupied [63, 64]. A different aspect was added to the spectrum awareness concept in [65] by attempting to characterize the source of the signal in the occupied spectrum. In this work, we propose to enhance the spectrum awareness by providing the cognitive radios with the capability of separating the primary user signals from each other in the uplink (UL). We consider orthogonal frequency division multiple access (OFDMA) based CR systems that co-exist with a primary network that is also OFDMA based[1].

Due to the involvement of multiple user signals, the uplink of OFDMA systems poses a number of challenges that do not exist in the downlink (DL). Most of these problems including multiuser channel estimation [66], carrier frequency offset (CFO) estimation [67], synchronization and symbol timing estimation [36, 68], multiuser interference cancellation [69], and subcarrier and power allocation [70] are investigated extensively in the prior-art. However, the problem of separating UL user signals without access to the subcarrier assignment scheme (SAS) has not been investigated in detail in the literature.

---

[1]The proposed algorithm can be applicable to single carrier-frequency disivion multiple accessing (SC-FDMA) based UL systems, as well, given that the resource blocks employed enable estimation of user specific parameters.

A practical cognitive radio application where user separation might be quite useful is a co-channel femtocell network coexisting with a macrocell network [29, 31], both of which have an OFDMA based physical layer. If the coexistence is based on a shared spectrum approach where the femtocell utilizes the available parts of the macrocell spectrum in an opportunistic manner, user separation can be very beneficial to the femtocell. How the user separation and block size estimation algorithms proposed in this chapter might improve the spectrum opportunity detection for femtocells is explained in Section 4.6. Other possible applications regarding femtocell-macrocell coexistence are discussed in detail in [8].

User separation in UL-OFDMA was considered in [71] for interleaved OFDMA systems. In [71], subcarriers allocated to different users follow a certain periodic structure, which leads to a user specific CFO. Hence, by estimating the CFOs, different user signals are identified and separated. In this chapter, however, we propose a semi-blind user separation algorithm that can be applied to any SAS, which does not necessarily involve any periodicity. The user separation algorithm considered in this chapter is based on exploiting the differences in user CFOs and delays. In the uplink of an OFDMA system, CFOs of users vary due to the differences in oscillator frequencies as well as the Doppler shifts caused by the different velocities of users. User delays, on the other hand, vary due to the different distances of users to the UL receiver.

In this chapter, we assume time synchronization to the first arriving UL user signal as well as availability of information on the basic OFDMA system parameters such as FFT size, sampling time, and cyclic prefix (CP) duration. Considering scenarios where information about block dimensions is not available, a block size estimation algorithm is devised that exploits the correlation between the pilot subcarriers within the same block. A Gaussian approximation based approach is then introduced that tries to determine the potential performance of the block size estimation algorithm theoretically.

The second algorithm proposed aims at user separation. It estimates the CFOs and delays for each block separately by performing cross-correlations over pilot subcarriers, and groups the blocks in the UL symbol according to their CFOs and delays using the

67

$Y(m,k)$ → Calculate vertical autocorrelation as in (4) → $|\mathcal{R}^{(V)}(l)|$ → Obtain the index of the second strongest correlation → K → Return resource block dimensions as $(K+1)x(M+1)$ → $(K+1)x(M+1)$

$Y(m,k)$ → Calculate horizontal autocorrelation as in (5) → $|\mathcal{R}^{(H)}(l)|$ → Obtain the index of the second strongest correlation → M

(b)

Calculate CFO and Delay for Each Block ← Find Blocks Exceeding the Power Threshold ← Received OFDMA Signal

Normalize CFO and Delay Values → Find Cluster Centers (Number of Users) via Subtractive Clustering → Return Number of Users

Normalize CFO and Delay Values → Cluster Blocks Based on CFO and Delay Values via Iterative Partitioning → Return Subcarrier Map of Each User

Figure 4.1 (a) Flowchart for block size estimation. (b) Flowchart for user signal separation.

subtractive clustering and iterative partitioning techniques. This way, it is able to determine the number of UL users and to separate their subcarriers. Flowcharts for both the block size estimation and user separation techniques are illustrated in Fig. 4.1a and Fig. 4.1b, respectively, which will be discussed in more detail in the later sections. Flowcharts for both the block size estimation and user separation techniques are illustrated in Fig. 4.1a and Fig. 4.1b, respectively, which will be discussed in more detail in the later sections.

The organization of the chapter is as follows. Section 4.2 provides the UL-OFDMA system model. In Section 4.3, the block size estimation method is presented and a Gaussian approximation approach to block size estimation is given. In Section 4.4, a mathematical model of the proposed user separation algorithm is provided. In Section 4.6, the potential contribution of block size estimation and user separation algorithms to spectrum opportu-

nity detection of cognitive radios is explained. Simulation results are presented in Section 4.7, and Section 4.8 concludes the chapter.

4.2 UL-OFDMA System Model

Consider an OFDMA system with N_u users in the uplink. The sampled time domain signal at the transmitter of user i can be written as

$$x^{(i)}(n) = \sqrt{E_{\mathrm{tx},i}} \sum_{k \in \mathbf{\Gamma}_i} X^{(i)}(k) e^{j2\pi kn/N}, -N_{\mathrm{CP}} \leq n \leq N-1, \tag{4.1}$$

where $E_{\mathrm{tx},i}$ is the total transmitted energy per symbol for user i, N is the FFT size, $\mathbf{\Gamma}_i$ is the set of subcarriers with N_i elements assigned to user i out of $\mathcal{S}$ used subcarriers, $k \in \mathbf{\Gamma}_i$ is the subcarrier index, N_{CP} is the length of the cyclic prefix, and $X^{(i)}(k)$ is the data on the kth subcarrier of ith user.

A received symbol of user i after the FFT operation can be written as

$$R^{(i)}(k) = X^{(i)}(k) \; H^{(i)}(k) e^{-j2\pi k\tau_i/N} e^{j\pi\xi_i} \mathrm{sinc}(\pi\xi_i) \; e^{j\pi k\delta_i} \mathrm{sinc}(\pi k\delta_i) e^{j\Phi_i} + I^{(i)}(k) + W(k), \tag{4.2}$$

where ξ_i is the carrier frequency offset (normalized by the subcarrier spacing f_s/N, where f_s is the sampling frequency), δ_i is the sampling clock error, τ_i is the timing offset of user i, Φ_i is the random phase noise caused by the instability of user i's oscillator, $H^{(i)}(k)$ is the frequency selective channel of user i, $I^{(i)}(k)$ is the inter-carrier interference (ICI) of user i, and $W(k)$ is complex additive white Gaussian noise (AWGN). In the remainder of this chapter, it will be assumed that the random phase noise as well as the sampling clock error in (4.2) are negligible.

From (4.2), it is seen that the CFO has two effects on the received signal. First, it results in amplitude degradation and a constant phase shift, and second, in ICI. Another effect, which becomes apparent when the phases of identical pilot subcarriers in two adjacent symbols are compared [72], is a phase shift that changes linearly over symbols. Taking this

69

linear phase shift into account, the received signal over multiple symbols can be modeled as

$$
\begin{aligned}
Y^{(i)}(m,k) &= R^{(i)}(m,k)e^{j2\pi m\xi_i\left(1+\frac{N_{\mathrm{CP}}}{N}\right)} + W(m,k) \\
&= \left[X^{(i)}(m,k)H^{(i)}(m,k)e^{j\pi\xi_i}\mathrm{sinc}(\pi\xi_i)\,e^{-j2\pi k\tau_i/N} + I^{(i)}(m,k)\right]e^{j2\pi m\xi_i\left(1+\frac{N_{\mathrm{CP}}}{N}\right)} \\
&\quad + W(m,k)\,,
\end{aligned}
\tag{4.3}
$$

where m is the symbol index.

4.3 Block Size Estimation

Uplink OFDMA signal is composed of independent frequency allocation blocks ($\mathcal{B}$'s) such as bins or tiles (tile structure in WiMAX UL-PUSC is depicted in Fig. 4.2). A certain user may use a number of these (not necessarily adjacent) blocks in the UL, depending on its data rate requirements and scheduling information.

If the coexistence of the primary network and the cognitive radio is cooperative (which might be the case, e.g., in a cognitive femtocell deployment where both the macrocell and femtocells are operated by the same service provider), then the primary network might provide information about its fundamental parameters such as N, N_{CP}, and f_s to the cognitive radio. Although the CR might get informed about the dimensions of $\mathcal{B}$, as well, it is possible that the CR has to determine the block size blindly.

It is feasible to determine the block size of an UL-OFDMA system in a blind manner utilizing any received signal $Y(m,k)$ that contains an arbitrary number of symbols, given that the two following assumptions are valid

- The pilot subcarriers are at the corners of the resource blocks, e.g., as in the PUSC mode of WiMAX standard[2].

- In the transmitter, the (BPSK modulated) pilot subcarriers within the same resource block are assigned the same value.

---

[2]Extensions to other pilot structures may also be possible after certain modifications.

70
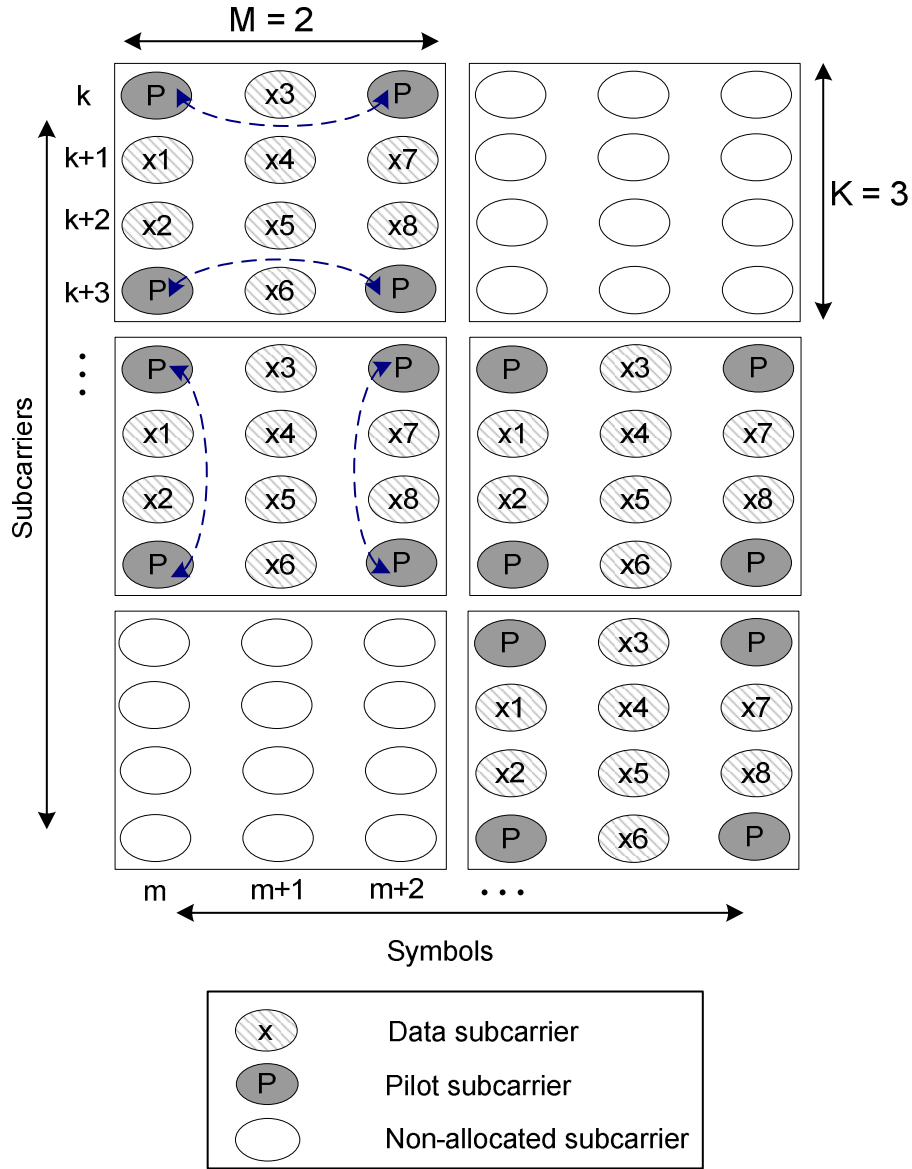
Figure 4.2 6 blocks in a WiMAX UL-PUSC system, where each block is a 4x3 tile, i.e., K=3 and M=2. Correlations for obtaining $\hat{\xi}$ are illustrated in the first block, while the correlations for obtaining $\hat{\tau}$ are illustrated in the second block.

Although the second condition causes some slight increase in the peak-to-average power ratio (PAPR) of the UL signal, this increase is tolerable especially in a cooperative coexistence scenario, where the primary network is willing to facilitate cognitive communications.

The pilots in each $\mathcal{B}$ are correlated with each other, whereas the data subcarriers are uncorrelated. Also, there is not a considerable correlation between the pilots in different $\mathcal{B}$s

71

since each $\mathcal{B}$ is assigned a random BPSK value for its pilots. The dimensions of $\mathcal{B}$ can be determined by exploiting the correlation between the pilots within the $\mathcal{B}$s.

The vertical dimension of $\mathcal{B}$ can be found by performing autocorrelation over an entire symbol (vertical correlation)[3]. Without taking the effects of delays and CFOs into consideration, we define the absolute value of the vertical correlation as

$$\left|\mathcal{R}^{(V)}(l)\right| = \left|E\{Y^*(m,k)Y(m,k+l)\}\right| = \begin{cases} \sigma_s^2 + \sigma_n^2 & l = 0 \\ \frac{1}{K+1}\sigma_s^2 & l = K \\ 0 & \text{otherwise} \end{cases} \qquad (4.4)$$

where l is the lag index, $E\{\cdot\}$ denotes the expectation operation, K is the separation between the pilots in the same symbol of $\mathcal{B}$, σ_s^2 is the average subcarrier power, and σ_n^2 is the noise power. Note that the expectation is performed over all subcarriers, and the $\frac{1}{K+1}$ term is the ratio of the number of pilot pairs in a symbol (number of $\mathcal{B}$s) to the number of occupied subcarriers $\mathcal{S}$.

In a similar manner, the horizontal dimension of $\mathcal{B}$ can be obtained via an autocorrelation over rows (horizontal correlation), where a row is the set of subcarriers at the same subcarrier index k. The absolute value of the horizontal correlation is given by

$$\left|\mathcal{R}^{(H)}(l)\right| = \left|E\{Y^*(m,k)Y(m+l,k)\}\right| = \begin{cases} \sigma_s^2 + \sigma_n^2 & l = 0 \\ \frac{1}{M+1}\sigma_s^2 & l = M \\ 0 & \text{otherwise} \end{cases} \qquad (4.5)$$

where M is the separation between the pilots in the same row of $\mathcal{B}$. The expectation is performed over all symbols involved in the correlation, and the $\frac{1}{M+1}$ term is the ratio of the number of pilot pairs (number of $\mathcal{B}$s) to the number of non-empty subcarriers in a row.

In both vertical and horizontal correlations, the desired peak is the one that is strongest after the peak at the origin. In order to accentuate the desired peak, noise averaging is performed by averaging $\boldsymbol{\mathcal{R}}^{(V)}$ over all symbols available, and by averaging $\boldsymbol{\mathcal{R}}^{(H)}$ over

---

[3]It is assumed that the orientation of subcarriers versus symbols is as depicted in Fig. 4.2
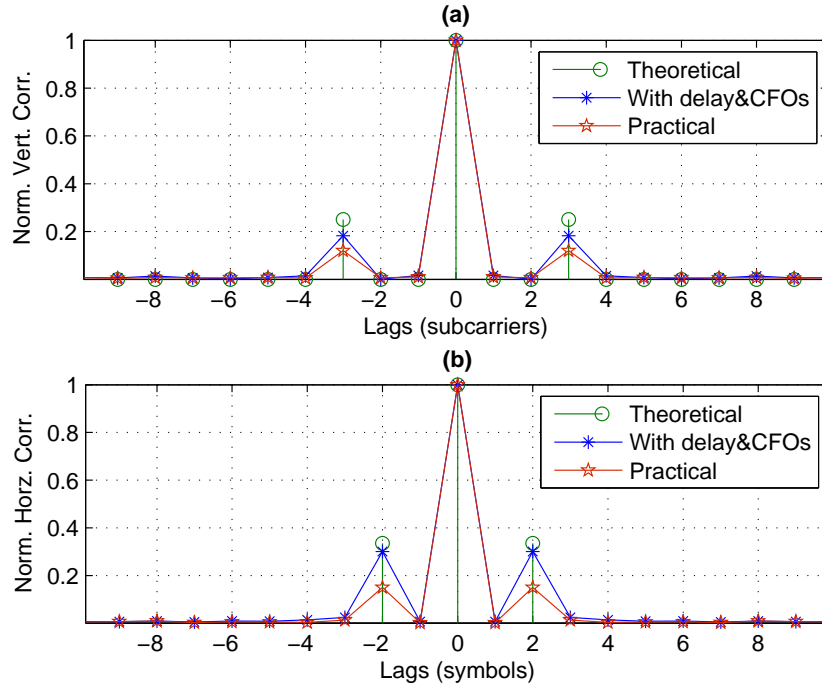
Figure 4.3 Normalized autocorrelations obtained utilizing a 60 symbol long signal (with FFT size 512) for a block size of 4x3 at 30 dB SNR in an AWGN channel. (a) Vertical autocorrelation. (b) Horizontal autocorrelation.

N rows. The desired peak in the vertical correlation is expected to appear at the Kth lag yielding the vertical dimension of $\mathcal{B}$ as $K+1$. Similarly, the horizontal dimension is obtained from the horizontal correlation as $M+1$.

An illustrative example of the vertical and horizontal correlations is provided in Fig. 4.3, where the main peaks are normalized to 1. The block dimensions that need to be determined is 4 subcarriers by 3 symbols (4×3) as in Fig. 4.2. Hence, peaks are observed in the 3rd lag in the vertical correlation and in the 2nd lag in the horizontal correlation. In Fig. 4.3a and Fig. 4.3b, the theoretical curves represent the values provided by (4.4) and (4.5), where the delays and CFOs are not taken into account. Under the effect of delays and CFOs, the second curves are obtained, where the desired peaks appear weaker than the theoretical values. The reason for the weakening of the desired peaks is that the delays and CFOs introduce different correlations to the subcarriers of each user, which, in effect, deteriorates

73

the overall correlations of the pilots. Finally, the correlation values that are obtained in a practical simulation are plotted, where the desired peaks are considerably weaker. This is because in a practical scenario, the vertical correlations are averaged over all symbols, only $\frac{2}{M+1}$ of which contain pilot subcarriers; and the horizontal correlations are averaged over all rows, $\frac{2}{K+1}$ of which contain pilots. Therefore, the heights of the desired peaks for the practical case are $\frac{1}{K+1} \times \frac{2}{M+1}$ and $\frac{1}{M+1} \times \frac{2}{K+1}$ for the vertical and horizontal correlations, respectively, which are equal to each other.

4.3.1 Gaussian Approximation for Block Size Estimation

In both vertical and horizontal correlations performed for block size estimation, each of the samples in the output of the correlation can be approximated using Gaussian approximation (GA). Ignoring the sample at the zeroth lag, all of the correlation samples have a zero mean except the sample at the desired peak location. Therefore, the problem of detecting a peak at the correlator output can actually be considered as finding a variable with a non-zero mean within a group of zero-mean variables.

Let μ_l and σ_l denote the mean and the standard deviation of a correlation value $\mathcal{R}(l)$ at the l-th lag, respectively. If l_p denotes the lag corresponding to the peak of the correlation outputs, we have $\mu_{l_\mathrm{p}} > 0$, and μ_l is equal to zero otherwise. Taking into account that the peak detection is performed after absolute value operation, the probability density function of $\big|\mathcal{R}(l_\mathrm{p})\big|$ can be written as

$$\mathrm{P}\Big(\big|\mathcal{R}(l_\mathrm{p})\big|\Big) = \frac{1}{\sigma_{l_\mathrm{p}}\sqrt{2\pi}}\left(\exp\left(-\frac{\left(\big|\mathcal{R}(l_\mathrm{p})\big| - \mu_{l_\mathrm{p}}\right)^2}{2\sigma_{l_\mathrm{p}}^2}\right) + \exp\left(-\frac{\left(\big|\mathcal{R}(l_\mathrm{p})\big| + \mu_{l_\mathrm{p}}\right)^2}{2\sigma_{l_\mathrm{p}}^2}\right)\right) . \quad (4.6)$$

In order for $\big|\mathcal{R}(l_\mathrm{p})\big|$ to have the largest amplitude, all other samples at the other correlation lags need to have absolute values that are smaller than $\big|\mathcal{R}(l_\mathrm{p})\big|$. This has a probability of $\left[1 - 2Q\left(\frac{\big|\mathcal{R}(l_\mathrm{p})\big|}{\sigma_l}\right)\right]^{C-1}$, where C is the half-length of the correlator output excluding the sample at the zeroth lag. Therefore, the total probability of detection of peak of the

74

correlation output can be obtained by the following equation

$$P_{\mathrm{d}} \approx \int_{x=0}^{\infty} \frac{1}{\sigma_{l_{\mathrm{p}}}\sqrt{2\pi}} \left\{ \exp\left(- \frac{\left(\left|\mathcal{R}(l_{\mathrm{p}})\right| - \mu_{l_{\mathrm{p}}}\right)^2}{2\sigma_{l_{\mathrm{p}}}^2} \right) + \exp\left(- \frac{\left(\left|\mathcal{R}(l_{\mathrm{p}})\right| + \mu_{l_{\mathrm{p}}}\right)^2}{2\sigma_{l_{\mathrm{p}}}^2} \right) \right\}$$
$$\times \left[1 - 2Q\left(\frac{\left|\mathcal{R}(l_{\mathrm{p}})\right|}{\sigma_l} \right) \right]^{C-1} \mathrm{d}\left|\mathcal{R}(l_{\mathrm{p}})\right| . \tag{4.7}$$

Performing (4.7) for both horizontal and vertical correlations yields the probabilities of detecting the corresponding peaks. Denoting these two probabilities as P_V and P_H, the probability of detecting the block size correctly is simply equal to $P_V \times P_H$.

Note that (4.7) is an approximation due to two primary reasons. First, as discussed before, noise-cross-noise terms in the pilot correlations are approximated using a GA. Secondly, all of the correlation samples are assumed to be uncorrelated random variables, which is not true in practice. The existence of delays introduces correlation between subcarriers in the same symbol, and the CFOs result in correlation between subcarriers in adjacent symbols. Despite these factors, it will be shown in Section 4.7 that the approximation yields relatively close results to the simulation results, especially when the block size is estimated over large number of symbols.

4.4   User Separation Method

The proposed user separation method is based on exploiting the differences in the τ_i's and ξ_i's of different UL-OFDMA users. The first step of the method is to determine the occupied $\mathcal{B}$'s via energy detection. Then, for each occupied $\mathcal{B}$, the UL receiver performs τ and ξ estimation. Next, occupied $\mathcal{B}$'s are clustered according to their τ and ξ values, where each separate cluster yields the $\mathcal{B}$'s that belong to a certain user. This way, $\hat{\mathbf{\Gamma}}_i$, which is an estimate for $\mathbf{\Gamma}_i$, is obtained for each user i.

The total energy of each block $\mathcal{B}$ can be calculated as follows

$$\Psi(\mathcal{B}) = \sum_{(m,k)\in\mathcal{B}} \left| Y(m,k) \right|^2 . \tag{4.8}$$

This energy value is averaged over the subcarriers within the block and inputted to an energy detector that employs a threshold ζ

$$\frac{\Psi(\mathcal{B})}{(K+1)(M+1)} \underset{H_0}{\overset{H_1}{\gtrless}} \zeta \, , \tag{4.9}$$

where hypothesis H_1 implies that block $\mathcal{B}$ is occupied, and hypothesis H_0 implies that it is not. Details of energy detection in OFDMA-UL, such as optimizing ζ can be found in [5]. Let $\boldsymbol{\beta}$ denote the set of all the occupied $\mathcal{B}$'s that satisfy the hypothesis H_1 in (4.9). Then, for each $\mathcal{B}$ within $\boldsymbol{\beta}$, carrier frequency offset and delay estimations are performed.

Regarding the CFO estimation, an important observation from (4.3) is that the linear phase shift caused by the CFO affects both the desired signal and ICI the same way. Therefore, a reliable ξ estimate can be obtained by correlating two identical pilot symbols [72], or pilot subcarriers in different symbols as illustrated in Fig. 4.2. If $\boldsymbol{\mu}_j$ denotes the indices of symbols (within the jth block) that carry pilot subcarriers, and $\boldsymbol{\Pi}_{m,j}$ denotes the subcarrier indices of pilots in symbol m within $\mathcal{B}$, a ξ estimate for $\mathcal{B}$, which will be denoted as $\hat{\xi}_j$, can be obtained by performing pairwise correlation between $\boldsymbol{\Pi}_{m,j}$ in different symbols within $\mathcal{B}$, separated by M symbols. Ignoring the ICI and noise terms, this correlation would be as follows

$$
\begin{aligned}
r_j^{(\xi)}(M) &= \sum_{m,k} Y^*(m,k)Y(m+M,k), \qquad m \in \boldsymbol{\mu}_j, \ k \in \boldsymbol{\Pi}_{m,j}, \\
&= e^{j2\pi\xi M\left(1+\frac{N_{\mathrm{CP}}}{N}\right)} \sum_{m,k} |X(m,k)|^2 H^*(m,k)H(m+M,k)\mathrm{sinc}^2(\pi\xi), \tag{4.10}
\end{aligned}
$$

where symbol $m + M$ is within $\mathcal{B}$. $\hat{\xi}_j$ can then be obtained as

$$\hat{\xi}_j = \frac{\angle\big(r_j^{(\xi)}(M)\big)}{2\pi M\big(1 + \frac{N_{\mathrm{CP}}}{N}\big)} \, , \tag{4.11}$$

where

$$\angle\big(r_j^{(\xi)}(M)\big) = \tan^{-1}\big(\mathrm{Im}\big[r_j^{(\xi)}(M)\big]/\mathrm{Re}\big[r_j^{(\xi)}(M)\big]\big). \tag{4.12}$$

76

Table 4.1 Typical Doppler spreads and coherence times for WiMAX

Carrier Freq.	Speed	Max. Doppler	Coherence Time
2.5 GHz	2 km/h	4.6 Hz	200 ms
2.5 GHz	45 km/h	104.2 Hz	10 ms
2.5 GHz	100 km/h	231.5 Hz	4 ms
5.8 GHz	2 km/h	10.7 Hz	93 ms
5.8 GHz	45 km/h	241.7 Hz	4 ms
5.8 GHz	100 km/h	537 Hz	2 ms

The timing offset causes a phase shift that changes linearly over the subcarriers, but is independent from the symbol index. If $\boldsymbol{p}_{k,j}$ denotes indices of rows with pilots within $\mathcal{B}$, a τ estimate for $\mathcal{B}$, which will be denoted as $\hat{\tau}_j$, can be obtained by correlating pilots at different rows separated by K subcarriers (illustrated in Fig. 4.2) as

$$
\begin{aligned}
r_j^{(\tau)}(K) &= \sum_{m,k} Y^*(m,k)Y(m,k+K), \qquad m \in \boldsymbol{\mu}_j, \ k \in \boldsymbol{p}_{k,j}, \\
&= e^{-j2\pi\tau K/N} \sum_{m,k} |X(m,k)|^2 H^*(m,k)H(m,k+K)\text{sinc}^2(\pi\xi),
\end{aligned}
\tag{4.13}
$$

where subcarrier $k + K$ is within $\mathcal{B}$. The τ estimate for $\mathcal{B}$ is obtained as follows

$$
\hat{\tau}_j = \frac{\angle\big(r_j^{(\tau)}(K)\big)}{-2\pi K/N} \ ,
\tag{4.14}
$$

where

$$
\angle\big(r_j^{(\tau)}(K)\big) = \tan^{-1}\big(\text{Im}\big[r_j^{(\tau)}(K)\big]/\text{Re}\big[r_j^{(\tau)}(K)\big]\big).
\tag{4.15}
$$

As seen from (4.10), an important condition necessary for $\hat{\xi}_j$ to be reliable is that the channel can be considered constant during M symbols. Taking the WiMAX standard as a reference, Table-4.1 [73] provides information about channel coherence times for two different frequency bands. Given that the WiMAX symbol duration is around 0.1 ms, the channel coherence time covers up to 20 symbols even at a speed of 100 km/h in the 5.8 GHz band. Similarly, for any typical OFDMA based standard, it can be expected that this channel constancy condition is met.

77

Equation (4.13) also introduces a similar requirement in the frequency dimension. A reliable $\hat{\tau}_j$ can only be obtained if $H_m(k)$ for pilots separated by K subcarriers are highly correlated. Although this condition is met for any K in a single tap channel, in a frequency selective channel, K is typically taken a small number (e.g., in the WiMAX UL-PUSC system K is defined as 3).

Once $\hat{\xi}_j$'s and $\hat{\tau}_j$'s are obtained for all elements of $\boldsymbol{\beta}$, the user separation algorithm requires that $\mathcal{B}$'s are clustered according to their $\hat{\xi}_j$'s and $\hat{\tau}_j$'s, taking both values into account simultaneously. Each separate cluster generated by the clustering algorithm corresponds to a different user i and yields its subcarrier allocation vector estimate $\hat{\boldsymbol{\Gamma}}_i$.

The clustering method first yields an estimate for the number of users $(\hat{N}_{\mathrm{u}})$, which is determined by finding the cluster centers through the subtractive clustering algorithm outlined in [74, 75]. A critical input required by the subtractive clustering algorithm is the ratio of dimensions of the potential clusters, which will be denoted as $D_{\tilde{\xi}}$ and $D_{\tilde{\tau}}$. In the next step, utilizing $\hat{N}_{\mathrm{u}}$, the separation is performed via iterative partitioning algorithm discussed in [76, 77]. Iterative partitioning splits the input data into $\hat{N}_{\mathrm{u}}$ initial clusters. Then, for each cluster, it computes the sum of absolute distances from each point in the cluster to the cluster centroid, where the centroid is the component-wise median of the points in the cluster. By minimizing the total of these sums in an iterative manner, the clusters are determined.

Prior to applying the clustering method, the sets of $\hat{\xi}_j$'s and $\hat{\tau}_j$'s, which will be denoted as $\hat{\boldsymbol{\xi}}$ and $\hat{\boldsymbol{\tau}}$, respectively, need to be normalized. The normalization is mandated by the fact that the range of numerical values for $\hat{\boldsymbol{\tau}}$ is wider than the range of $\hat{\boldsymbol{\xi}}$s by at least two orders of magnitude. In fact, clustering without normalization results in a user separation that is solely based on $\hat{\boldsymbol{\tau}}$ values[4]. In particular, we apply the following normalizations:

$$\tilde{\boldsymbol{\xi}} = \frac{\hat{\boldsymbol{\xi}} - \min(\hat{\boldsymbol{\xi}})}{\max(\hat{\boldsymbol{\xi}}) - \min(\hat{\boldsymbol{\xi}})} , \tag{4.16}$$

---

[4]Computer simulations without applying any normalization resulted in poor user separation performances.

78
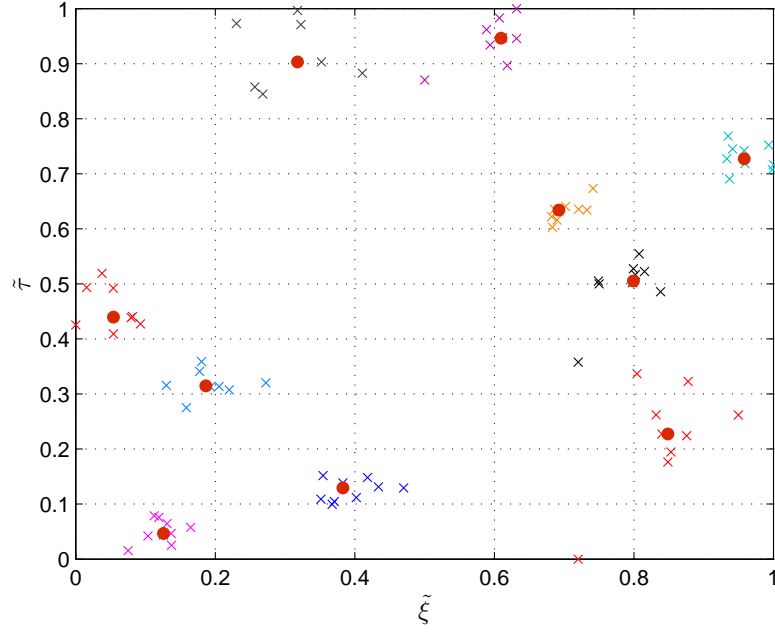
Figure 4.4 Clusters on the $\tilde{\tau}$ vs. $\tilde{\xi}$ plane in a 10-user scenario (30 dB SNR is assumed for all user signals over MP channel).

and

$$\tilde{\boldsymbol{\tau}} = \frac{\hat{\boldsymbol{\tau}} - \min(\hat{\boldsymbol{\tau}})}{\max(\hat{\boldsymbol{\tau}}) - \min(\hat{\boldsymbol{\tau}})} \ , \tag{4.17}$$

respectively, which map both $\hat{\boldsymbol{\xi}}$ and $\hat{\boldsymbol{\tau}}$ into the interval $[0, 1]$. Therefore, as shown in Fig. 4.4, the clustering is performed on a $[0, 1] \times [0, 1]$ plane.

A second point related to the subtractive clustering algorithm is that it requires to optimize the ratio of cluster dimensions for the best performance. This ratio $(D_{\tilde{\xi}}/D_{\tilde{\tau}})$ is proportional to the ratio of variances of $\tilde{\xi}_j$ and $\tilde{\tau}_j$, i.e., $(\sigma^2_{\tilde{\xi}_j}/\sigma^2_{\tilde{\tau}_j})$, which are related to each other as follows

$$\sigma^2_{\tilde{\xi}_j} = \frac{\mathrm{Var}(\mathcal{A}^{(\tau)})}{\mathrm{Var}(\mathcal{A}^{(\xi)})} \, \sigma^2_{\tilde{\tau}_j}, \tag{4.18}$$

where $\mathcal{A}^{(\tau)}$ and $\mathcal{A}^{(\xi)}$ denote the sets of all $\angle(r_j^{(\tau)}(K))$'s and $\angle(r_j^{(\xi)}(M))$'s, respectively. The $D_{\tilde{\xi}}/D_{\tilde{\tau}}$ input of the subtractive clustering algorithm is set as $\sqrt{\mathrm{Var}(\mathcal{A}^{(\tau)})/\mathrm{Var}(\mathcal{A}^{(\xi)})}$. From (4.18), it is seen that the wider is the range of values that $\angle(r_j^{(\tau)}(K))$ can take, the smaller

79

is the $D_{\tilde{\tau}}$ dimension of the clusters (the same analogy applies $D_{\tilde{\xi}}$ dimension, as well). More-over, (4.18) also indicates that $\sigma_{\tilde{\xi}_j}^2 / \sigma_{\tilde{\tau}_j}^2$ can be found before performing clustering by simply calculating the ratio of $\text{Var}(\mathcal{A}^{(\tau)})$ to $\text{Var}(\mathcal{A}^{(\xi)})$. An important assumption regarding (4.18) is that the ξ and τ values of different users are uniformly spread within $[\min(\xi), \max(\xi)]$ and $[\min(\tau), \max(\tau)]$, respectively.

A visual example that illustrates the clustering algorithm is provided in Fig. 4.4. It shows the clusters in a 10-user scenario, where SNR is assumed to be 30 dB for all user signals, and a multipath (MP) channel is considered along with the delay and CFO values in Table 4.2. In Fig. 4.4, the large red dots constitute the cluster centers found through subtractive clustering, and the markers surrounding each of them indicate the resource blocks that belong to a certain user determined through iterative partitioning.

4.5 User Separation Applications for OFDMA-Based Cognitive Radios

OFDMA-based cognitive femtocells are systems where user separation can be useful in various ways. This section provides examples of practical applications related to femtocell-macrocell coexistence that can be realized when OFDMA based femtocells are equipped with the capability of separating the macrocell mobile station (mMS) signals in the uplink.

4.5.1 Classifying the Source of Co-channel Interference

The spectral occupancy that the femtocell base station (fBS) observes in the received uplink signal might be caused by mMSs or by other femtocells (fBSs or femtocell mobile stations (fMS)). Information about the source of this co-channel interference (CCI) can be beneficial to the fBS because if the occupant is another femtocell, it can negotiate sharing the occupied spectrum with that femtocell.

The CFO, delay, and power measurements performed for user separation can be utilized for classifying the source of CCI. Assuming that the mMSs will possibly have a high mobility, while the locations of fBSs are fixed and the mobility of fMSs are limited, if the CCI is caused by an mMS, the CFO, power, and delay values measured will be varying over time, whereas

80

they will be fairly constant for an fBS, and displaying limited variations over time for an fMS. Hence, based on these three criteria, the fBS should be able to decide whether the source of CCI is an mMS or a femtocell.

To be able to track the changes in power and delay of a certain mMS, it is required to perform the corresponding measurements over multiple consecutive frames, where a frame is a certain number of adjacent symbols, for the same mMS. That means that the fBS needs to keep track of the subcarriers assigned to the same mMS over multiple frames. This can be achieved by building a chain of the clusters with close delay, power, and CFO values in adjacent frames, assuming that the delay, power, and CFO of an mMS cannot change sharply from one frame to another.

4.5.2 Hand-off Between Macrocell-BS and Femtocell-BS

In a co-channel femtocell implementation, the subcarrier assignment map of the macrocell may have been provided to the fBS. Even in this case, CFO, delay and power measurements can be used to find the direction of movement of an mMS, e.g., it can be concluded that an mMS is moving away from the fBS when its delay is increasing, and its power level is decreasing.

Information about the direction of movement of mMSs can make the hand-off decisions between fBS and mBS more robust. Hand-off decisions solely based on power measurements can be misleading in case of strong fading, i.e., an instant fading in the signal power can trigger an unnecessary hand-off. However, if the decrease in power is supported by an increasing delay measurement, then the hand-off decision would be much more reliable.

Via user separation based on tracking the delays and carrier frequency offsets of macrocell users, the users that are just passing by from the vicinity of the femtocell can be determined so that unnecessary hand-offs between the macrocell and femtocell are avoided.

In a case where a macrocell user needs to be handed over from a macrocell and multiple femtocells are available, the most appropriate femtocell for hand-off can be determined by these femtocells by sharing the user separation data they have.
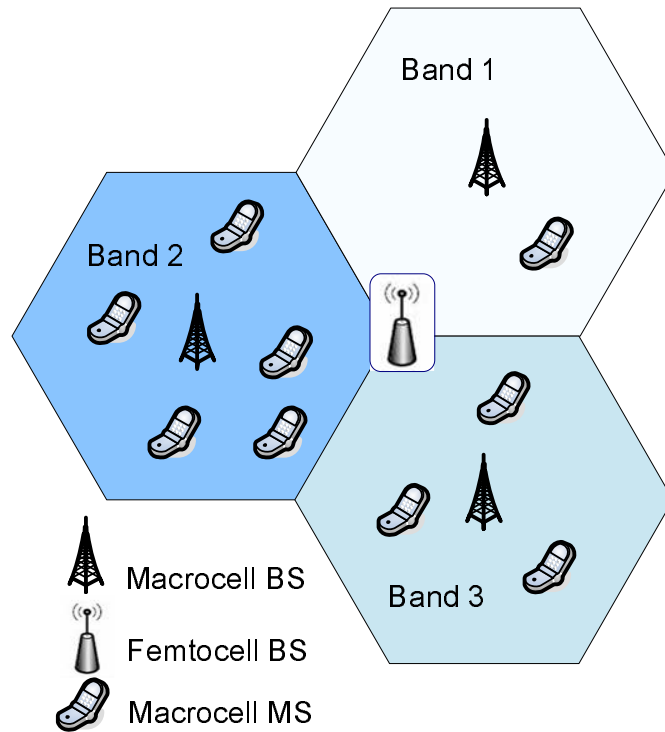
Figure 4.5 Femtocell operating in the middle of 3 mBSs in a system with frequency reuse of 3.

4.5.3 Directing Some Femtocell Users to the Macrocell

Information about the number of macrocell users might be useful in a macrocell-femtocell coexistence, where hand-offs can be performed conveniently between the macrocell and femtocell. In case of excessive demand for femtocell communications, i.e. when there are too many users connected to an fBS, it might be necessary to limit the number of femtocell users in order to relax the computational burden on the fBS. In such a scenario, the fBS can sense the macrocell uplink signal and determine the number of mMSs by applying user separation. If it finds that there are too few active mMSs, it can direct some femtocell users to the macrocell.

Note that an fBS may also reschedule its own users to a different frequency band, if an mMS using a frequency band reused by the fBS moves closer to the fBS.

4.5.4 Causing CCI to the Minimum Number of mMSs Possible

In a macrocell system with reuse factor not equal to 1, adjacent cells will be using separate frequency bands. In a cellular system where reuse factor is equal to 3, a femtocell that is located in the middle of 3 mBSs will be detecting signals of all these macrocells as illustrated in Fig. 4.5. In this scenario, a co-channel femtocell would be expected to determine the occupancy of all three bands separately, and pick the band with the least occupancy to operate. However, if the occupancy rates of all 3 target bands are approximately the same, it would be reasonable that the fBS picks the band with the least number of users, which it can detect through user separation, so that the number of macrocell users affected by CCI is the smallest.

4.5.5 Determining the Close Users

In general, the mMSs that are close to the femtocell BS are determined according to the power levels in the uplink signal. These decisions might be supported by the delay information considering that the mMS transmit powers might not be identical, or a close mMS's signal might be shadowed. The necessary delay information for each mMS is obtained while performing user separation.

Table 4.2 Simulation parameters

Parameter	Value
FFT Size	512
Occupied subcarriers	360
N_{CP}, CP Duration	1/8, 11.2 μs
Number of users	10
Sampling frequency	5.714 MHz
Symbol Time	100.8 μs
Bandwidth	5 MHz
CFOs (in Hz)	[-500, -400, ..., 0, ... 400, 500]
User distances (in m)	[100, 200, 400, 600, ..., 1800]
RTDs (in samples)	[4, 8, 15, 23, 30, 38, 46, 53, 61, 69]

Also, since user separation reveals which subcarriers belong to which mMS, the power that will be transmitted by the femtocell on different subcarriers can be determined adaptively according to the relative distances of the mMSs.

4.6 Using Block Size Estimation and User Separation in Spectrum Opportunity Detection

Opportunistic spectrum usage is one of the main goals of a cognitive radio. It requires that the CR reliably determines the temporarily empty parts of the spectrum of a primary network and utilizes them without causing any interference to the primary network. In this section, we propose techniques that make use of the user separation and block size estimation methods proposed in the previous sections in order to improve the opportunity detection performance.

In an OFDMA based primary network, the spectrum opportunities correspond to the unused subcarriers within the spectrum. A simple method that might be employed for the detection of these opportunities by the cognitive radios is energy detection, where, the unused subcarriers may be simply identified through hytpothesis test as follows[5]

$$\left| Y(m,k) \right|^2 \underset{H_0}{\overset{H_1}{\gtrless}} \zeta \ . \tag{4.19}$$

However, with subcarrier based opportunity detection as in (4.19), each of the individual subcarriers are subject to false alarms and mis-detections. As an alternative, if the resource block size is perfectly known, the opportunities within the spectrum of a primary system can be determined via tile-based energy detection using (4.9). Since all the subcarriers within the same tile should all be affiliated with the same hypothesis (i.e., all subcarriers should be occupied, or, all subcarriers should be non-occupied), probability of mis-detections and probability of false-alarms will be minimized compared to the subcarrier-based detection. If the resource block size is not known, on the other hand, block size detection algorithm

---

[5]Similar to (4.9), hypothesis H_1 implies that a subcarrier is occupied, and hypothesis H_0 implies that it is not.

84

as in Section 4.3 can be utilized to estimate the resource block dimensions and improve the opportunity detection performance with respect to the subcarrier-based detection.

As a third technique, we also propose an additional method in order to decrease the false-alarm probability of the block (tile) based opportunity detection with perfect block size knowledge. In this approach, which we will call user separation based opportunity detection, we consider each resource block with index j that is estimated to belong to hypothesis H_1 (i.e., detected as occupied). Then, hypothesis for the resource block j is changed to H_0 if any of the following criteria is satisfied for the resource block:

- $\{\hat{\tau}_j^{(1)}, \hat{\tau}_j^{(2)}\} < 0$, i.e., the delay estimates for tile-j are smaller than 0.

- $|\hat{\tau}_j^{(1)} - \hat{\tau}_j^{(2)}| > \tau_{\text{thrs}}$, i.e., different delay estimates for the same resource block have a considerably large difference.

- $|\hat{\xi}_j| > \xi_{\max}$, i.e., the absolute value of the CFO estimate for tile-j is larger than the maximum possible CFO value.

- $|\hat{\xi}_j^{(1)} - \hat{\xi}_j^{(2)}| > \xi_{\text{thrs}}$, i.e., different CFO estimates for the same resource block have a considerably large difference.

As will be shown in Section 4.7, the performance of user separation based opportunity detection can be improved using the above tests that pose some constraints on the occupied resource blocks.

4.7   Simulation Results

Computer simulations were performed in order to determine the success rate in blind block size estimation, to test the performance of the proposed user separation algorithm, and to determine the opportunity detection performance using various methods. In the simulations, the basic system parameters are set according to the WiMAX UL-PUSC standard, and both an AWGN channel and a 6-tap multipath channel (ITU-R Vehicular A) are employed. Detailed simulation parameters are provided in Table-4.2, where RTD stands for the round-trip-delay.

85

4.7.1 Block Size Estimation Simulations

The performances of the block size estimation method as well as the Gaussian approximation are simulated using two separate $Y(m,k)$'s that are 60 symbols and 120 symbols long.

The variation of the performances with respect to signal-to-noise ratio (SNR) is plotted for both AWGN and multipath (MP) channels in Fig. 4.6 and Fig. 4.7, where the block sizes to be found are 4×3 and 6×6, respectively.

The results show that the performance heavily depends on the block size. While the simulated performance is 100% in all cases examined for the 4×3 block, it can be around 70% for the 6×6 block when the SNR is low. There are two reasons for the relatively lower performance for the 6×6 block. First, the number of symbols and rows with pilot subcarriers is lower, which weakens the desired correlation peaks. And second, the physical separation between the pilots is larger, which, in a MP channel, decreases the correlation between them due to the variation of the channel in time and frequency. It is also worth to note that the Gaussian approximation matches with the simulation results quite well for the 4×3 block. The match between the simulations and the GA is still acceptable for the 6×6 block when 120 symbols are available. When there are just 60 symbols, however, there is an apparent difference between them. This is due to the fact that μ_{l_p} cannot be estimated reliably over 60 symbols, and also the correlation between the non-pilot subcarriers has a non-zero value that is considerably larger than in case of 120 symbols.

4.7.2 User Separation Simulations

Performance of the proposed user separation algorithm was tested via simulations using the following performance metrics:

Performance in finding the number of users:

$$P_{N_u} = 100 \times \left(1 - \frac{\left| \hat{N}_\mathrm{u} - N_\mathrm{u} \right|}{N_\mathrm{u}} \right) \tag{4.20}$$

86

Performance in finding the user subcarriers:

$$P_\Gamma = 100 \times \frac{\sum_{i,k} \delta_D\big(\hat{\Gamma}_i(k) - \Gamma_i(k)\big)}{\sum_i N_i} \ , \qquad\qquad (4.21)$$

where δ_D is the Dirac delta function. The performances obtained in AWGN and MP channels using a 4×3 block are demonstrated in Fig. 4.8. The assumption in the corresponding simulations was that the received SNR is the same for all users regardless of their distance[6]. The performance at each SNR is maximized by employing the optimum cluster dimension given by $\sqrt{\mathrm{Var}\big(\mathcal{A}^{(\tau)}\big)/\mathrm{Var}\big(\mathcal{A}^{(\xi)}\big)}$. The results show that better than 90% user separation performance is achievable for sufficiently high SNR values.

In Table-4.3, additional simulation results are provided for a practical scenario, where the received powers from different users depend on their distances to the receiver as specified in Table-4.2 (free space path loss model is considered). The transmission power of users is 27 dBm, and the received signal SNRs descend from 30 dB towards 5 dB. The blocks whose power levels do not exceed a certain threshold are discarded as in (4.9). Simulation results in Table-4.3 show that P_{N_u} values that exceed 80% and P_Γ values close to 80% are achievable.

Another analysis is performed to investigate the effect of number of users on the performance in finding the user subcarriers. P_Γ is obtained for N_u values 5, 10, and 20. The CFOs of users are equally spaced between -500 Hz and 500 Hz, while the user distances are equally spaced between $2000/N_\mathrm{u}$ and 2000 meters. The P_Γ curves obtained for both AWGN and MP channels are shown in Fig. 4.9. It is observed that a smaller user number such as 5 yields considerably higher performance, especially in AWGN channel. It is also important to note that when the SNR level is high enough, even 20 user signals can be separated with an accuracy rate that exceeds 80%.

---

[6]Note that if the cognitive radio performing user separation is close to the primary receiver, such a scenario may be valid. Due to power control, the SNRs of the received UL signals at the primary receiver (e.g., a macrocell BS) would be similar; hence, a close-by cognitive radio (e.g., a femtocell BS) would also observe similar SNR levels.

87

4.7.3 Opportunity Detection Simulations

The results of the opportunity detection simulations are demonstrated in Fig. 4.10 and Fig. 4.11. The error probability is computed as the sum of probability of false alarms (PFA) and probability of missed detections (PMD). PFA is the ratio of the number of subcarriers detected as used although they are unused to N, whereas PMD is defined as the ratio of number of subcarriers detected as unused although they are used to N. In the related simulations, the occupancy rate of the subcarriers is kept at 50% to have equal contribution from PMD and PFA to the total error probability.

In Fig. 4.10, the error probabilities for four different methods are shown for an optimum ($\zeta = 0.15$) and for a non-optimum ($\zeta = 0.50$) normalized threshold value, where the block size of the primary system is 4x3. The methods that are employed are subcarrier based, user separation based, tile based with known tile size, and tile based with estimated tile size. It is observed that the subcarrier based method yields the worst performance, while the tile based method performs the best. Therefore, if the tile size is not known, instead of employing the subcarrier based method, first the proposed tile size estimation can be performed and then the tile based detection method can be applied. Given that the proposed tile size estimation for this small block size is very accurate, this way, the detection performance can be made as good as in the known tile size case. User separation based method is seen to introduce some errors and to degrade the performance when the threshold is optimum. If the optimum threshold is not available and an intuitive value such as 0.5 is employed, however, then the user separation based method improves the performance.

Error probability curves obtained for a block size of 6x6 are demonstrated in Fig. 4.11. Being different from the 4x3 case, for a 6x6 block, the block size estimation method does not perform very well. Therefore, the subcarrier based detection method is superior to the tile based method with tile size estimation. It is noteworthy that the user separation based method is slightly superior to the tile based method for both optimum and non-optimum thresholds.
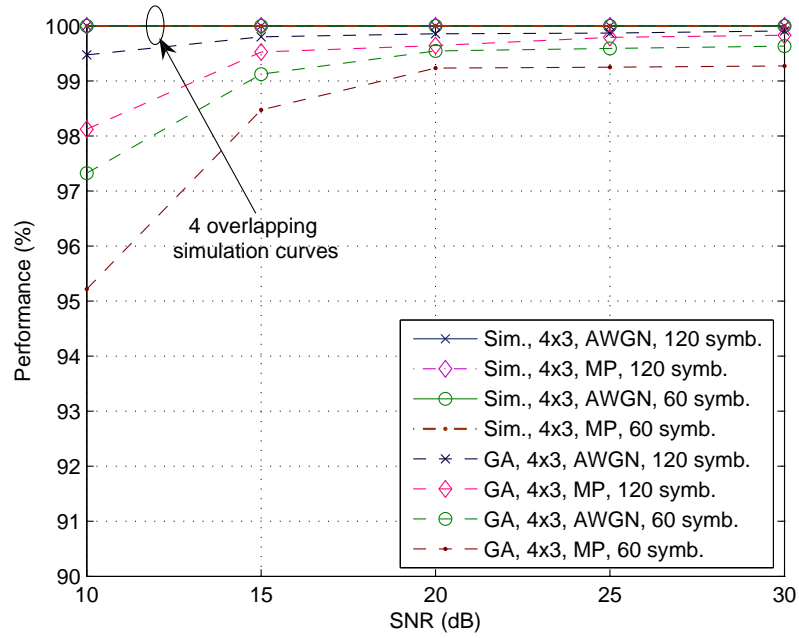
Figure 4.6 Simulation and Gaussian approximation results for estimating the size of a 4x3 block.
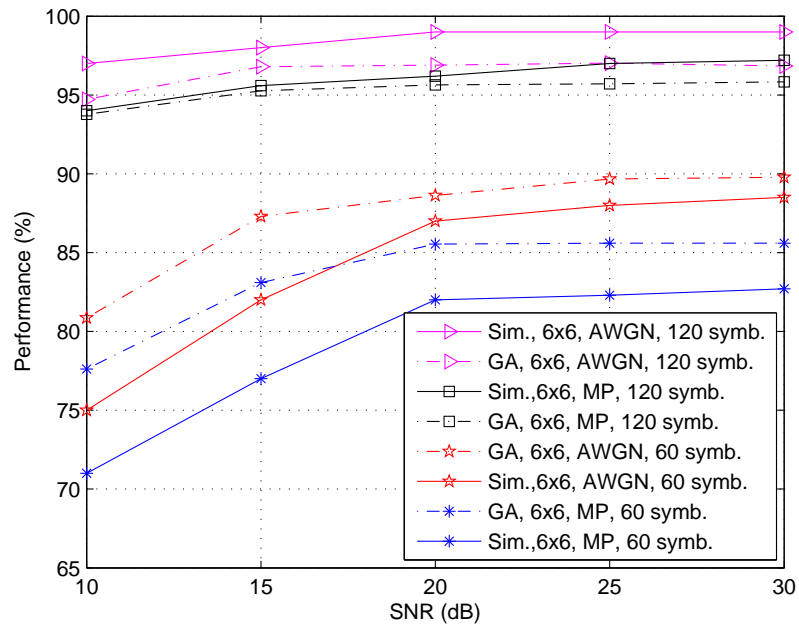
Figure 4.7 Simulation and Gaussian approximation results for estimating the size of a 6x6 block.

89
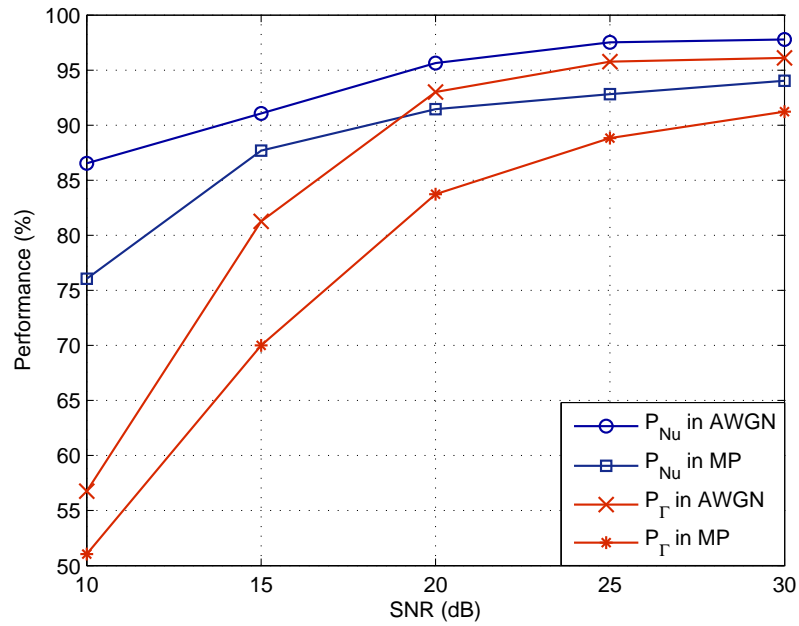
Figure 4.8 Performances in finding the number of users and separating the user subcarriers in AWGN and MP channels assuming the same SNR for all users.
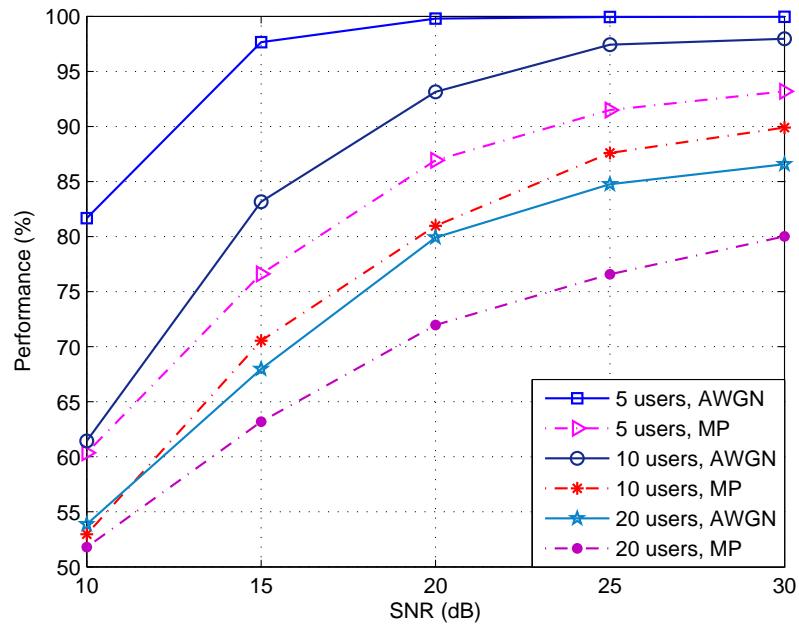
Figure 4.9 Performances in separating the user subcarriers in AWGN and MP channels for various numbers of users.

90
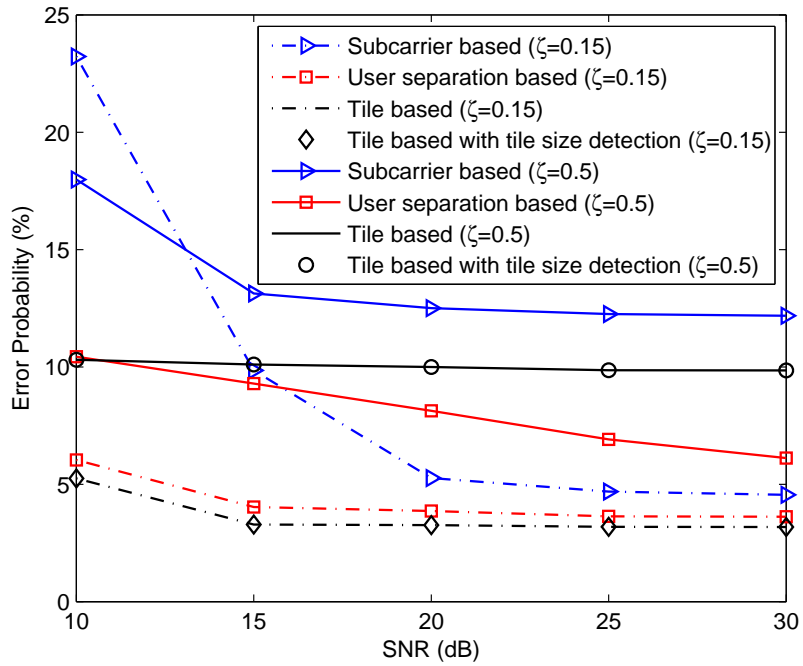
Figure 4.10 Error probability in detecting the spectrum opportunities using four different methods for a resource block size of 4x3.
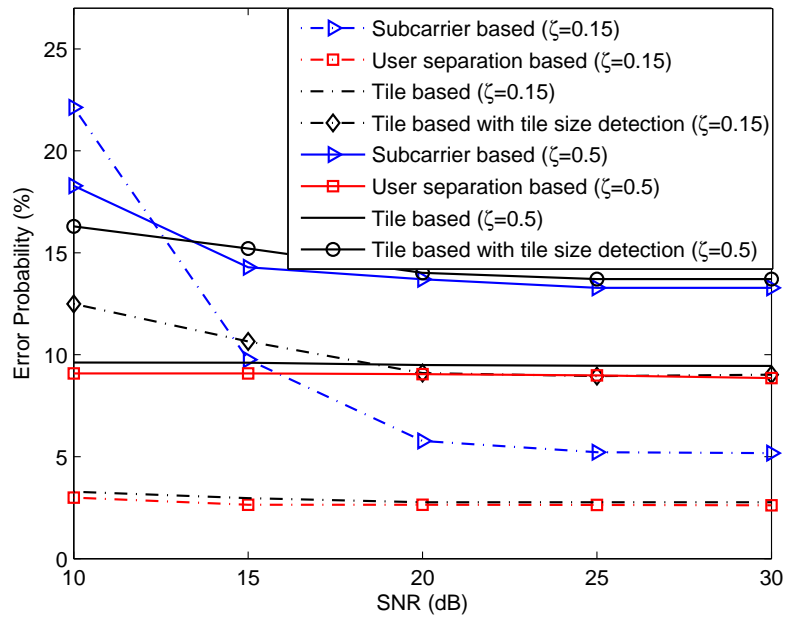
Figure 4.11 Error probability in detecting the spectrum opportunities using four different methods for a resource block size of 6x6.

91

Table 4.3 User separation performances when received powers depend on user distances

	AWGN	MP
P_{N_u}	86.07%	81.25%
P_Γ	78.55%	77.78%

4.8 Concluding Remarks

In order to increase the spectrum awareness of OFDMA based cognitive radios, separation of primary user signals in the uplink is proposed. An algorithm is devised for determining the frequency allocation block dimensions blindly. The probability of finding the block size correctly is obtained through a Gaussian approximation based approach, and it is compared with the simulated performance of the devised algorithm. Moreover a user separation method is proposed, and a rather high performance is obtained in practical computer simulations proving its feasibility. Spectrum opportunity detection is highlighted as a potential application area where the proposed methods might be considerably useful. The improvement in opportunity detection performance of cognitive radios is quantified through simulations and shown to be significant.

RECEPTION OF MIMO-OFDMA SIGNALS WITH A SINGLE CHANNEL RECEIVER

5.1   Introduction

Orthogonal frequency division multiple accessing (OFDMA) is expected to be the enabling technology for the fourth generation (4G) wireless communication systems. One of the features that make OFDMA the primary choice for 4G is its compatibility with the multiple input multiple output (MIMO) technology [78, 79], because MIMO has a very significant potential for enhancing wireless systems in capacity, data rate, and coverage aspects.

MIMO adds the multiplexing gain to the proven transmit or receive diversity gains of single input multiple output (SIMO) and MISO systems as a result of operating on a number of parallel channels [80]. It can achieve the high spectral efficiency desired by future bandwidth-greedy wireless systems at the expense of increased hardware and computational complexity. MIMO is especially important for OFDMA based WiMAX systems because it is a part of the IEEE 802.16 and 802.16e standards [81, 82], which are considered suitable candidates for 4G [83, 84].

Optimally, MIMO signal reception is performed either by using multiple receivers or a receiver with multiple RF front-ends. In both cases, the hardware cost is a significant concern. In this chapter, an attractive solution to this concern is provided that employs a single receiver. Considering a WiMAX MIMO system, the primary RF front-end impairments are analyzed, and a guide to estimate each of them is provided. The possible reasons for different impairments in different transmitter branches are addressed. Furthermore, a complete

procedure that explains how to process WiMAX MIMO signals with a single receiver is given. The procedure handles the signal from its reception up to the symbol decision stage.

The flow of the chapter is as follows. Section 5.2 discusses the primary RF front-end impairments. Section 5.3 provides a guide to estimate and remove the effects of RF front-end impairments. Section 5.4 analyzes the challenges of MIMO systems in comparison to a single channel system in detail. Section 5.6 describes how to handle WiMAX MIMO signals. Section 5.7 provides the details about combining the transmitted WiMAX MIMO signals from two transmitter branches. Section 5.9 concludes the chapter.

5.2   Signal Model and the Primary RF Front-end Impairments

In a MIMO-OFDMA system, the received signal contains the effects of various RF front-end impairments. These effects have to be determined and removed before making the symbol decisions. The detailed features of RF impairments have been addressed in [85] and [86]; here, the essential impact of each of them will be summarized so that the reader can follow the MIMO solution that will be presented.

If $X_m(k)$ is the transmitted OFDMA signal in the frequency domain, then, ignoring the inter-carrier interference (ICI) effects, the received signal can be modeled as [87]

$$
\begin{aligned}
Y_m(k) \;=\; & X_m(k)\,H_m(k)\,F(k)\exp(-j2\pi k\tau/N)\,\exp(j\pi\Omega T)\mathrm{sinc}(\pi\Omega T) \\
& \times \exp(-j\pi k\delta/f_s)\mathrm{sinc}(\pi k\delta/f_s)\,\exp(j2\pi k\Phi_m) + N_m(k)\;,
\end{aligned}
\tag{5.1}
$$

where m is the symbol index, k is the subcarrier index, T is the symbol duration, N is the FFT size, and $f_s = N/T$ is the sampling frequency. The remainder of the parameters and their effects are as follows:

- τ : The time offset between the transmitter and receiver. It causes a phase shift that increases linearly over the subcarriers, but does not change from one symbol to another;

procedure that explains how to process WiMAX MIMO signals with a single receiver is given. The procedure handles the signal from its reception up to the symbol decision stage.

The flow of the chapter is as follows. Section 5.2 discusses the primary RF front-end impairments. Section 5.3 provides a guide to estimate and remove the effects of RF front-end impairments. Section 5.4 analyzes the challenges of MIMO systems in comparison to a single channel system in detail. Section 5.6 describes how to handle WiMAX MIMO signals. Section 5.7 provides the details about combining the transmitted WiMAX MIMO signals from two transmitter branches. Section 5.9 concludes the chapter.

5.2   Signal Model and the Primary RF Front-end Impairments

In a MIMO-OFDMA system, the received signal contains the effects of various RF front-end impairments. These effects have to be determined and removed before making the symbol decisions. The detailed features of RF impairments have been addressed in [85] and [86]; here, the essential impact of each of them will be summarized so that the reader can follow the MIMO solution that will be presented.

If $X_m(k)$ is the transmitted OFDMA signal in the frequency domain, then, ignoring the inter-carrier interference (ICI) effects, the received signal can be modeled as [87]

$$
\begin{aligned}
Y_m(k) \;=\; & X_m(k)\,H_m(k)\,F(k)\exp(-j2\pi k\tau/N)\,\exp(j\pi\Omega T)\mathrm{sinc}(\pi\Omega T) \\
& \times \exp(-j\pi k\delta/f_s)\mathrm{sinc}(\pi k\delta/f_s)\,\exp(j2\pi k\Phi_m) + N_m(k)\;,
\end{aligned}
\tag{5.1}
$$

where m is the symbol index, k is the subcarrier index, T is the symbol duration, N is the FFT size, and $f_s = N/T$ is the sampling frequency. The remainder of the parameters and their effects are as follows:

- τ : The time offset between the transmitter and receiver. It causes a phase shift that increases linearly over the subcarriers, but does not change from one symbol to another;

- Ω : The frequency offset between the oscillators in both sides. It results in a drift that increases with time. All subcarriers in the same symbol experience the same amount of shift due to the frequency offset;

- δ : The inaccuracy between the sampling clocks of the transmitter and receiver. The sampling clock error causes a phase shift in frequency, which grows both with time and with frequency;

- Φ_m : Random phase noise, which is caused by the instability of oscillators. It leads to a phase shift that is the same for all subcarriers in the same symbol, but the amount of this shift varies between symbols because of the randomness of the phase error;

- $F(k)$: The effective combined frequency response of the analog filters employed in both the transmitter and the receiver;

- $H_m(k)$: Frequency selectivity and time dependency of the channel. Because of its frequency selectivity, the channel affects the subcarriers differently. It may also vary over time, especially if a mobile channel is considered;

- $N_m(k)$: Additive complex noise term.

5.3   Estimation and Removal of Impairments in the SISO Case

The main factors that lead to impairments in the received signal were introduced in the previous section. In the following, processing the received signal in the SISO case will be addressed. A step-by-step guide that provides the order and short explanations of the necessary impairment estimations is given below. As it will be clear, the order of the estimations is important because each estimation assumes that the other errors that affect the subcarriers in the same way have already been removed. So, after each impairment estimation, the corresponding effect has to be removed from the received signal before proceeding to the next step.

95

- *Packet Detection:* The beginning and the end of the signal packet is determined by utilizing a simple energy detection method. The threshold may have to be modified adaptively according to the received noise power. This initial step serves as a rough timing estimation.

- *Frequency Offset Estimation (Time Domain):* The received time domain signal $Y(n)$ is correlated with $Y^*(n+D)$

$$Z(n) = \sum_n |X(n)|^2 e^{-j2\pi\Omega D} \ , \tag{5.2}$$

where D is the symbol length, and $|X(n)|$ is the baseband transmitted signal. Owing to the (identical) pilot subcarriers that are repeated regularly in time, $Z(n)$ can be utilized to obtain the frequency offset by computing $\Omega = \angle Z(n)/-2\pi D$.

- *Finer Frequency Offset Estimation (Frequency Domain):* After converting the received time signal into the frequency domain, the values of all subcarriers including the pilots become available. Since the effect of frequency offset changes from symbol to symbol, a finer estimate $(\tilde{\Omega})$ can be obtained by correlating the pilots in two different symbols separated by M symbols ($P_{1,k}$ and $P_{1+M,k}^*$)

$$Z(k) = \sum_k P_{1,k} P_{1+M,k}^* = e^{-j2\pi\Omega M} \sum_k |P_{1,k}|^2, \tag{5.3}$$

and then computing $\tilde{\Omega} = \angle Z(k)/-2\pi M$.

- *Finer Timing Offset Estimation:* If the received signal contains a preamble (or a midamble) part that has been added to the signal to facilitate synchronization, a finer timing estimation can be done. Since the transmitter generates the preamble according to a certain standard, the same preamble can be generated in the receiver part, as well. Correlating the preamble with the time domain signal yields a very accurate timing estimation.

96

- *Sampling Clock Error Estimation:* Error in the sampling clock rate adds a phase shift that increases both over symbols and subcarriers. Since the effect of frequency offset (on the symbols) has already been removed, the clock error should be reliably determined by correlating pilots in different symbols.

- *Slope Estimation:* A time offset may still exists at this point, especially if no preamble was sent, since the packet estimation does not determine the signal starting point very accurately. This time offset will indicate itself as a phase shift that increases with a certain slope over subcarriers. Since the impact of the sampling clock error was already canceled in the previous step, this slope can be estimated by comparing the phases of the subcarriers in the same symbol.

- *Random Phase Error Estimation:* To determine the random phase error, pilots in different symbols have to be correlated. This correlation yields the phase error between the two correlated symbols. Since the amount of error changes randomly from one symbol to another, it has to be determined separately for each symbol.

- *Channel Estimation:* Channel estimation is done using again the pilots, which should be now free from all the impairments mentioned so far. The channel estimates for the subcarriers between the pilots are obtained by interpolating the pilot values in a reasonable way.

5.4   Challenges in MIMO Compared to SISO

As opposed to systems with a single input, in MIMO systems, the received signal includes simultaneously transmitted data from multiple transmitter antennas. Therefore, the measured error vector magnitude is based on a combined error vector, which cannot be separated into contributions from separate antennas/transmitter branches. However, under some circumstances, the impairments caused by different branches differ substantially, and a common EVM estimation fails to reflect the error magnitude for all of the branches accurately.

97

In what follows, the possible factors that lead to different impairment values will be discussed. The MIMO-OFDMA system considered here has two transmitter branches and one receiver branch.

5.4.1   Time Offset Between the Branches

In MIMO signal reception, it is desirable to assume that signals from the two transmitter branches are received simultaneously. However, there may be a time offset between the received signals if

- the transmitters are not well synchronized with each other,

- or if the distances from each transmitter to the receiver are considerably different from each other.

In case of a time offset between the transmitter branches, the timing estimation done by the receiver will not be accurate for at least one of the branches.

5.4.2   Employing Separate Clocks

The oscillator that is needed to generate the sampling instants of the digital-to-analog converter (DAC) may be common to both branches, or each branch can use a separate oscillator. If two separate oscillators are employed serving as sampling clocks, there will be an unavoidable inaccuracy between the sampling periods. This fact will lead to different sampling clock errors for each branch.

Although it is more reasonable to employ a single clock for the entire transceiver, in some cases, the different transmitter branches may run separate clocks. This will be the case if the signals are generated by different sources such as two vector signal generators, or two collaboratively operating mobile devices each with a single antenna. Even if there is a single unit with multiple output branches, since each branch will have its own DAC, there will be still two different sampling clock errors, unless the DACs are run by a common external clock input.

98

5.4.3 Using Separate IQ Modulators

The use of separate IQ modulators in each transmitter branch has various impacts. One is that it causes the IQ impairments of each branch to be different. Another one is observed on the frequency offset. Since it is certain that the output frequencies of the oscillators in each IQ modulator can never be exactly the same, the signals from each branch have a different frequency offset in the receiver part. Another effect of separate IQ modulators is seen on the random phase error. Most local oscillators display an inconsistent behavior in time in terms of the output frequency, i.e. their frequency makes slight variations in time. This impairment results in phase errors that are random in nature. Therefore, employing two separate local oscillators will lead to two independent phase errors.

5.4.4 Using Separate RF Components

Since each transmitter branch employs its own mixer, analog RF filters, power amplifier, and antenna, the signals from each branch will be modified differently before being radiated into the air. The good thing about the different RF sections is that their effects can be folded into the channel. Therefore, channel estimations can be considered to reflect the effect of the RF sections on the received signals.

5.5 Detecting the Impairment Differences by Examining the Constellation Diagram

When dealing with MIMO signals, having an idea about the potential impairment differences between the transmitter branches can facilitate the estimation and removal of these impairments considerably. If there is a vector signal analyzer (VSA) available to examine the received signal, Some of these differences can be recognized by investigating the IQ constellation diagram after the removal of offsets from the received combined signal. How the constellation looks for a QPSK modulated space-time transmit diversity (STTD) MIMO signal after the removal of offsets (and before the removal of the channel effects, i.e. equalization) is shown in Fig. 5.1. Note that there are 16 constellation points (as well as 2

99
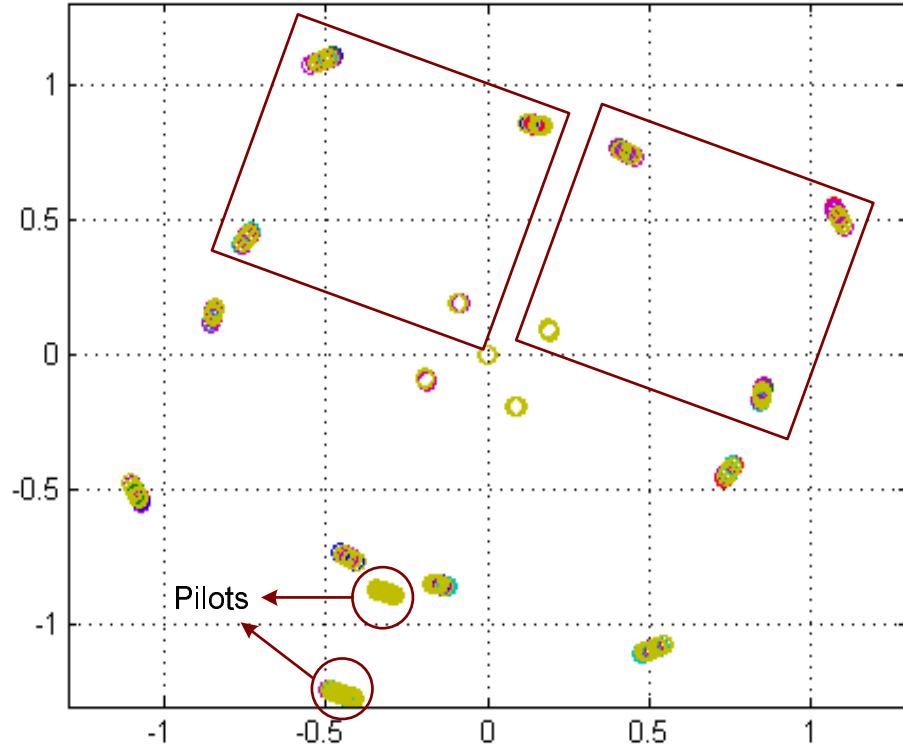
Figure 5.1 The constellation for two QPSK modulated STTD signals before equalization.

collections of pilot symbols and the point in the middle caused by the non-allocated sub-carriers) in the diagram. There are 16 points because each of the 4 constellation points in QPSK are summed vectorially with another 4 points. Two of these quadruples are explicitly indicated with rectangles in Fig. 5.1.

   Simulations have been run aiming to see what kind of effects are observed in the constellation when there are certain differences between the two transmitted signals. For this purpose, various differences were intentionally set between the two signals. When performing the corresponding simulations, it was assumed that one of the signals is not corrupted (does not have an impairment) but the other one does. That means, one of the signals has no IQ imbalance, but the other one has 30% IQ imbalance, *etc.* It should be also noted that only one type of impairment difference is assumed to exist at a time; they have been examined one by one, because it may not be possible to make a reliable guess by simply looking at the constellation if multiple such impairment differences exist at the same time.

100
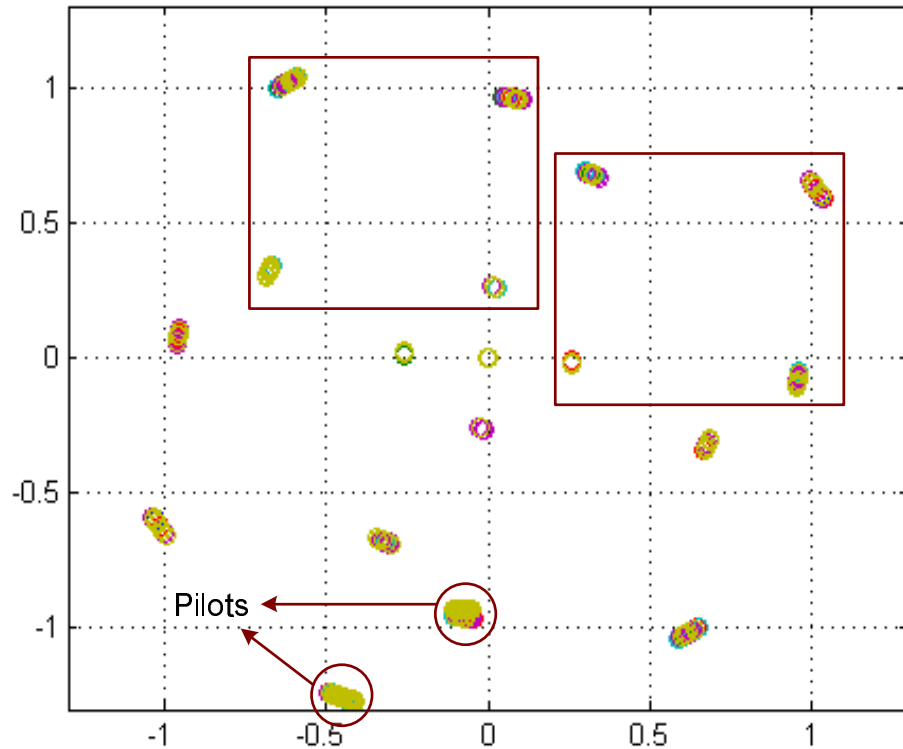
Figure 5.2 $\pi/12$ phase difference between the two transmitted signals.

In Fig. 5.2, the effect of $\pi/12$ phase difference between the two transmitted signals is observed. The rotation of the quadruples around their center is apparent. The same effect can be verified by checking the position of the pilots. Fig. 5.3 shows two signals with 30% IQ imbalance difference. In Fig. 5.4, the effect of $\pi/12$ quadrature error difference between the signals is shown. Finally, in Fig. 5.5 two signals with 0.002 radian frequency offset difference are shown. Frequency offset has a similar effect to phase difference in terms of rotation of quadruples. However, since the phase shift caused by the frequency offset increases over symbols, a clear shift is seen in the constellation points. Apparently, each of these impairment differences has a different effect on the constellation diagram, and studying these visual effects, one can make a strong guess about the possible problem with the received MIMO signal by just examining the constellation diagram.

101
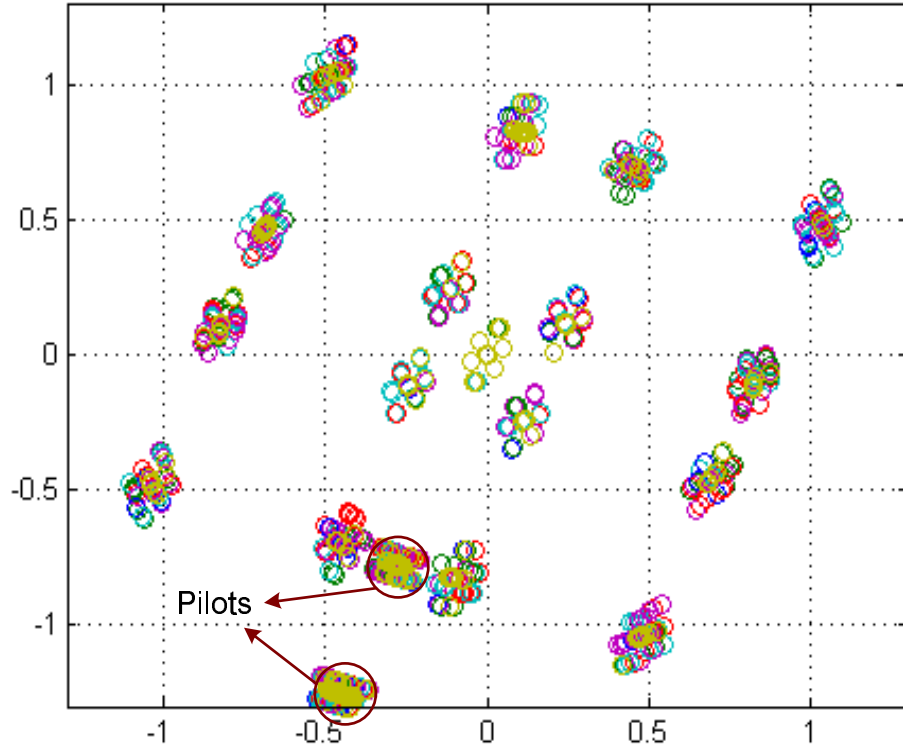
Figure 5.3 30% IQ imbalance difference between the two transmitted signals.

5.6 Procedure to Handle WiMAX MIMO Signals

Although the term MIMO implies usage of multiple receivers, it is possible to process MIMO signals with a single receiver if there is a solution to the fundamental issue how to separate the constellations and the EVM contributions of each transmitter branch. In the remainder of this chapter, a WiMAX system will be considered as an example to MIMO systems using OFDMA. To be more specific, space time coded (STC) downlink (DL) and uplink (UL) WiMAX signals with PUSC permutation will be analyzed more closely. The (frequency domain) allocations of pilot subcarriers in DL-PUSC and UL-PUSC are shown in Fig. 5.6 and Fig. 5.7. In these allocation maps, it is seen clearly that each branch is transmitting a separate set of pilots that are orthogonal to each other either in frequency or in time. Basically, this is the feature that enables separating the impairment contributions from separate branches.

102
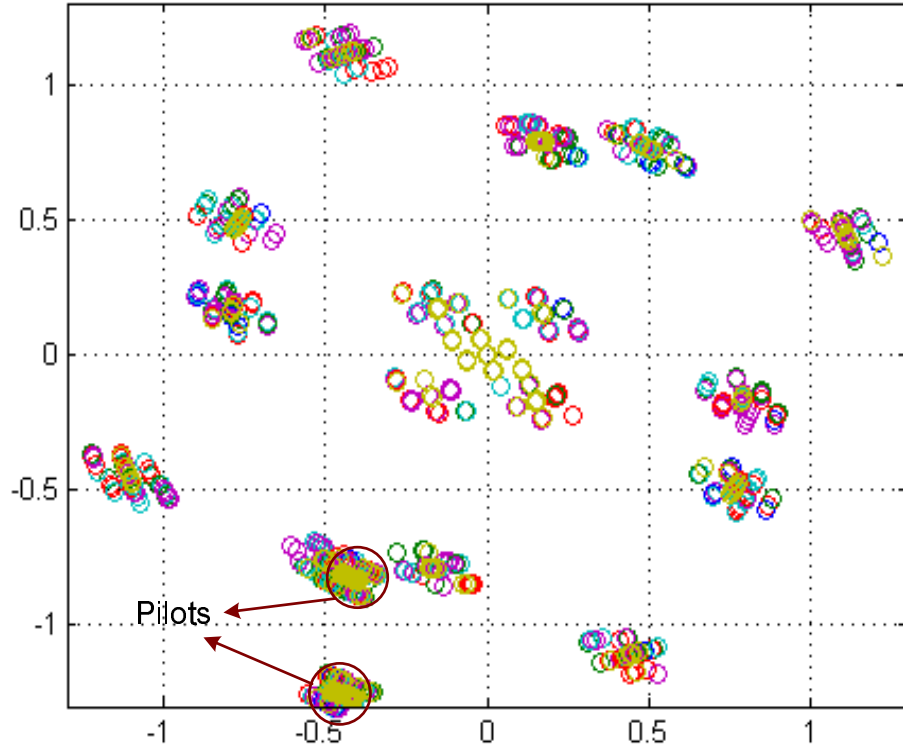
Figure 5.4 $\pi/12$ quadrature error difference between the two transmitted signals.

For testing the proposed solution two different 2×1 setups are employed. In the first setup, Tx and Rx antennas are used, whereas in the second one transmitter signals are combined with an RF combiner and fed to the receiver. The second setup is shown in Fig. 5.8. The WiMAX MIMO system settings, which are common to both setups, are given in Table 5.1. In these 1024 FFT scenarios, there are 840 subcarriers left after removing the guard bands.

The solution that will be investigated in this chapter is based on the use of pilot sequences. In WiMAX, each Tx branch is transmitting a separate set of pilots that are orthogonal to each other according to their subcarrier allocation maps. Basically, this is the feature that enables separating the impairment contributions from separate branches.

The received time domain signal contains pilot subcarriers from both branches, however, it is not possible to process these pilots separately in time. Therefore, the packet detection and the time domain based frequency offset estimation can be applicable only if the timing

103
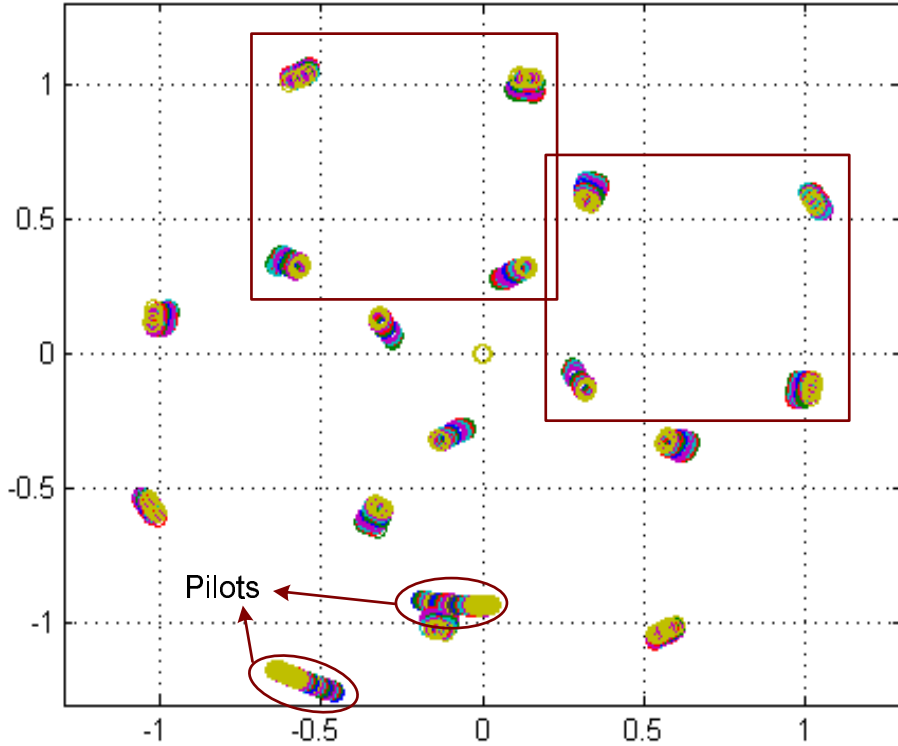
Figure 5.5 0.002 radian frequency offset difference between the two transmitted signals.

Table 5.1 WiMAX MIMO system settings

Parameter	Value
DL / UL	Downlink
Number of transmitters	2
Number of receivers	1
MIMO type	Matrix B (SMUX)
Permutation	PUSC
FFT Size	1024
Number of symbols	14
Bandwidth	10 MHz
Modulations	16QAM & 64QAM
Coding Rates	1/2 & 1/2

offsets and the frequency offsets from the two branches are close to each other. Otherwise, only after converting the signal to the frequency domain, since pilots from different branches get separated from each other, one can apply the offset estimations (explained in detail for a single channel) to pilots from each branch separately.

104
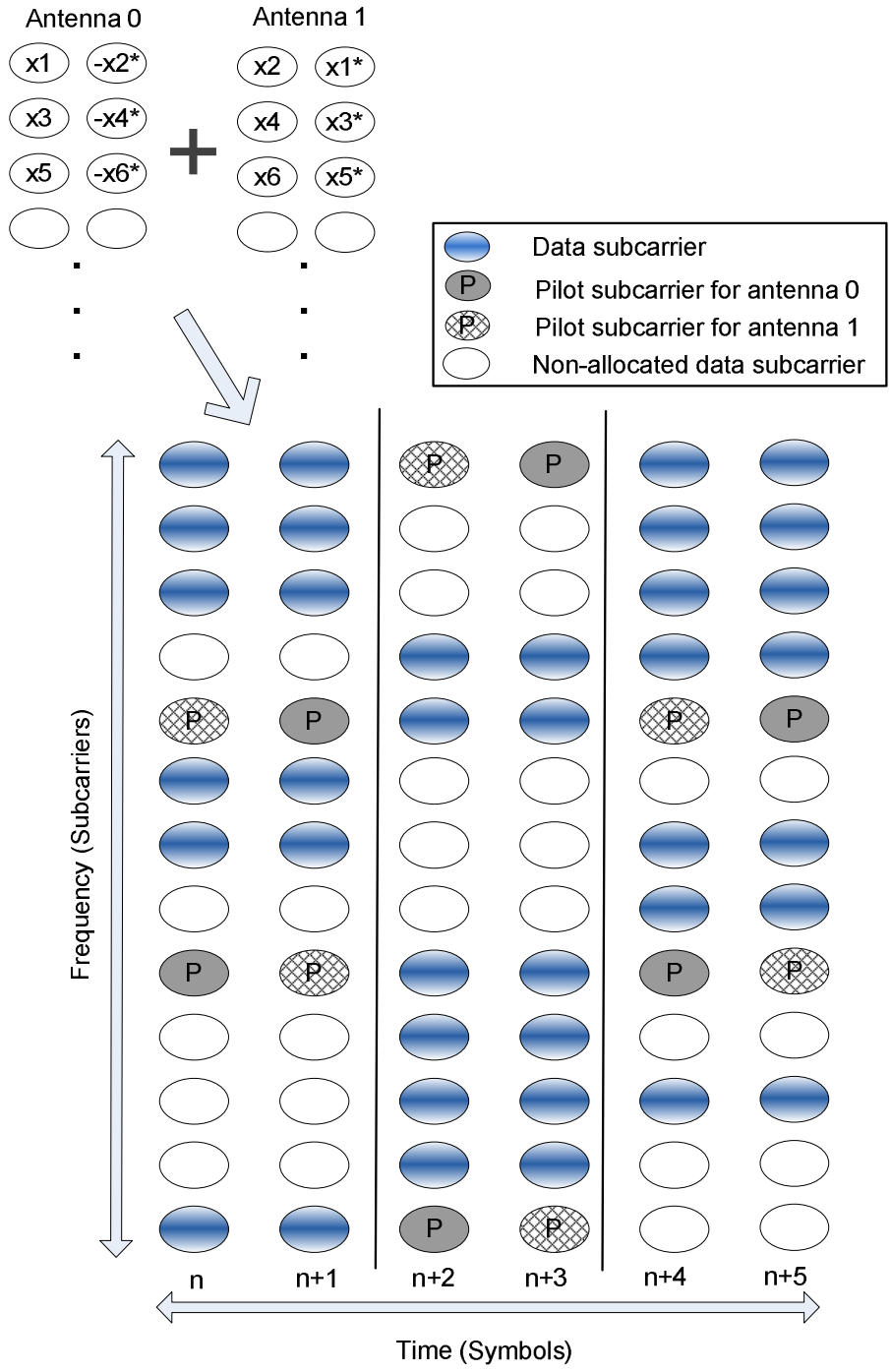
Figure 5.6 Allocation of subcarriers in downlink PUSC WiMAX. Implementation of Alam-outi (space-time) coding is shown.
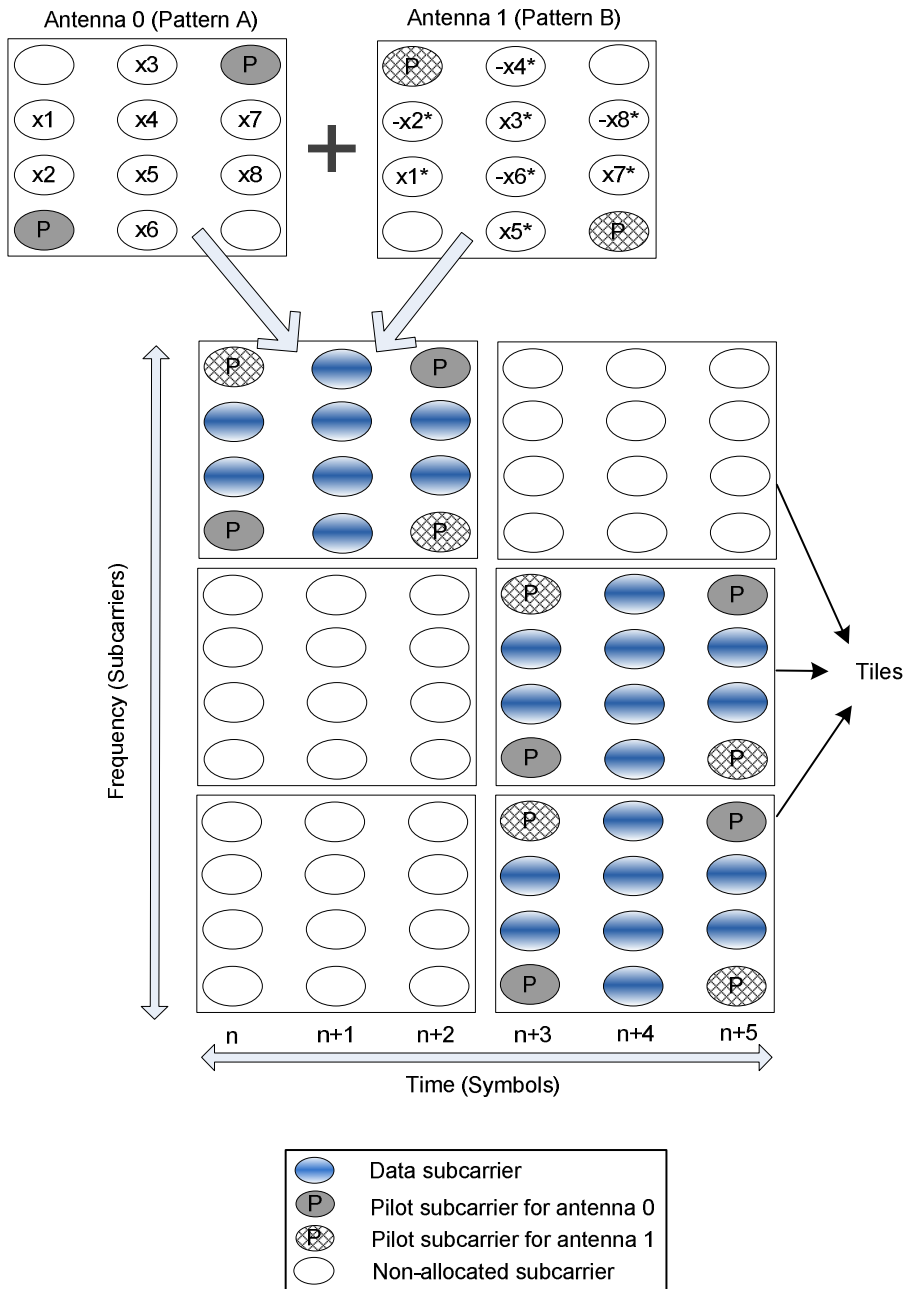
Figure 5.7   Allocation of subcarriers in uplink PUSC WiMAX. Implementation of space-frequency coding is shown.

In the single channel case, after each impairment estimation the corresponding effect was being removed from the signal. In the MIMO case, however, since each branch has different impairments, it is not valid to remove the effects from the received signal. Instead, the

106
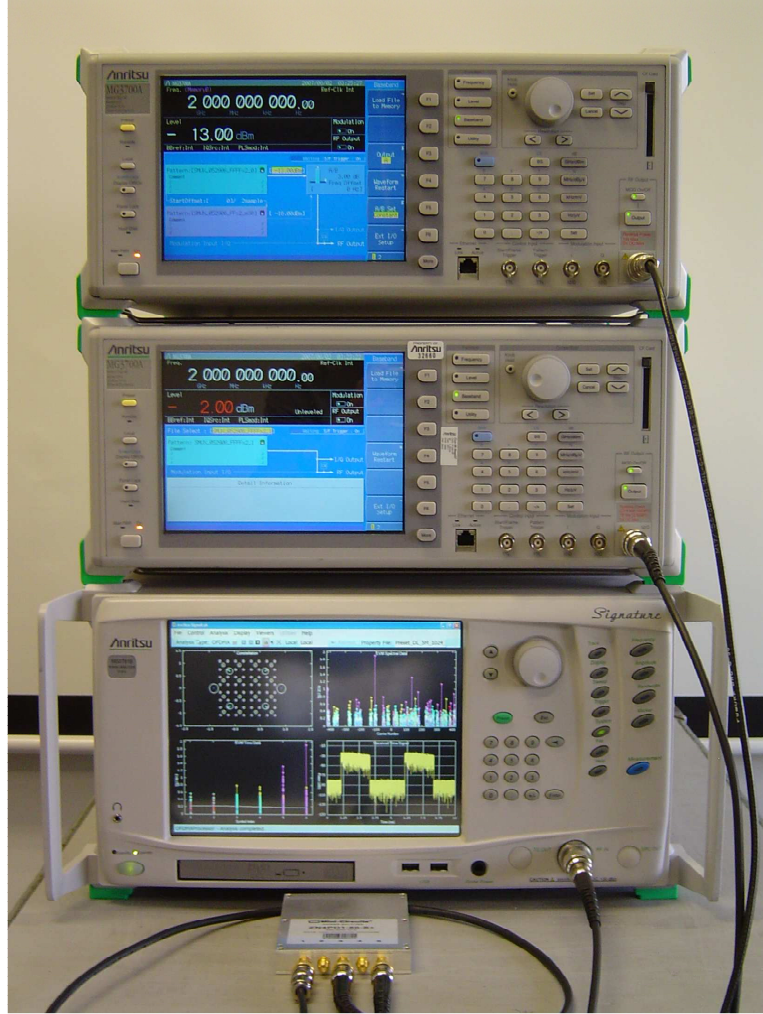
Figure 5.8 The 2x1 MIMO system setup. The outputs of the transmitters are combined with an RF combiner and provided to a single receiver.

estimated effects are removed from the corresponding set of pilots, only. After determining and removing all the effects one by one, the channel estimations $H(k)$ can be obtained from the pilot sets. Before proceeding to the symbol decision step, the impairment estimations obtained for both channels should be applied to the corresponding channel estimations as follows

$$\hat{H}_m(k) = H_m(k) \exp(-j2\pi k\tau/N) \exp(j\pi\Omega T) \exp(-j\pi k\delta/f_s) \exp(j2\pi k\Phi_m). \qquad (5.4)$$

5.7 Space-Time Transmit Diversity and Combining the MIMO Signals From Two Transmitter Branches

The two MIMO options that are considered in the 802.16 standard for WiMAX systems are the space-time transmit diversity (STTD) and the spatial multiplexing (SM). In this and the following sections, the implementation of these two methods will be explained shortly. The main focus will be on how to extract the transmitted information from the received signals in each case.

In the STTD case, Alamouti encoding [88] is applied to subcarrier pairs, where the same subcarriers of two consecutive OFDMA symbols constitute a pair. In the receiver part, the STTD signals are combined in a special way that will be explained shortly. A single receiver is enough for combining STTD signals, and this is very appropriate for the purpose of employing a single receiver to keep the hardware cost at a minimum.

In the STTD implementation for DL-PUSC WiMAX, which is illustrated in Fig. 5.6, the signals of the subcarriers x_1 and x_2, which constitute a subcarrier pair, are transmitted as $[x_1, -x_2^*]$, respectively, from the first antenna, and in the order of $[x_2, x_1^*]$ from the second antenna, according to the Alamouti coding. In the receiver, the signals received at consecutive symbol times on each carrier pair are

$$Y_1(k) = H_1(k)x_1 + H_2(k)x_2 + N_1 \ , \tag{5.5}$$

$$Y_2(k) = -H_1(k)x_2^* + H_2(k)x_1^* + N_2 \ , \tag{5.6}$$

where $H_1(k)$ and $H_2(k)$ are the channel responses, and N_i is noise. These two received signals can be combined in two different ways to yield the transmitted signals as follows

$$
\begin{aligned}
C_1 &= \hat{H}_1(k)^* Y_1(k) + \hat{H}_2(k) Y_2(k)^* \\
&= x_1(|\hat{H}_1(k)|^2 + |\hat{H}_2(k)|^2) + \hat{H}_1(k)^* N_1 + \hat{H}_2(k) N_2^* \ , \tag{5.7}
\end{aligned}
$$

$$
\begin{aligned}
C_2 &= \hat{H}_2(k)^* Y_1(k) - \hat{H}_1(k) Y_2(k)^* \\
&= x_2(|\hat{H}_1(k)|^2 + |\hat{H}_2(k)|^2) + \hat{H}_2(k)^* N_1 - \hat{H}_1(k) N_2^* \ , \tag{5.8}
\end{aligned}
$$

108

where $\hat{H}_i(k)$ are the channel estimations. Assuming that noise has a limited effect, a reliable estimation for x_1 and x_2 can be obtained by $C_1/(|\hat{H}_1(k)|^2 + |\hat{H}_2(k)|^2)$ and $C_2/(|\hat{H}_1(k)|^2 + |\hat{H}_2(k)|^2)$, respectively.

In UL-PUSC WiMAX, on the other hand, the implementation of STTD is different. Alamouti coding is applied to adjacent subcarriers in the same symbol (rather than the same subcarriers in adjacent symbols), as illustrated in Fig. 5.7. Therefore, it is more like space-frequency coding rather than space-time coding. In the receiver, the signals received at consecutive subcarrier locations are

$$
Y_1(k) = H_1(k)x_1 - H_2(k)x_2^* + N_1 , \tag{5.9}
$$

$$
Y_1(k+1) = H_1(k+1)x_2 + H_2(k+1)x_1^* + N_2 , \tag{5.10}
$$

These signals are combined as follows

$$
C_1 = \hat{H}_1^* Y_1(k) + \hat{H}_2 Y_1(k+1)^* , \tag{5.11}
$$

$$
C_2 = \hat{H}_1^* Y_1(k+1) - \hat{H}_2 Y_1(k)^* , \tag{5.12}
$$

and the transmitted signals x_1 and x_2 can be obtained as in the case of space-time coding.

5.8   Spatial Multiplexing and Joint Demodulation

In spatial multiplexing, each branch transmits a different signal. Ideally, there should be N receivers if there are N transmitter branches. This way, N independent copies of each transmit signal can be received. By making use of the channel information, these copies are combined to obtain the desired signals. If there is a single receiver available, however, the transmitted signals can only be obtained by doing joint demodulation [89].

In joint demodulation, at every subcarrier each possible IQ signal pair $[X_1(k), X_2(k)]$ is considered to be a hypothesis. Each hypothesis is simulated by applying the channel

109

responses, and the best hypothesis is determined via a maximum likelihood method

$$\left[\hat{X}_1(k), \hat{X}_2(k)\right] = \arg \min_{X_1(k), X_2(k)} \left\{ \left| Y(k) - \hat{H}_1(k)X_1(k) - \hat{H}_2(k)X_2(k) \right|^2 \right\}, \qquad (5.13)$$

where $Y(k)$ is the received signal, $X_1(k)$ and $X_2(k)$ are the two signals that constitute the hypothesis, and $\hat{H}_1(k)$ and $\hat{H}_2(k)$ are the corresponding channel estimates.

If two transmitter antennas, each transmitting, for example, a QPSK modulated signal, are considered, then there are 4^2 hypotheses to check for each received data subcarrier, which does not pose a serious computational challenge. However, the complexity of this method increases proportional to M^c, where M is the modulation order, and c is the number of transmitter branches. Therefore, for MIMO applications that employ a number of transmitters and use higher order modulations, the computational complexity may set a practical limit to the feasibility of this method. A version of joint demodulation that utilizes multiple receivers can be considered as a solution in such a case.

5.9   Conclusion

In this chapter, reception of OFDMA based MIMO signals with a single receiver is handled. For the OFDMA based signals, the causes for the primary impairments and the way of eliminating their effects are addressed. Challenges in signal reception that are specific to MIMO scenarios are analyzed in comparison to the single transmitter case. It is explained how to make intelligent guesses about the potential problems in received MIMO signals by examining the constellation diagrams. Finally, but very importantly, a maximum likelihood based method that enables receiving MIMO-OFDMA signals transmitted from two transmitter branches with a single receiver is presented.

AN ITERATIVE INTERFERENCE CANCELLATION METHOD FOR CO-CHANNEL MULTICARRIER AND NARROWBAND SYSTEMS

6.1 Introduction

Transition from third generation (3G) to the fourth generation (4G) wireless systems is a major challenge that will be faced in the near future. Two different physical (PHY) layer technologies that have a high chance of being employed by next generation systems are Long Term Evolution (LTE) and WiMAX, both of which are multicarrier (MC) systems and can have a bandwidth up to 20 MHz. Relative to these technologies, 3G systems such as EDGE, DECT, CDMA-2000, and even W-CDMA with its 5 MHz bandwidth need to be considered as narrowband (NB) systems. During the transition phase from 3G to 4G, various multicarrier and NB systems might have to share the same spectrum, which will result in a severe performance degradation in both systems due to the co-channel interference (CCI).

Suppression of narrowband interference (NBI) in OFDM systems was considered in the prior-art [90]- [93]. In [90], linear minimum mean-square error (LMMSE) estimates of the interference are utilized. The proposed algorithm requires a priori information about the power spectral density of the NB signal. In [91], a normalized least mean squares (N-LMS) adaptive noise cancellation algorithm was introduced for suppressing NBI in pilot symbol assisted OFDM systems. NBI rejection via interferometry spreading codes was proposed in [92]. In [93], an NBI canceller for OFDM systems is considered, where the NB signal is estimated over the unused OFDM subcarriers. The feasibility of this method is limited in practice due to the very few number of unused subcarriers in a well designed OFDM based

111

system. In this chapter, we treat both co-channel signals as desired signals and propose a method that combats CCI through enhancing both signals in an iterative manner. In the literature, iterative co-channel interference cancellation was considered in [4]- [99], which typically focus on narrowband systems and consider that the interferer and victim both use the same technology. In most of these works, the *hunch* effect has been typically observed in the performance results: 1) The bit-error-rate (BER) performance improves with the increasing signal to interference ratio (SIR) for low SIR values[1], 2) It starts degrading with the increasing SIR for moderate interference levels and gets worse when the interference power is comparable with the desired signal power, and 3) BER starts improving again as the SIR increases further. Therefore, it is argued that interference cancellation is most effective when the interference is sufficiently strong.

In [4], it is emphasized that by exploiting the differences in signal features such as their delays, initial signal separation can be obtained, which considerably increases the efficiency of iterative interference cancellation. In the current chapter, we exploit the inherent initial signal separation that exists due to the multicarrier vs. single carrier natures of interfering signals as well as the fact that the information is in frequency domain for MC signal and in time domain for NB signal. The proposed method assumes availability of signal reception and transmission capabilities for both systems. At each iteration, each signal is demodulated and then regenerated based on the symbol decisions and the channel impulse response. This way, a better estimate of the signal is obtained. The regenerated signal is subtracted from the aggregate signal to obtain an estimation of the other co-channel signal. Through extensive simulations, it is proved that this method can provide a fundamental improvement in the performances of both systems in as few as three iterations. The relatively high computational burden (associated with multiple transitions between time and frequency domains) as well as the extra cost caused by the addition of a second system's transceiver functionalities are compensated by the fundamental performance gain obtained. Our other contributions include a detailed comparison of the computational complexity of

---

[1]In other words, interference cancellation works effectively if the received interference is strong and can be separated easily from the desired signal.

112

the proposed method with the joint demodulation technique and evaluation of the Gaussian approximation (GA) method for characterizing the interference from the other system.

The chapter is organized as follows: Section 6.2 provides application examples and the system models for the MC and NB systems in consideration. Also, it shortly discusses the GA based symbol error rate (SER). Section 6.3 reviews the joint demodulation technique for the NB and MC signals, while Section 6.4 is a detailed description of the proposed CCI cancellation method. A complexity comparison of the joint demodulation and iterative interference cancellation approaches is made in Section 6.5, simulation results are presented in Section 6.6, and the last section concludes the chapter.

6.2 Application Examples and System Model

6.2.1 Application Examples

Earlier examples of coexistence studies in the prior art include [100] and [101], which investigate the coexistence of code division multiple access (CDMA) and GSM systems. A contemporary example scenario, where coexistence of NB and multicarrier systems might be unavoidable, is the co-channel deployment of wideband CDMA (W-CDMA) based femtocells with LTE based macrocells, which has not been studied in the literature to our best knowledge. Femtocells [28, 29] are miniature cellular networks that have a communication range in the order of 10 meters. They can coexist with a macrocell network through either a split-spectrum approach, which leads to an inefficient spectrum utilization, or a shared-spectrum approach [30]- [102], where CCI is a potential concern. The initial deployments of femtocells will be mostly based on CDMA based technologies, such as the W-CDMA. In the future, while macro-cellular networks migrate to wider-band multicarrier-based technologies such as LTE, it might be expected that it takes a longer time for the consumers to replace their existing 3G femtocells with their next-generation versions. Hence, an LTE based macrocell may need to coexist with a large number of 3G femtocells within its coverage area. In a shared-spectrum deployment, this would result in an interference from the macrocell at a femtocell, as illustrated in Fig. 6.1, which needs to be cancelled at the

113
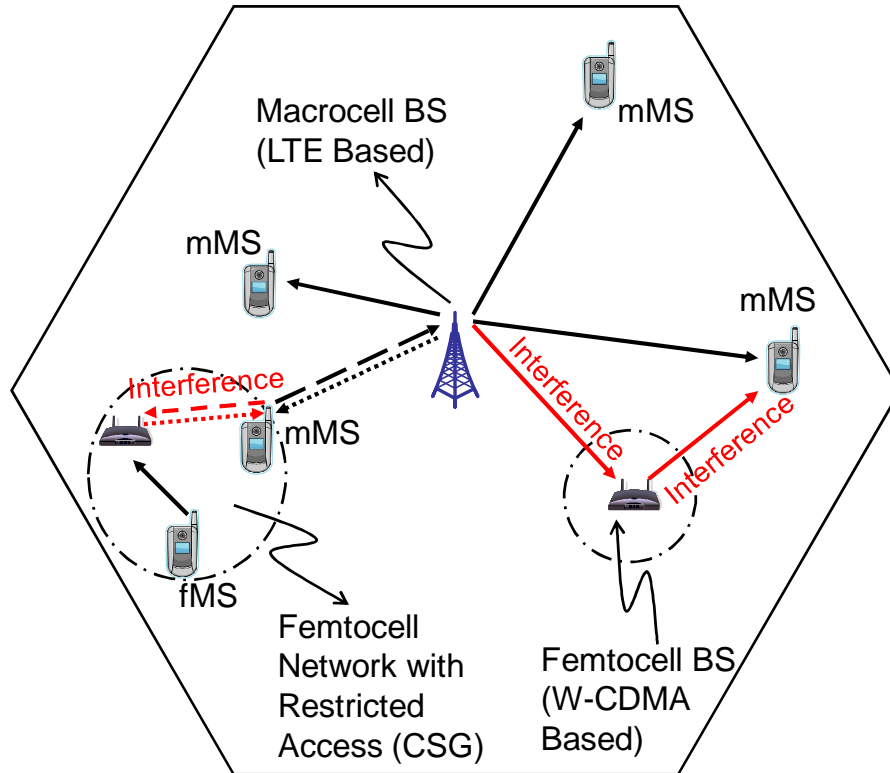
Figure 6.1 An example coexistence scenario for an LTE based macrocell with a W-CDMA based femtocell during migration from 3G to 4G.

femtocell for an improved performance. Similarly, a W-CDMA femtocell may be interfering to an LTE based mobile station (MS) nearby, which again needs to be mitigated at the MS.

A particularly important scenario where interference cancellation may yield good gains for femtocell networks is for the restricted operation mode[2] of femtocells, where, the macrocell mobile stations (mMSs) are not allowed to make hand-off to the femtocell network even when the signal quality is superior at the femtocell. As illustrated in Fig. 6.1, this may result in significant uplink interference from the mMS to the femtocell MSs (fMSs), and significant downlink interference from the fMS to the mMSs. As discussed before, for the interference cancellation to become effective, the interference should be sufficiently strong; therefore, femtocells with restricted access are a good application scenario for interference cancellation techniques.

_____

[2]Also referred as the closed subscriber group (CSG) operation.

Another related example is the coexistence of multicarrier based ultra-wideband (UWB) systems (see e.g., [103]) with the relatively narrowband technologies (e.g., W-CDMA etc.)[3]. It has been shown in [105] that multiband orthogonal frequency division multiplexing (MB-OFDM) interference may seriously degrade the performance of NB systems at low signal-to-interference ratios (SIRs). While detect-and-avoid approaches as in [106] are possible solutions for coexistence, it may not always be feasible to reliably detect the interference. Also, joint use of the spectrum may be more efficient in several scenarios if interference cancellation techniques can be successfully deployed. These scenarios include applications in the ISM bands where MC systems like WiFi coexist with NB systems like cordless phones and bluetooth devices.

6.2.2 System Model

In this chapter, two different co-channel interference scenarios are considered. The first scenario involves a MC and NB coexistence, and the second one deals with a MC and CDMA systems coexistence. The MC system employed has an orthogonal frequency division multiple accessing (OFDMA) based PHY layer. In both scenarios, it is assumed that the transceiver functionalities of both co-channel systems are available, but the primary receiver is the OFDMA receiver, i.e. perfect time and frequency synchronization to the OFDMA signal is ensured. This fact is illustrated in the diagram in Fig. 6.2, which shows the NB and OFDMA signals in time and frequency domains. It is demonstrated that synchronizing to the OFDMA symbols rather than NB symbols is necessary even if a targeted packet of NB symbols starts and ends somewhere in the middle of the OFDMA symbols.

The sampled downlink OFDMA signal in time domain can be written as

$$x(n) = \sqrt{P_{\text{tx}}} \sum_{k=0}^{N-1} X(k) e^{j2\pi kn/N}, -N_{\text{cp}} \leq n \leq N - 1, \tag{6.1}$$

---

[3]Note that 60 GHz technologies as in [104] also have multicarrier transmission as an option and may face similar coexistence problems. Several other scenarios for the coexistence of a narrowband and multicarrier system may also be considered.

115
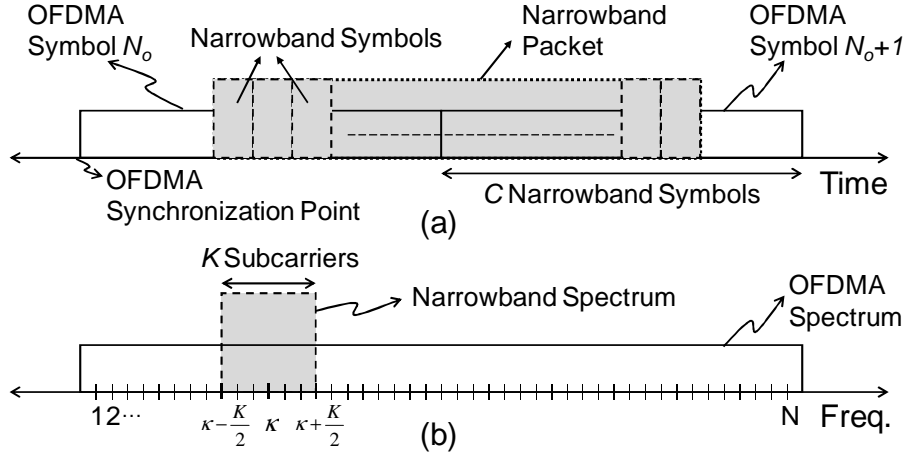
Figure 6.2 Diagram of the OFDMA and NB symbols in time and frequency.

where P_{tx} is the transmit power, N is the number of subcarriers, k is the subcarrier index, N_{cp} is the length of the cyclic prefix (CP), and $X(k)$ is the data on the kth subcarrier.

The received time domain OFDMA signal that traverses through a multipath channel $h(l)$ with L_{mc} taps is

$$y(n) = \sqrt{P_{\mathrm{rx}}} \sum_{l=0}^{L_{\mathrm{mc}}-1} h(l)x(n - D_l) , \qquad (6.2)$$

where P_{rx} is the received signal power, and D_l is the delay of the lth tap. Assuming that the maximum tap delay does not exceed the CP length, the frequency domain OFDMA signal can be shown as

$$Y(k) = \sqrt{P_{\mathrm{rx}}}X(k) \sum_{l=0}^{L_{\mathrm{mc}}-1} h(l)e^{-j2\pi kD_l/N} = \sqrt{P_{\mathrm{rx}}}X(k)H(k), \qquad (6.3)$$

where $H(k)$ is the channel frequency response.

The baseband narrowband signal can be modeled as

$$s(n) = \sum_m a_m g(n - mT) , \qquad (6.4)$$

where m is the symbol index, a_m denotes the mth data symbol, $g(n)$ is the pulse shaping filter with a roll-off factor α, and T is the symbol duration of the narrowband signal. In

116

case of a CDMA signal, $s(n)$ becomes

$$s(n) = \sum_m a_m g(n - mT) p(n - mT) \; , \tag{6.5}$$

where $p(n)$ is the spreading chip sequence with R_c chips. Since $s(n)$ passes through a multipath channel $h'(l)$ with L_{nb} symbol-spaced taps[4], the received signal becomes

$$z(n) = \sqrt{P_{\mathrm{rx}}} \sum_{l=0}^{L_{\mathrm{nb}}-1} h'(l) s(n - lT) \; . \tag{6.6}$$

The discrete Fourier transform (DFT) of $z(n)$ will be denoted as $Z(k)$. The main lobe of the spectrum occupied by $Z(k)$ overlaps with K subcarriers of $Y(k)$ (see e.g., Fig. 6.2 and Fig. 6.5). Hence, if the center frequency of $Z(k)$ is located at subcarrier κ, the subcarriers $k \in \left[\kappa - \frac{K}{2}, \kappa + \frac{K}{2} - 1 \right]$ will constitute the overlapping band (OB).

In time domain, NB symbols constitute structured information from a finite alphabet, while OFDMA signal behaves like random noise spread over multiple NB symbols. In frequency domain, on the other hand, OFDMA subcarriers carry structured information, and NB signal can be considered like random and colored noise covering multiple subcarriers. This is readily seen from the received signal, which can be denoted in time domain as

$$r(n) = \overbrace{z(n)}^{\mathrm{NB}} + \underbrace{\overbrace{\sum_{k=0}^{N-1} Y(k) e^{j2\pi kn/N}}^{\mathrm{OFDMA}}}_{y(n)} + w(n), \tag{6.7}$$

---

[4]Note that the symbol-spaced equivalent of any physical channel can be obtained by convolving the actual channel impulse response with the pulse shaping filter employed and taking symbol-spaced samples.

117

where $w(n)$ is the additive white Gaussian noise (AWGN) with a two sided power spectral density of $N_0/2$, and in frequency domain as

$$R(k) = \overbrace{Y(k)}^{\text{OFDMA}} + \underbrace{\frac{1}{N}\overbrace{\sum_{n=0}^{N-1} z(n)e^{-j2\pi kn/N}}^{\text{NB}}}_{Z(k)} + W(k), \tag{6.8}$$

where $W(k)$ is the frequency domain reciprocal $w(n)$.

6.2.3 Gaussian Approximation Based Symbol Error Rate

The symbol error rate of a system under the effect of co-channel interference can be estimated assuming that the interfering signal amplitude has a Gaussian distribution, which is known as Gaussian approximation. The SER for a system employing QPSK modulation and using the GA is given by [47]

$$P_{QPSK} = 2Q\left(\sqrt{\frac{E_b}{\frac{N_0}{2} + \sigma_I^2}}\right)\left[1 - \frac{1}{2}Q\left(\sqrt{\frac{E_b}{\frac{N_0}{2} + \sigma_I^2}}\right)\right], \tag{6.9}$$

where Q denotes the Q-function, E_b is the bit energy, and σ_I^2 is the interference variance, which is equal to P_{rx} of the interfering signal.

The GA is rather simple but it is typically not very accurate especially at high SNR values where the resulting SER tends to be optimistic. For the scenario at hand, based on (6.7) and (6.8), the interference is a sum of N random variables. Therefore, from the central limit theorem, this implies that GA for the specific scenario in consideration would be accurate (especially for large N). The accuracy of the GA is tested in a practical co-channel interference scenario by comparing it with actual simulation results in Section 6.6.

6.3 Joint Demodulation Method

A well-known and efficient method for handling co-channel signals is to demodulate them jointly utilizing maximum likelihood estimation [107, 108]. For the coexistence scenario in

118

consideration, ML estimation might be performed either in time domain or in frequency domain. However, time domain requires a smaller number of computations and it is more desirable to perform the ML estimation in time domain. This is due to the relationship between K and the number of NB symbols within the OFDMA symbol C, which can be written as $K = (1 + \alpha)C$, where α is usually greater than 0.

Denoting the estimates for the NB and OFDMA signals in time domain as $\hat{z}(n)$ and $\hat{y}(n)$, respectively, an ML estimate of both signals can be obtained as

$$
\begin{aligned}
\left[\hat{a}_m, \hat{X}(k)\right] &= \arg \min_{a_m, X(k)} \left\{ \left| r(mT) - z(mT) - y'(mT) \right|^2 \right\} \\
&= \arg \min_{a_m, X(k)} \left\{ \left| r(mT) - \sum_{l=0}^{L_{\mathrm{nb}}-1} h'(l) a_{m-l} - \sum_{k=\kappa-\frac{K}{2}}^{\kappa+\frac{K}{2}-1} Y(k) e^{j2\pi kmT/N} \right|^2 \right\}, \quad (6.10)
\end{aligned}
$$

where $y'(n)$ is the time domain reciprocal of $Y(k)$ for $k \in \left[\kappa - \frac{K}{2}, \kappa + \frac{K}{2} - 1\right]$.

The number of different values that $z(mT)$ and $y'(mT)$ can take should be limited in order for the joint demodulation algorithm to be computationally feasible. This condition is satisfied for both $z(mT)$ and $y'(mT)$ since the data sequences a_m and $X(k)$ each belong to a finite alphabet. There are M^K possibilities for the OFDMA signal in the overlapping band, and M possibilities for each of the C symbols in the NB signal, where M is the number of constellation points depending on the modulation order (e.g., $M = 4$ for QPSK). Therefore, the number of possibilities that need to be considered for each NB symbol is M^{K+1}.

Implementing (6.10) requires an exhaustive search through M^{K+1} possible combinations of $z(mT)$ and $y'(mT)$, which are obtained by applying the channel responses to all possible values of a_m and $X(k)$ to yield $z(mT)$ and $Y'(k)$, respectively, and also by computing the inverse DFT (IDFT) for all $Y'(k)$s to get $y'(mT)$s. This exhaustive search as well as the computations required for obtaining $z(mT)$ and $y'(mT)$s render the joint demodulation method prohibitively complex as it will be clearly demonstrated in Section 6.5.

119

6.4 Iterative CCI Cancellation Method

Considering the apparently high complexity of the ML estimation based joint demodulation method, we propose an efficient but low complexity alternative, which we call iterative CCI cancellation method. The iterative cancellation method solves the co-channel interference problem through enhancing both $Y(k)$ and $z(n)$ in a successive manner in multiple iterations. The iterations get started by obtaining and using an initial estimate of either $z(n)$ or $Y(k)$, which will be denoted as $\hat{z}(n)$ and $\hat{Y}(k)$, respectively.

An initial rough estimation for $z(n)$ can be obtained utilizing $Z(k)$ if the power of $Z(k)$ is high enough that it can be sensed over the OB through energy detection. The threshold of the energy detector is set according to the average signal-to-noise ratio (SNR) level over $k \notin \left[\kappa - \frac{K}{2}, \kappa + \frac{K}{2} - 1\right]$. In case the number of subcarriers whose energy exceeds the threshold is close to K, an initial estimate for the NB signal is obtained by taking the IDFT of the subcarriers $k \in \left[\kappa - \frac{K}{2}, \kappa + \frac{K}{2} - 1\right]$ to yield

$$\hat{z}(n) = \sum_{k=\kappa - \frac{K}{2}}^{\kappa + \frac{K}{2} - 1} R(k)e^{j2\pi kn/N}. \tag{6.11}$$

If the NB signal is too weak to provide a useful estimate, or if K is unknown, then, following an alternative approach, $R(k)$ is used as an initial estimate for $Y(k)$.

The main idea of the proposed method is to demodulate the estimated signal, $\hat{z}(n)$ or $\hat{Y}(k)$, and then to regenerate the signal waveform based on the symbol decisions made to obtain $\tilde{z}(n)$ or $\tilde{Y}(k)$. Note that $\tilde{z}(n)$ and $\tilde{Y}(k)$ are expected to be cleaner versions of $\hat{z}(n)$ and $\hat{Y}(k)$, respectively, since they are free of AWGN and supposedly less affected by CCI.

Since the initial estimate employed $\left(\hat{z}(n) \text{ or } \hat{Y}(k)\right)$ is corrupted by CCI and AWGN, the symbol decisions made may include errors. However, the effect of symbol errors made in $\hat{z}(n)$ is not localized in frequency domain; on the contrary, it is spread over K subcarriers. Similarly, a corrupted subcarrier in $\hat{Y}(k)$ has an impact that is spread over N samples in time domain. Hence, subtracting $\tilde{z}(n)$ with symbol errors from $r(n)$ does not necessarily

120
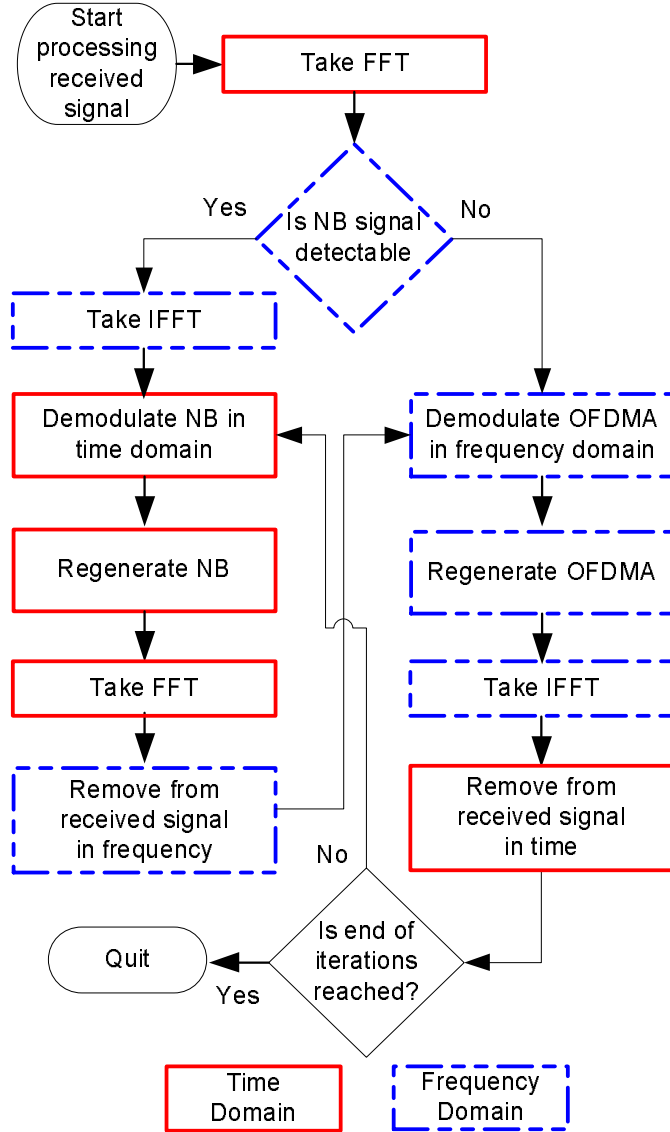
Figure 6.3 Flowchart of the proposed iterative CCI cancellation algorithm.

corrupt subcarriers of $\hat{Y}(k)$. The same is true when $\tilde{Y}(k)$ with some incorrectly demodulated subcarriers is removed from $R(k)$; it does not necessarily lead to a $\hat{z}(n)$ with symbol errors.

The flowchart provided in Fig. 6.3 illustrates the steps that need to be followed after obtaining the initial signal. The first step is demodulation. The internal stages for demodulation are shown for the NB system in a separate flowchart in Fig. 6.4. It starts with downconverting the signal to the baseband from the intermediate frequency (IF) of $f_c' - f_c$, where f_c and f_c' are the carrier frequencies of the OFDMA signal and the NB signal,

121

respectively. If the NB signal is a CDMA signal, this stage is followed by multiplication with the pseudo-noise (PN) sequence, which is shown with a dashed block in Fig. 6.4. The rest of demodulation is performed by applying channel equalization, downsampling, and making symbol decisions to obtain the IQ data. For the NB system, it is assumed that the carrier frequency f_c' is known, and a channel estimate $\hat{h}'(l)$ is available[5]. For the OFDMA system, downconversion and downsampling stages do not exist[6], and channel estimation is performed over pilot subcarriers to obtain $\hat{H}(k)$.

After obtaining the IQ data, regeneration (demonstrated for NB signal in Fig. 6.4) takes place. The steps that constitute regeneration are upsampling the IQ data, applying pulse shaping, (if the signal is a CDMA signal) multiplying the signal with the PN sequence, upconverting it, and convolving it with the baseband channel. Again, upsampling and upconversion are not performed for the OFDMA signal. The pulse shaping filter used by the NB system is assumed to be known. If the regenerated signal is $\tilde{z}(n)$, its DFT is taken, and the resulting signal $\tilde{Z}(k)$ is removed from $R(k)$ to obtain an estimate for the OFDMA signal, i.e.

$$\hat{Y}(k) = R(k) - \tilde{Z}(k) = R(k) - \frac{1}{N} \sum_{n=0}^{N-1} \tilde{z}(n) e^{-j2\pi kn/N}. \tag{6.12}$$

---

[5]The proposed algorithm's performance for an NB system with channel estimation errors is investigated through simulations in Section 6.6.

[6]The received signal $r(n)$ is already downconverted to the baseband based on the carrier frequency f_c of the OFDMA signal.
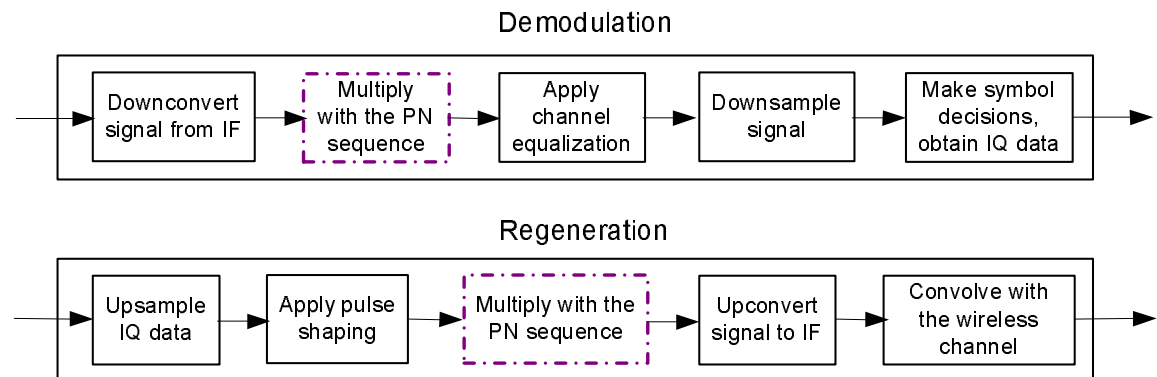
Demodulation

Regeneration

Figure 6.4 Flowchart of the demodulation and regeneration modules for the NB system.

If the regenerated signal is $\tilde{Y}(k)$, its IDFT is taken, and the resulting signal $\tilde{y}(n)$ is subtracted from $r(n)$ to obtain an estimate for the NB signal as follows

$$\hat{z}(n) = r(n) - \tilde{y}(n) = r(n) - \sum_{k=0}^{N-1} \tilde{Y}(k)e^{j2\pi kn/N}. \tag{6.13}$$

An important question that might be raised about the proposed method is why the entire OFDMA band is handled rather than dealing with the OB only, because processing the entire band has the following disadvantages:

- Since $\tilde{y}(n)$ is the IDFT of the entire OFDMA band rather than the OB only, any errors made in the demodulation of subcarriers $k \notin \left[\kappa - \frac{K}{2}, \kappa + \frac{K}{2} - 1\right]$ appear as additive noise in (6.13). It would be expected that this increases the number of NB demodulation errors, especially if K is small,

- The complexity of the algorithm becomes proportional to N rather than K (as it will be analyzed in Section 6.5).

The reasons why we do not deal with the OB only is that K may not always be known accurately, and also, subcarriers $k \notin \left[\kappa - \frac{K}{2}, \kappa + \frac{K}{2} - 1\right]$ might have been affected by the sidelobes of the NB signal. Moreover, through computer simulations, it is found that the extra noise caused by the demodulation errors outside the OB does not lead to a noticeable increase in the NB demodulation errors even for $\frac{K}{N}$ ratios as small as 2.5%.

6.5   Computational Complexity

Co-channel interference needs to be canceled in real-time by a mobile station or a base station that is affected by CCI. Therefore, the computational complexity of the cancellation algorithm employed is critical. This section aims to provide a comparison of complexities of the maximum likelihood and the proposed iterative interference cancellation algorithms in terms of the CPU cycle counts required by multiplication (MUL), addition (ADD), and comparison (CMP) operations.

123

6.5.1 ML Method

According to the information provided in Section 6.3, there are M^K possibilities for K interfered subcarriers in the OFDMA signal, and M possibilities for each of the C NB symbols. Applying the channel frequency response to the possible OFDMA symbols requires $M^K K$ complex MULs. Applying the channel impulse response to C NB symbols, on the other hand, requires MC convolutions, where each convolution is equivalent to L complex MULs and $L-1$ complex ADDs.

After appying the channel responses, all possible OFDMA signals need to be transfered from frequency domain into the time domain via M^K inverse fast Fourier transform (IFFT) operations of size N. Each IFFT operation requires $\frac{N}{2}\log_2 N$ complex MULs and $N\log_2 N$ complex ADDs. Adding the OFDMA and NB signals and subtracting their sum from the received signal requires $2M^{K+1}C$ complex ADDs. To obtain the absolute squared differences for all possibilities, $2M^{K+1}C$ MULs and $M^{K+1}C$ ADDs are performed. The minimum of the M^{K+1} absolute squared values obtained is found performing M^{K+1} CMPs for all C NB symbols.

Taking into account that a complex ADD is equivalent to 2 real ADDs, and a complex MUL is equal to 4 real MULs and 2 real ADDs, the computations required can be listed in terms of real MULs, real ADDs, and CMPs as in Table 6.1.

6.5.2 Iterative Cancellation

In the proposed iterative cancellation method, for a desired number of iterations $\mathcal{I}$, $2(1+\mathcal{I})$ FFT and IFFT operations need to be performed in total, each of which requires $\frac{N}{2}\log_2 N$ complex MULs and $N\log_2 N$ complex ADDs. To find whether the NB signal is detectable over the OB, the absolute squared values for K samples in frequency domain need to be calculated and compared with a threshold value. These two operations are performed via $2K$ MULs plus K ADDs, and K CMPs, respectively.

In each of the $\mathcal{I}$ iterations desired, to demodulate the OFDMA subcarriers, N complex MULs are needed for equalization and $N\log_2 M$ CMPs for making symbol decisions . For

124

the demodulation of NB symbols, if a maximum likelihood sequence estimation (MLSE) equalizer is employed, $4CLM^L$ MULs and $CM^L(4L-2)$ ADDs are needed (according to [109]), whereas a linear equalizer (LE) such as a zero-forcing equalizer (ZFE) or an MMSE equalizer would require CL complex MULs and $C(L-1)$ complex ADDs. Also, $C\log_2 M$ CMPs are necessary for making symbol decisions.

Again in each iteration, to regenerate the OFDMA subcarriers, N complex MULs are needed to apply the wireless channel effect. In NB symbols' regeneration, on the other hand, a convolution is required for applying the channel, which is equal to CL complex MULs and $C(L-1)$ complex ADDs, and another convolution for pulse shaping, which is equal to $2CN$ MULs and $2(C-1)N$ ADDs. Finally, in each iteration each of the subtractions from the received signal in time and in frequency require N complex ADDs. The computations required for each step of the iterative cancellation method are provided in the second part of Table 6.1.

125

Table 6.1 The computations required for maximum likelihood and iterative cancellation algorithms

	Operation	MUL	ADD	CMP
Maximum Likelihood	Applying Channel Responses	$4M^K K + 4MCL$	$2M^K K + 2MC(2L - 1)$	
	Taking IFFT	$2M^K N\log_2 N$	$3M^K N\log_2 N$	
	$r(n) - (\hat{z}(n) + \hat{y}(n))$		$4M^{K+1}C$	
	$|.|^2$	$2M^{K+1}C$	$M^{K+1}C$	
	$\min(|.|^2)$			$M^{K+1}C$
Iterative Cancellation	Taking FFT/IFFT	$4(1 + \mathcal{I})N\log_2 N$	$6(1 + \mathcal{I})N\log_2 N$	
	Energy Detection	$2K$	K	K
	OFDMA Equalization	$4\mathcal{I}N$	$2\mathcal{I}N$	
	NB Equalization (MLSE)	$4\mathcal{I}CLM^L$	$\mathcal{I}CM^L(4L - 2)$	
	NB Equalization (LE)	$4\mathcal{I}CL$	$2\mathcal{I}C(2L - 1)$	
	Symbol Decision			$\mathcal{I}(N + C)\log_2 M$
	Applying Channel Responses	$4\mathcal{I}N + 4\mathcal{I}CL$	$2\mathcal{I}N + 2\mathcal{I}C(2L - 1)$	
	Pulse Shaping	$2\mathcal{I}CN$	$2\mathcal{I}(C - 1)N$	
	$r(n) - \tilde{y}(n)$ & $R(k) - \tilde{Z}(k)$		$4\mathcal{I}N$	

126

Table 6.2 CPU cycle counts obtained using a XilinX DSP48 slice

N	K	C	L	M	$\mathcal{I}$	ML	Iter. I	Iter. II
512	40	32	4	4	3	5.3×10^{28}	2.3×10^{6}	7.9×10^{5}
512	20	16	4	4	3	4.7×10^{16}	1.3×10^{6}	5.8×10^{5}
512	10	8	4	4	3	4.4×10^{10}	8.6×10^{5}	4.8×10^{5}
512	40	32	4	16	3	7.0×10^{52}	3.9×10^{8}	7.9×10^{5}
512	40	32	4	4	5	5.3×10^{28}	3.8×10^{6}	1.3×10^{6}
512	40	32	1	4	3	5.3×10^{28}	7.8×10^{5}	7.8×10^{5}
1024	40	32	4	4	3	1.1×10^{29}	3.2×10^{6}	1.6×10^{6}

6.5.3 Comparison of Complexities

A numerical comparison of complexities of the two algorithms in terms of CPU cycle counts can be obtained considering that the cycle numbers for ADD, MUL, and CMP operations, in a Xilinx DSP48 slice for instance, are 1, 3, and 1, respectively [32]. The CPU cycle counts determined for both algorithms employing various sets of system parameters are demonstrated in Table 6.2, where Iter. I stands for the iterative cancellation method employing an MLSE equalizer for the NB system, and Iter. II is the iterative method employing an LE.

In Table 6.2, it is observed that there is a drastic difference between the cycle numbers required for ML and Iter. I algorithms. This is caused by the fact that every step of the ML estimation has an exponential complexity, whereas Iter. I has a linear complexity except for the MLSE equalizer that it employs. Cycle counts for Iter. II algorithm show that the complexity of the iterative cancellation can be decreased further by employing a linear equalizer, especially when M or L is large.

It is seen that parameter K (and C, which depends on K) acts exponentially on the complexity of ML estimation and linearly on the iterative cancellation. M affects ML estimation and Iter. I exponentially, whereas it has a negligible effect on Iter. II. N has a linear effect on all algorithms, and $\mathcal{I}$ has a linear effect on the iterative ones. L has a relatively weak impact on ML estimation and Iter. II, whereas it affects Iter. I exponentially.

127
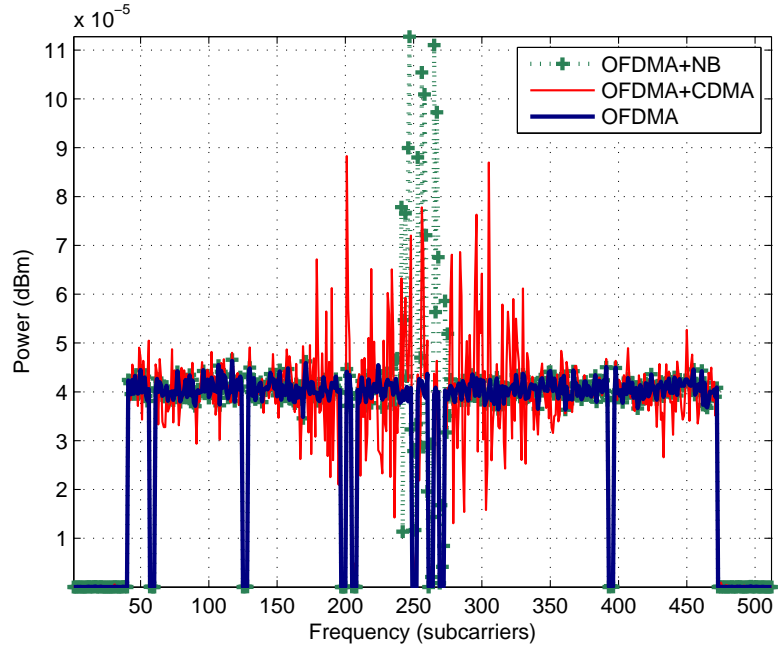
Figure 6.5 The spectra of the received co-channel signals and the OFDMA signal alone (OFDMA SNR: 30 dB, NB SNR: 20 dB). CDMA spectrum is wider than the NB spectrum due to multiplication with the PN sequence.

6.6 Simulations

6.6.1 Simulation Parameters

Computer simulations are done to determine the performance of the proposed iterative canceler in different scenarios as well as to compare it with the joint demodulation method's performance. The parameters of the OFDMA, NB, and CDMA systems employed in the simulations are presented in Table 6.3. The OFDMA symbol occupies 400 subcarriers out of 512 available ones due to the guard bands and empty subcarriers. The overlapping band, which is located in the middle of the OFDMA spectrum, is approximately 40 subcarriers wide for the NB signal, and 128 subcarriers wide for the uplink CDMA signal (illustrated in Fig. 6.5).

The SER performances of OFDMA, NB, and CDMA systems are investigated both in AWGN (Figs. 6.6-6.9) and multipath (MP) (Figs. 6.10-6.13) channels. In MP simulations, availability of a perfect channel estimation is assumed for NB and CDMA, and an efficient

128

MLSE equalizer is utilized. For OFDMA, on the other hand, pilot based practical channel estimation and equalization are performed. In all simulations, while the desired signal power is varied over a certain range, noise power is fixed, and interference SNR is kept constant. Signal-to-interference-plus-noise ratio (SINR) is defined as the ratio of the desired signal power to the sum of interference and noise power over the overlapping band.

In Figs. 6.6-6.13, the uppermost curve shows the performance obtained without applying CCI cancellation (referred as "without cancellation"), whereas the lowest curve shows the performance when CCI does not exist (referred as "No CCI"). The three curves in between demonstrate the SER performances after each iteration[7]. The SINR values on the x-axis apply only to the without cancellation curve. As a last note, the no CCI curve is actually an SER vs. SNR curve shifted leftwards by the amount of interference SNR, which is 30 dB in Fig. 6.6 and Fig. 6.10; 25 dB in Fig. 6.7 and Fig. 6.11; 20 dB in Fig. 6.8 and Fig. 6.12; and 15 dB in Fig. 6.9 and Fig. 6.13.

6.6.2 AWGN Channel Results

Fig. 6.6 shows the SER performance of the OFDMA system interfered by an NB system. At very low SINR levels, since the interfering signal can be detected accurately, the gain with respect to without cancellation can be as large as 25 dB after the 3rd iteration. As SINR approaches 0 dB, however, it becomes challenging to separate the two signals from each other, and the gain drops to around 6 dB. Beyond 10 dB SINR, the SER curve of the

---

[7]In Fig. 6.12, the first two iterations are omitted, and the performance curves obtained for two different channel estimation error levels are displayed instead.

Table 6.3 OFDMA, narrowband, and CDMA system parameters

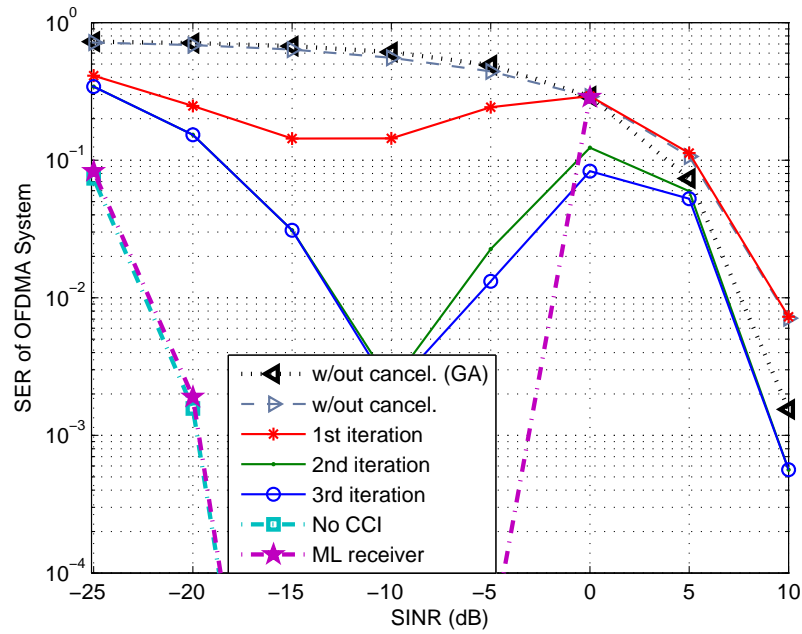| Parameter	OFDMA	Narrowband	CDMA
Bandwidth	5 MHz	370 kHz	625 kHz
Samples per symbol	512	16	32
Modulation	QPSK	QPSK	QPSK
MP channel model	Veh. A	Out.-to-in. A	Out.-to-in. A
Pulse shape	Rectang.	Raised cos. (α=0.3)	Raised cos. (α=0.3)

129

Figure 6.6 SER performance of the OFDMA system under the influence of NB interference (AWGN channel).
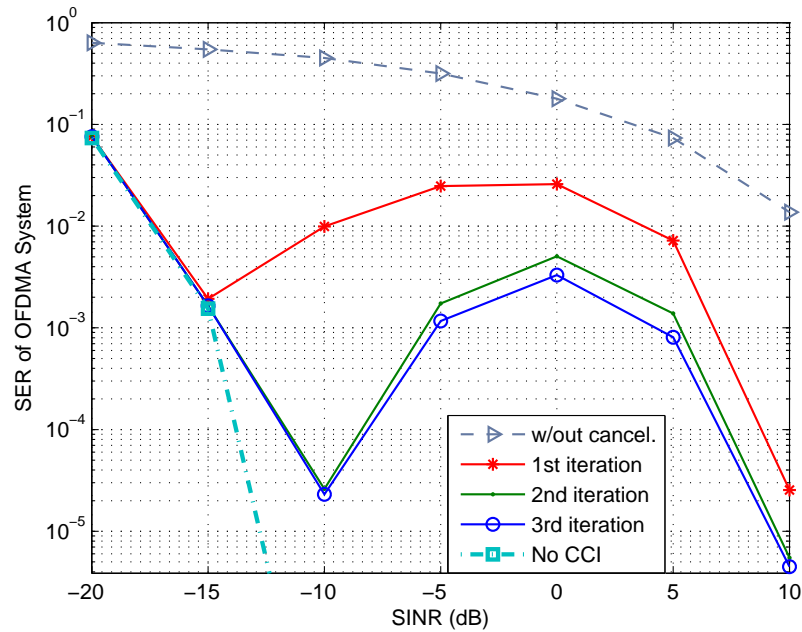
Figure 6.7 SER performance of the OFDMA system under the influence of CDMA interference (AWGN channel).

proposed method approaches to the without cancellation curve. This is reasonable because when the interference is too weak relative to the desired signal, interference cancellation is not expected to yield a high gain. It is worth to note that while there is a considerable gain difference between the first two iterations, the extra gain yielded by the third iteration is not that significant.

Fig. 6.6 also shows the theoretical performance curve that is obtained by using the GA for the co-channel interference. It is observed that the GA yields quite accurate values up until 0 dB SINR, after where it yields optimistic SERs. Another performance curve that is displayed in Fig. 6.6 belongs to the maximum likelihood receiver, whose SER is as low as the "No CCI" case at low SINR values. The ML receiver is superior to the iterative canceler everywhere except around 0 dB SINR.

In case of CDMA interference, the gains obtained for the OFDMA system, which are displayed in Fig. 6.7, are considerably larger than the previous case. The reason for this performance difference is the involvement of the PN sequence, which introduces additional signal separability. The fact that the CDMA signal power is spread over a wider frequency band (compared to the NB signal) makes the OFDMA signal more accurately detectable. Once the cancellation process starts with a reliable estimate for the OFDMA signal, the following iterations become more successful, as well.

The NB system performance improvement enabled by the proposed method is shown in Fig. 6.8. For SINR values smaller than 0 dB, the gain with respect to no CCI cancellation can be as high as 18 dB. For SINR greater than 0 dB, there is still a gain around 3 dB. Fig. 6.8 also shows the ML receiver performance. ML receiver is superior to the iterative canceler in general. However, at around 0 dB SINR, it yields apparently higher SER than the iterative canceler.

The improvement of the CDMA performance is again more significant as it can be seen in Fig. 6.9. The SER values are much closer to the no CCI curve at low SINR values, and there is a 10 dB gain even at rather high SINR.
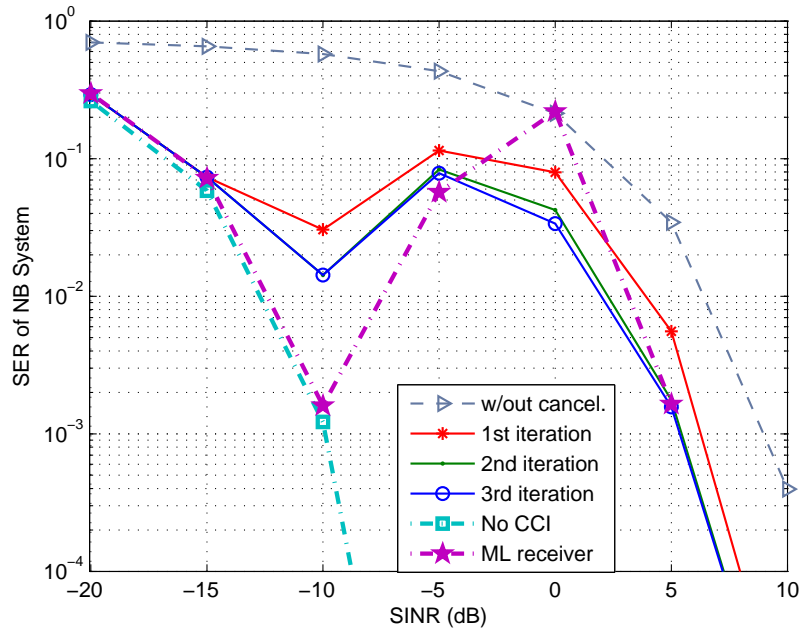
131

Figure 6.8 SER performance of the NB system under the influence of OFDMA interference (AWGN channel).
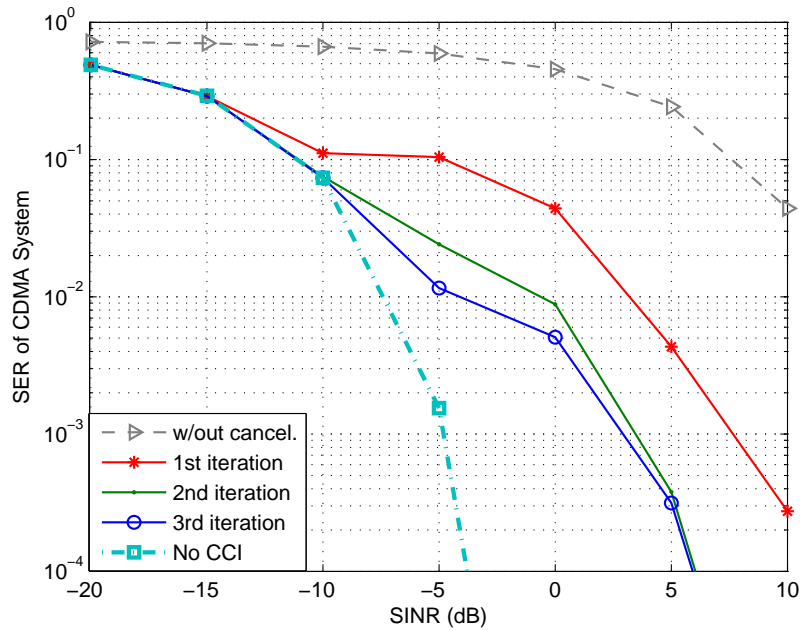
Figure 6.9 SER performance of the CDMA system under the influence of OFDMA interference (AWGN channel).

132

6.6.3 Multipath Channel Results

In MP simulation results in Figs. 6.10-6.13, the margin between without cancellation and no CCI curves is not as wide as in the AWGN case. Nevertheless, the proposed algorithm is still able to provide considerable gains. For the OFDMA system interfered by the NB signal (see Fig. 6.10), the gain is above 15 dB up until 0 dB SINR, after which it decreases towards 5 dB again. When the interferer is CDMA (see Fig. 6.11), on the other hand, the gains are considerably higher, and the performance curve approaches the no CCI case.

Improvement of the NB performance is shown in Fig. 6.12. The gain obtained for SINR smaller than 0 dB is more than 12 dB. Approaching 0 dB SINR, this gain becomes smaller, but even at 10 dB SINR there is still a gain of approximately 5 dB. Impact of NB channel estimation error on the performance of iterative cancellation is also demonstrated in Fig. 6.12. The variance of the Gaussian noise added to each channel tap estimate is set as a certain ratio of the power of that tap. The two ratios examined are 5% and 10%. It is observed that the cancellation gain decreases with increasing channel estimation error. Still, it can be stated that channel estimation errors, which are likely to occur under CCI effect, do not have a very strong influence at error levels as large as 5%.

The CDMA performance improvement (see Fig. 6.13) is more critical. The performance is almost as good as no CCI case up until 0 dB SINR, after where it starts to decrease. The difference between the NB and CDMA curves' behavior is again due to the use of a PN sequence.

6.6.4 Effect of Overlapping Bandwidth

The width of the OB has a considerable effect on the cancellation performance of the proposed iterative method. This effect is investigated in terms of SER values of the OFDMA system in Fig. 6.14, where the overlapping bandwidths are expressed as their ratio to the OFDMA signal bandwidth. The performance curves that are obtained for various overlap percentages clearly indicate that increasing overlap leads to a more successful cancellation. This is because, for a given SINR value, the energy of the NB signal changes linearly

133
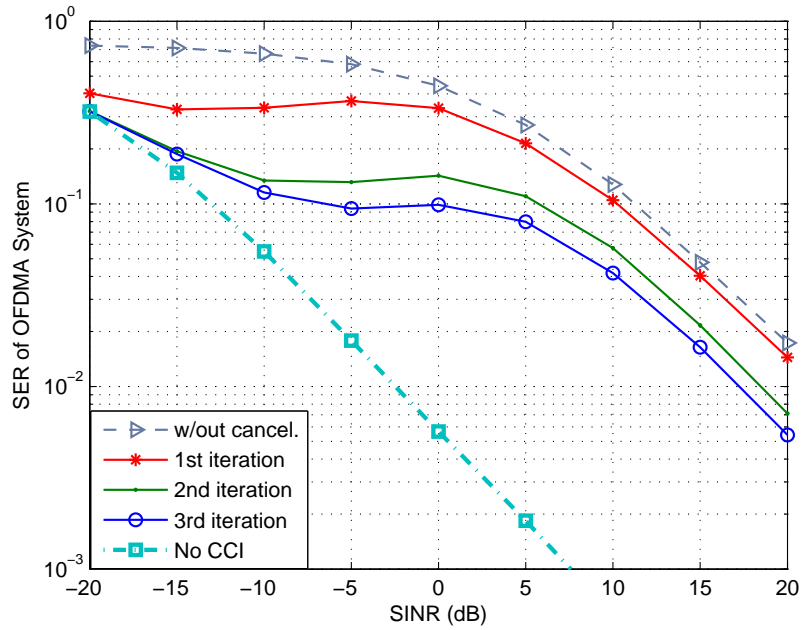
Figure 6.10 SER performance of the OFDMA system under the influence of NB interference (MP channel).
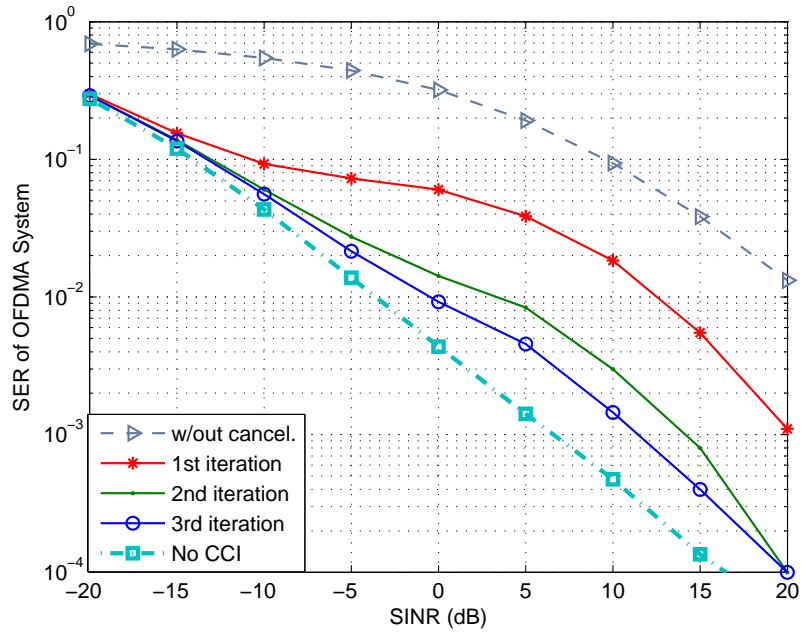
Figure 6.11 SER performance of the OFDMA system under the influence of CDMA interference (MP channel).

134
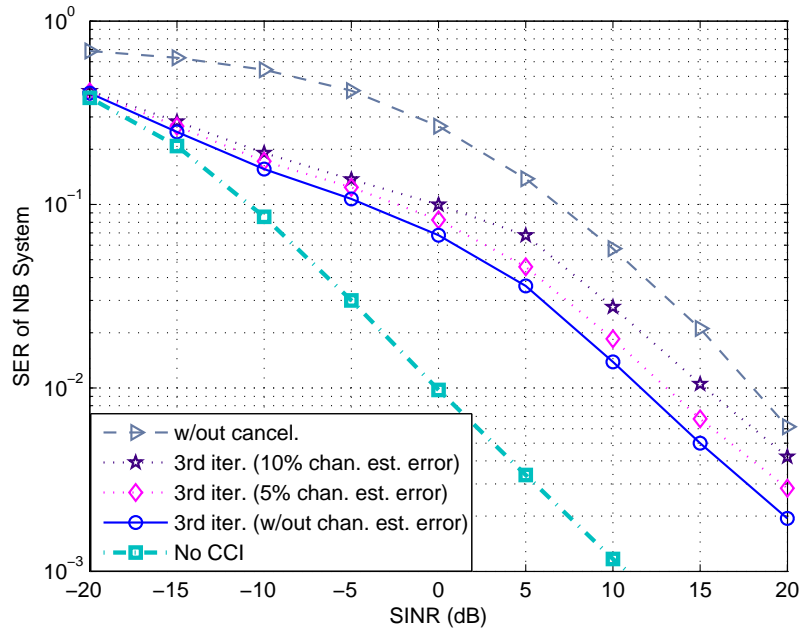
Figure 6.12 SER performance of the NB system under the influence of OFDMA interference (MP channel).
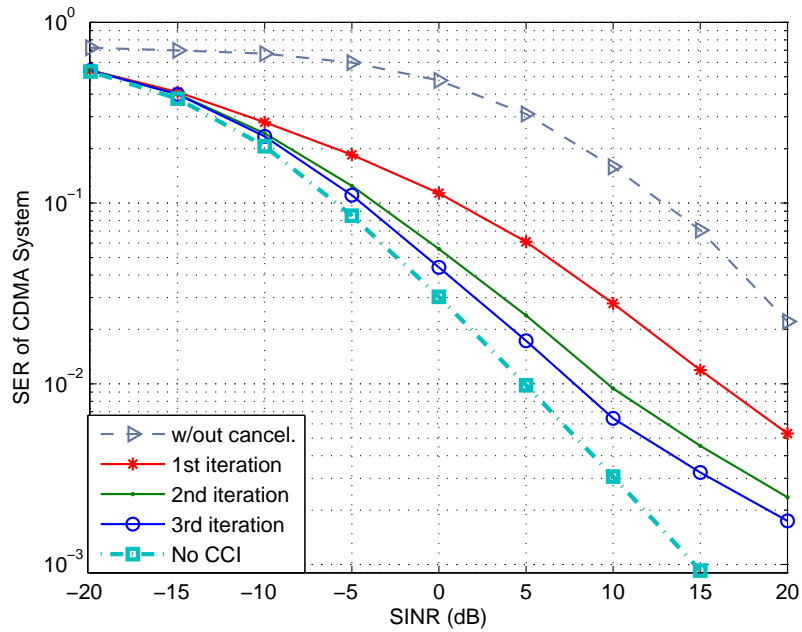
Figure 6.13 SER performance of the CDMA system under the influence of OFDMA interference (MP channel).

135
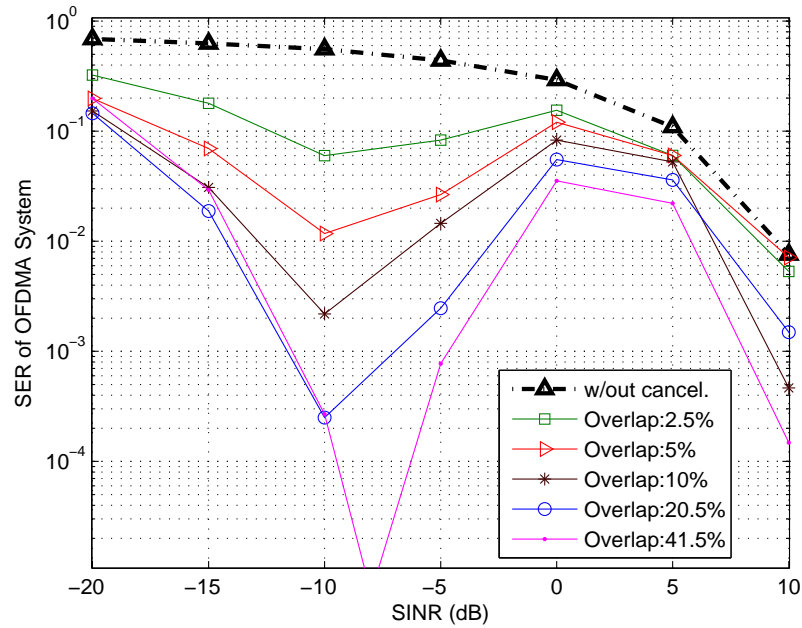
Figure 6.14 OFDMA system's SER performance under the influence of NB interference for various overlapping bandwidths (AWGN channel).

depending on its bandwidth, i.e. the NB signal in a widest overlap scenario is the strongest one. Increased NB signal energy leads to a more successful demodulation of the NB symbols, which in turn boosts the overall performance of the algorithm.

6.7 Concluding Remarks

In this chapter, an iterative CCI canceler is proposed that mitigates the NB interference in multicarrier spectrum as well as the effect of MC signal on NB symbols. Application scenarios are provided where the proposed canceler might be very attractive such as the coexistence of CDMA and OFDMA based systems during the migration from 3G to 4G wireless technologies. It is shown that processing the whole MC band rather than only the overlapping band is more advantageous in spite of the increased complexity. Moreover, it is numerically demonstrated that the proposed method is significantly less complex compared to joint demodulation. In the simulations, fundamental gains are obtained for both co-channel signals in terms of SER performance validating the claimed efficiency of the

136

proposed method. Also, the effect of NB channel estimation errors on the available gains is quantified. Finally, it is found that larger gains are possible when the overlap between the NB and MC signals is larger.

CHAPTER 7

CONCLUSION AND FUTURE WORK

In this dissertation, next generation orthogonal frequency division multiple access (OFDMA) based co-channel systems are considered. For various scenarios, where two systems' signals might be co-channel on purpose or in an unintentional manner, baseband receiver algorithms are developed that aim at avoiding and cancelling co-channel interference. Co-channel systems in which 4G femtocells are involved are considered as a case study in most of the algorithms proposed. Certain parts of the work presented in this dissertation appeared in or are submitted to internationally recognized publications [5–13]. In the remainder of this section, first, the specific contributions of each chapter are summarized and then the possible future work is discussed.

7.1 List of Specific Contributions

- Analysis of the opportunity detection performance in UL OFDMA with timing misalignments

  We analyzed the opportunity detection performances of energy detection and ESPRIT (estimation of signal parameters by rotational invariance techniques) algorithms in the presence of timing misalignments in uplink OFDMA. For the energy detector, the statistics of subcarrier power are derived considering timing misalignments, and they are verified through computer simulations. Using these statistics, which take inter-carrier-interference (ICI) effects into account, receiver operating characteristics (ROCs) of the energy detector receiver are obtained. It is shown that energy detection

138

has a considerably better performance than ESPRIT, especially when the subcarrier assignment changes frequently.

- Estimation the optimum UL-OFDMA synchronization point that minimizes the ICI

  A closed form expression is obtained for the optimum UL-OFDMA synchronization point that minimizes the interference on the cognitive radio. It is shown that it may be at a later point than the arrival time of the earliest primary user's signal.

- Development of a co-channel framework for the coexistence of OFDMA based macro-cell and femtocells

  A co-channel framework is developed, which is based on utilizing the resource blocks of macrocell-associated mobile stations (mMSs) that are far away to a femtocell base station (fBS), therefore avoiding strong interference that may occur between a femtocell and close-by mMSs. An avoidance method that jointly utilizes the spectrum sensing results as well as scheduling information obtained from the macrocell base station (mBS) is introduced.

- Semi-blind user separation

  We proposed semi-blind user separation algorithm, which estimates the carrier frequency offsets and time delays of each block by exploiting the cross-correlations over pilot subcarriers. A two-dimensional clustering method is then employed to group the estimates, where each group belongs to a different user.

- Reception of MIMO-OFDMA signals using a single receiver

  A maximum likelihood estimation based method is devised, which takes MIMO receivers one step further and introduces reception of MIMO signals with a single receiver. The proposed method relaxes the hardware requirement while demanding higher digital signal processing power.

- Iterative Interference Cancellation for Co-Channel Multicarrier and Narrowband Systems

139

We proposed an efficient CCI cancellation method that may be utilized for improved coexistence of NB and multicarrier technologies. The method treats both co-channel signals as desired signals and enhances them in an iterative manner. In every iteration, the signals are demodulated, regenerated, and subtracted from the received signal successively in order to obtain a better estimate of the other co-channel signal.

7.2   Final Comments and Future Work

Co-channel systems are a promising approach to increasing wireless systems' capacity without requiring increased bandwidth. In this work, we considered the coexistence of next generation wireless systems and proposed a number of algorithms that target handling the potential co-channel interference that will occur. We believe that the algorithms that we developed, for which we did patent applications, as well, might be of considerable importance for the designers of wireless systems in the near future.

An important related research problem that we did not try to find a solution for in this dissertation is the co-channel interference that occurs in the coexistence of two OFDMA systems with the same parameters. Assuming that the signals of these systems overlap in all domains that can be readily imagined such as time, frequency, code, space, and power domains, there is need for some means that will provide signal separability. This might be a new domain or a computationally very demanding digital signal processing technique. In depth research for an element that will lead to signal separability in this kind of a co-channel scenario can lead to another PhD dissertation.

REFERENCES

[1] V. Chandrasekhar, J. G. Andrews, and A. Gatherer, "Femtocell networks: a survey," *IEEE Commun. Mag.*, vol. 46, no. 9, pp. 59–67, Sep. 2008.

[2] S. P. Yeh, S. Talwar, S. C. Lee, and H. Kim;, "WiMAX femtocells: a perspective on network architecture, capacity, and coverage," *IEEE Commun. Mag.*, vol. 46, no. 10, pp. 58–65, Oct. 2008.

[3] H. Claussen, L. Ho, and L. Samuel, "An overview of the femtocell concept," *Bell Labs Tech. J.*, vol. 13, no. 1, pp. 221–245, 2008.

[4] H. Arslan and K. Molnar, "Cochannel interference suppression with successive cancellation in narrow-band systems," *IEEE Commun. Lett.*, vol. 5, no. 2, pp. 37–39, 2001.

[5] M. E. Sahin, I. Guvenc, M. R. Jeong, and H. Arslan, "Opportunity detection for OFDMA systems with timing misalignment," in *Proc. IEEE Global Telecommun. Conf. (GLOBECOM)*, New Orleans, LA, Nov. 2008, pp. 1–6.

[6] M. E. Sahin, I. Guvenc, and H. Arslan, "Opportunity Detection for OFDMA-Based Cognitive Radio Systems with Timing Misalignment," *IEEE Trans. Wireless Commun.*, 2009, to appear.

[7] M. E. Sahin, I. Guvenc, M.-R. Jeong, and H. Arslan, "Handling CCI and ICI in OFDMA Femtocell Networks Through Frequency Scheduling," *IEEE Trans. Consum. Electron.*, 2009, submitted.

[8] M. E. Sahin, I. Guvenc, M. R. Jeong, and H. Arslan, "User separation for OFDMA uplink," in *IEEE Vehic. Technol. Conf. (VTC)*, Barcelona, Spain, Apr. 2009, pp. 1–5.

[9] M. E. Sahin, I. Guvenc, and H. Arslan, "Uplink User Signal Separation for OFDMA-Based Cognitive Radios," *EURASIP J. on Advances in Signal Proc.*, 2009, to appear.

[10] M. Sahin and H. Arslan, "MIMO-OFDMA Measurements; Reception, Testing, and Evaluation of WiMAX MIMO Signals With a Single Channel Receiver," *IEEE Trans. Instr. Meas.*, vol. 58, no. 3, pp. 713–721, Mar. 2009.

[11] M. E. Sahin, H. Arslan, and D. Singh, "Reception and Measurement of MIMO-OFDM Signals with a Single Receiver," in *IEEE Vehic. Technol. Conf. (VTC)*, Baltimore, MD, Oct. 2007, pp. 666–670.

[12] M. E. Sahin, I. Guvenc, and H. Arslan, "An Iterative Interference Cancellation Method for Co-Channel Multicarrier and Narrowband Systems," *Elsevier Phy. Commun.*, 2009, submitted.

[13] ——, "Iterative Interference Cancellation for Co-Channel Multicarrier and Narrowband Systems," in *Proc. IEEE Wireless Commun. and Network. Conf. (WCNC)*, 2010, submitted.

[14] S. Haykin, "Cognitive radio: brain-empowered wireless communications," *IEEE J. Sel. Areas Commun. (JSAC)*, vol. 23, no. 2, pp. 201–220, 2005.

[15] G. Ganesan and Y. G. Li, "Cooperative spectrum sensing in cognitive radio, part I: Two user networks," *IEEE Trans. Wireless Commun.*, vol. 6, no. 6, pp. 2204–2213, June 2007.

[16] ——, "Cooperative spectrum sensing in cognitive radio, part II: Multiuser networks," *IEEE Trans. Wireless Commun.*, vol. 6, no. 6, pp. 2214–2222, June 2007.

[17] S. Mangold, Z. Zhong, K. Challapali, and C.-T. Chou, "Spectrum agile radio: radio resource measurements for opportunistic spectrum usage," in *Proc. IEEE Global Telecommun. Conf. (GLOBECOM)*, vol. 6, Dallas, TX, Nov. 2004, pp. 3467–3471.

[18] J. Hillenbrand, T. A. Weiss, and F. K. Jondral, "Calculation of detection and false alarm probabilities in spectrum pooling systems," *IEEE Commun. Lett.*, vol. 9, no. 4, pp. 349–351, Apr. 2005.

[19] Y. C. Liang, Y. Zeng, E. C. Y. Peh, and A. T. Hoang, "Sensing-throughput tradeoff for cognitive radio networks," *IEEE Trans. Wireless Commun.*, vol. 7, no. 4, pp. 1326–1337, Apr. 2008.

[20] S.-Y. Tu, K.-C. Chen, and R. Prasad, "Spectrum sensing of OFDMA systems for cognitive radios," in *Proc. IEEE Int. Symp. Personal, Indoor and Mobile Radio Commun. (PIMRC)*, Athens, Greece, Sep. 2007, pp. 1–5.

[21] N. Khambekar, L. Dong, and V. Chaudhary, "Utilizing OFDM guard interval for spectrum sensing," in *Proc. IEEE Int. Symp. Personal, Indoor and Mobile Radio Commun. (PIMRC)*, Athens, Greece, Sep. 2007, pp. 1–5.

[22] T. Yucek and H. Arslan, "OFDM signal identification and transmission parameter estimation for cognitive radio applications," in *Proc. IEEE Global Telecommun. Conf. (GLOBECOM)*, Washington, DC, Nov. 2007, pp. 4056–4060.

[23] J. Ma and Y. G. Li, "Soft combination and detection for cooperative spectrum sensing in cognitive radio networks," in *Proc. IEEE Global Telecommun. Conf. (GLOBECOM)*, Washington, DC, Nov. 2007, pp. 3139–3143.

[24] J.-H. Baek, H.-J. Oh, and S.-H. Hwang, "Improved reliability of spectrum sensing using energy detector in cognitive radio system," in *Proc. Int. Conf. Adv. Commun. Technol. (ICACT)*, vol. 1, Gangwon-Do, Korea, Feb. 2008, pp. 575–578.

142

[25] M. El-Tanany, Y. Wu, and L. Hazy, "OFDM uplink for interactive broadband wireless: Analysis and simulation in the presence of carrier, clock, and timing errors," *IEEE Trans. Broadcast*, vol. 47, no. 1, pp. 3–19, Mar. 2001.

[26] M. Park, K. Ko, H. Yoo, and D. Hong, "Performance analysis of OFDMA uplink systems with symbol timing misalignment," *IEEE Commun. Lett.*, vol. 7, no. 8, pp. 376–378, Aug. 2003.

[27] E. Bala and L. J. Cimini, "On the uplink synchronization of OFDMA systems," in *Proc. IEEE Military Commun. Conf. (MILCOM)*, Atlantic City, NJ, Oct. 2005, pp. 1133–1139.

[28] L. T. W. Ho and H. Claussen, "Effects of user-deployed, co-channel femtocells on the call drop probability in a residential scenario," in *Proc. IEEE Int. Symp. Personal, Indoor and Mobile Radio Commun. (PIMRC)*, Athens, Greece, Sep. 2007, pp. 1–5.

[29] H. Claussen, "Performance of macro- and co-channel femtocells in a hierarchical cell structure," in *Proc. IEEE Int. Symp. Personal, Indoor and Mobile Radio Commun. (PIMRC)*, Athens, Greece, Sep. 2007, pp. 1–5.

[30] V. Chandrasekhar and J. G. Andrews, "Uplink capacity and interference avoidance for two-tier cellular networks," in *Proc. IEEE Global Telecommun. Conf. (GLOBECOM)*, Washington, DC, Nov. 2007, pp. 3322–3326.

[31] V. Chandrasekhar, J. Andrews, and A. Gatherer, "Femtocell networks: a survey," *IEEE Commun. Mag.*, vol. 46, no. 9, pp. 59–67, Sep. 2008.

[32] H. Mahmoud, H. Arslan, and M. Ozdemir, "Initial Ranging for WiMAX (802.16e) OFDMA," in *Proc. IEEE Military Commun. Conf. (MILCOM)*, Washington, DC, Oct. 2006, pp. 1–7.

[33] Y. Choi, S. Park, and S. Bahk, "Multichannel random access in OFDMA wireless networks," *IEEE J. Sel. Areas Commun. (JSAC)*, vol. 24, no. 3, pp. 603–613, 2006.

[34] I. Guvenc, "Statistics of macrocell-synchronous femtocell-asynchronous users' delays for improved femtocell uplink receiver design," *IEEE Commun. Lett.*, vol. 13, no. 4, pp. 239–241, Apr. 2009.

[35] J. V. Beek, P. O. Borjesson, M. L. Boucheret, D. Landstrom, J. M. Arenas, P. Odling, C. Ostberg, M. Wahlqvist, and S. K. Wilson, "A time and frequency synchronization scheme for multiuser OFDM," *IEEE J. Sel. Areas Commun. (JSAC)*, vol. 17, no. 11, pp. 1900–1914, Nov. 1999.

[36] M. Morelli, "Timing and frequency synchronization for the uplink of an OFDMA system," *IEEE Trans. Commun.*, vol. 52, no. 2, pp. 296–306, Feb. 2004.

[37] R. Roy and T. Kailath, "ESPRIT-estimation of signal parameters via rotational invariance techniques," *IEEE Trans. Acoust., Speech, and Signal Process.*, vol. 37, no. 7, pp. 984–995, Jul. 1989.

143

[38] B. Ottersten, M. Viberg, and T. Kailath, "Performance analysis of the total least squares ESPRIT algorithm," *IEEE Trans. Signal Process.*, vol. 39, no. 5, pp. 1122–1135, May 1991.

[39] B. Yang, K. Letaief, R. Cheng, and Z. Cao, "Channel estimation for OFDM transmission in multipath fading channels based on parametric channel modeling," *IEEE Trans. Commun.*, vol. 49, no. 3, pp. 467–479, Mar. 2001.

[40] R. Roy, A. Paulraj, and T. Kailath, "ESPRIT– A subspace rotation approach to estimation of parameters of cisoids in noise," *IEEE Trans. Acoust., Speech, and Signal Process.*, vol. 34, no. 5, pp. 1340–1342, Oct. 1986.

[41] U. Tureli, H. Liu, and M. Zoltowski, "OFDM blind carrier offset estimation: ESPRIT," *IEEE Trans. Commun.*, vol. 48, no. 9, pp. 1459–1461, Sep. 2000.

[42] T. Yucek, "Channel, Spectrum, and Waveform Awareness in OFDM-Based Cognitive Radio Systems," Ph.D. dissertation, University of South Florida, 2007.

[43] M. Wax and T. Kailath, "Detection of signals by information theoretic criteria," *IEEE Trans. Acoust., Speech, and Signal Process.*, vol. 33, no. 2, pp. 387–392, 1985.

[44] "3rd generation partnership project; technical specification group radio access network; evolved universal terrestrial radio access (E-UTRA); physical channels and modulation (release 8)," 3GPP, 3GPP TS 36.211, April 2008.

[45] "IEEE standard for local and metropolitan area networks. part 16: Air interface for fixed broadband wireless access systems," IEEE Std 802.16-2004, Oct. 2004.

[46] "IEEE standard for local and metropolitan area networks. part 16: Air interface for fixed and mobile broadband wireless access systems; amendment 2: Physical and medium access control layers for combined fixed and mobile operation in licensed bands," IEEE Std 802.16e-2005, Dec. 2005.

[47] J. G. Proakis, *Digital Communications*, 4th ed.   New York: McGraw-Hill, 2001.

[48] M. Rumney, "IMT-Advanced: 4G Wireless Takes Shape in an Olympic Year," White Paper, Sep. 2008. [Online]. Available: http://cp.literature.agilent.com/litweb/pdf/5989-9793EN.pdf

[49] J. Choi, D. Shin, and D. Shin, "Research and implementation of the context-aware middleware for controlling home appliances," *IEEE Trans. Consum. Electron.*, vol. 51, no. 1, pp. 301–306, 2005.

[50] FemtoForum, "Femtocell applications." [Online]. Available: http://femtoforum.org/femto/applications.php

[51] "3rd Generation Partnership Project; Technical Specification Group Radio Access Networks; 3G Home NodeB Study Item Technical Report (Release 8)," 3GPP, 3GPP TR 25.820, March 2008.

[52] FemtoForum, "Interference management in UMTS femtocells," White Paper, Dec. 2008. [Online]. Available: http://www.femtoforum.org/femto/Files/File/InterferenceManagementinUMTSFemtocells.pdf

[53] Orange, Telecom-Italia, T-Mobile, and Vodafone, "Requirements for LTE Home eNodeBs," 3GPP Document R4-070209, Lemesos, Cyprus, Mar. 2007.

[54] Vodafone-Group, "Home eNodeB considerations for LTE," 3GPP Document R4-070456, Sophia Antipolis, France, Apr. 2007.

[55] F. S. Chu and K. C. Chen, "Radio resource allocation in OFDMA cognitive radio systems," in *Proc. IEEE Int. Symp. Personal, Indoor and Mobile Radio Commun. (PIMRC)*, Athens, Greece, Sep. 2007, pp. 1–5.

[56] T. H. Kim and T. J. Lee, "Spectrum allocation algorithms for uplink sub-carriers in OFDMA-based cognitive radio networks," in *Proc. IEEE Int. Conf. on Innovations in Information Technol.*, Nashville, TN, Nov. 2007, pp. 51–54.

[57] D. L. Perez, A. Valcarce, G. D. L. Roche, E. Liu, and J. Zhang;, "Access methods to WiMAX femtocells: A downlink system-level case study," in *Proc. IEEE Int. Conf. Commun. Syst. (ICCS)*, Guangzhou, China, Nov. 2008, pp. 1657–1662.

[58] D. L. Perez, G. D. L. Roche, A. Valcarce, A. Juttner, and J. Zhang;, "Interference avoidance and dynamic frequency planning for WiMAX femtocells networks," in *Proc. IEEE Int. Conf. Commun. Syst. (ICCS)*, Guangzhou, China, Nov. 2008, pp. 1579–1584.

[59] S. Chen and T. Yao, "Intercarrier interference suppression and channel estimation for OFDM systems in time-varying frequency-selective fading channels," *IEEE Trans. Consum. Electron.*, vol. 50, no. 2, pp. 429–435, 2004.

[60] H. Yoshino and A. Czylwik, "Adaptive co-channel interference (CCI) cancellation for OFDM communication systems," in *Proc. Internat. Zurich Seminar Broadband Commun.*, 2000, pp. 245–250.

[61] S. Mangold, Z. Zhong, G. Hiertz, and B. Walke, "IEEE 802.11 e/802.11 k wireless LAN: Spectrum awareness for distributed resource sharing," *Wireless Commun. and Mobile Computing*, vol. 4, no. 8, Dec. 2004.

[62] N. Shankar, C. Cordeiro, and K. Challapali, "Spectrum agile radios: utilization and sensing architectures," in *IEEE Symp. New Frontiers Dyn. Spectrum Access Netw. (DySPAN)*, Nov. 2005, pp. 160–169.

[63] S. Haykin, "Cognitive radio: brain-empowered wireless communications," *IEEE J. Sel. Areas Commun.*, vol. 23, no. 2, pp. 201–220, 2005.

[64] I. Akyildiz, W. Lee, M. Vuran, and S. Mohanty, "NeXt generation/dynamic spectrum access/cognitive radio wireless networks: a survey," *Computer Networks*, vol. 50, no. 13, pp. 2127–2159, 2006.

145

[65] T. Yucek and H. Arslan, "Spectrum characterization for opportunistic cognitive radio systems," in *IEEE Military Commun. Conf. (MILCOM)*, Washington, DC, Oct. 2006, pp. 1–6.

[66] M. Pun, M. Morelli, and C. Kuo, "Maximum-likelihood synchronization and channel estimation for OFDMA uplink transmissions," *IEEE Trans. Commun.*, vol. 54, no. 4, pp. 726–736, 2006.

[67] Z. Cao, U. Tureli, and Y. Yao, "Deterministic multiuser carrier-frequency offset estimation for interleaved OFDMA uplink," *IEEE Trans. Commun.*, vol. 52, no. 9, pp. 1585–1594, 2004.

[68] J. van de Beek, M. Sandell, and P. Borjesson, "ML estimation of time and frequency offset in OFDM systems," *IEEE Trans. Signal Process.*, vol. 45, no. 7, pp. 1800–1805, 1997.

[69] R. Fantacci, D. Marabissi, and S. Papini, "Multiuser interference cancellation receivers for OFDMA uplink communications with carrier frequency offset." in *Proc. IEEE Global Telecommun. Conf. (GLOBECOM)*, vol. 5, Dallas, TX, Nov. 2004, pp. 2808–2812.

[70] K. Kim, Y. Han, and S. Kim, "Joint subcarrier and power allocation in uplink OFDMA systems," *IEEE Commun. Lett.*, vol. 9, no. 6, pp. 526–528, 2005.

[71] Z. Cao, U. Tureli, and Y. Yao, "User Separation and Frequency-Time Synchronization for the Uplink of Interleaved OFDMA," in *Proc. IEEE Asilomar Conf. on Signals, Systems and Computers*, vol. 2, Pacific Grove, CA, Nov. 2002, pp. 1842–1846.

[72] P. Moose, "A technique for orthogonal frequency division multiplexing frequency offset correction," *IEEE Trans. Commun.*, vol. 42, no. 10, pp. 2908–2914, 1994.

[73] J. G. Andrews, A. Ghosh, and R. Muhamed, *Fundamentals of WiMAX: Understanding Broadband Wireless Networking.* Prentice-Hall, Feb. 2007.

[74] S. Chiu, "Fuzzy model identification based on cluster estimation," *J. Intelligent and Fuzzy Systems*, vol. 2, no. 3, pp. 267–278, 1994.

[75] R. Yager and D. Filev, "Generation of fuzzy rules by mountain clustering," *J. Intelligent and Fuzzy Systems*, vol. 2, no. 3, pp. 209–219, 1994.

[76] G. Seber, *Multivariate Observations.* John Wiley & Sons, 1984.

[77] H. Spath, *Cluster Dissection and Analysis: Theory, FORTRAN Programs, Examples.* Horwood New York: Halsted Press [distributor], Chichester, 1985.

[78] G. Stuber, J. Barry, S. Mclaughlin, Y. Li, M. Ingram, and T. Pratt, "Broadband MIMO-OFDM Wireless Communications," *Proceedings of the IEEE*, vol. 92, no. 2, pp. 271–294, 2004.

[79] H. Sampath, S. Talwar, J. Tellado, V. Erceg, and A. Paulraj, "A fourth-generation MIMO-OFDM broadband wireless system: design, performance, and field trial results," *Communications Magazine, IEEE*, vol. 40, no. 9, pp. 143–149, 2002.

[80] D. Gesbert, H. Bolcskei, D. Gore, and A. Paulraj, "MIMO wireless channels: capacity and performance prediction," in *IEEE Global Telecommun Conf. (GLOBECOM'00)*, vol. 2, 2000.

[81] *IEEE Standard for Local and Metropolitan Area Networks Part 16*, IEEE Std. IEEE 802.16-2004, 2004.

[82] *IEEE Standard for Local and Metropolitan Area Networks Part 16 (IEEE Std 802.16e-2005)*, IEEE Std., 2005.

[83] F. Ivanek, "Convergence and Competition on the Way Toward 4G: Where are We Going?" in *Radio and Wireless Symposium, 2007 IEEE*, Long Beach, CA, Jan. 2007, pp. 265–268.

[84] K. Lee, "Technology Leaders Forum - Create the Future with Mobile WiMAX," *Communications Magazine, IEEE*, vol. 45, no. 5, pp. 10–14, 2007.

[85] H. Arslan, "Channel Frequency Response Estimation Under the Effect of RF Impairements in OFDM Based Wireless Systems," in *Proc. 64th Vehicular Technol. Conf. (VTC-Fall 2006)*, Montreal, Canada, Sep. 2006, to appear.

[86] H. Arslan and D. Singh, "Establish test procedures for WiMAX Transceivers," *Microwaves & RF*, vol. 45, no. 7, 2006.

[87] M. El-Tanany, Y. Wu, and L. Hazy, "OFDM uplink for interactive broadband wireless: analysis andsimulation in the presence of carrier, clock and timing errors," *Broadcasting, IEEE Transactions on*, vol. 47, no. 1, pp. 3–19, 2001.

[88] S. Alamouti, "A simple transmit diversity technique for wireless communications," *Selected Areas in Communications, IEEE Journal on*, vol. 16, no. 8, pp. 1451–1458, 1998.

[89] A. Hafeez, D. Hui, and H. Arslan, "Interference cancellation for EDGE via two-user joint demodulation," in *Proc. 58th Vehicular Technol. Conf. (VTC-Fall 2003)*, vol. 2, Oct. 2003, pp. 1025 – 1029.

[90] R. Nilsson, F. Sjoberg, and J. LeBlanc, "A rank-reduced LMMSE canceller for narrowband interference suppression in OFDM-based systems," *IEEE Trans. Commun.*, vol. 51, no. 12, pp. 2126–2140, Dec. 2003.

[91] A. Coulson, "Narrowband interference in pilot symbol assisted OFDM systems," *IEEE Trans. Commun.*, vol. 3, no. 6, pp. 2277–2287, Nov. 2004.

[92] Z. Wu and C. Nassar, "Narrowband interference rejection in OFDM via carrier interferometry spreading codes," *IEEE Trans. Commun.*, vol. 4, no. 4, pp. 1491–1505, July 2005.

147

[93] D. Zhang, P. Fan, and Z. Cao, "A novel narrowband interference canceller for OFDM systems," in *Proc. IEEE Wireless Commun. and Network. Conf. (WCNC)*, vol. 3, Mar. 2004, pp. 1426–1430.

[94] X. G. Doukopoulos and R. Legouable, "Intercell interference cancellation for MC-CDMA systems," in *Proc. IEEE Vehic. Technol. Conf. (VTC)*, Dublin, Ireland, Apr. 2007, pp. 1612–1616.

[95] M. Mohaisen and K. H. Chang, "Maximum-likelihood co-channel interference cancellation with power control for cellular OFDM networks," in *Proc. Int. Symp. on Commun. Inform. Technol. (ISCIT)*, Sydney, Australia, Oct. 2007, pp. 198–202.

[96] H. Yoshino and A. Czylwik, "Adaptive co-channel interference (CCI) cancellation for OFDM communication systems," in *Proc. Int. Zurich Seminar on Broadband Commun.*, Zurich, Switzerland, Feb. 2000, pp. 245–250.

[97] P. A. Hoeher, S. B. Hoeher, W. Xu, and C. Krakowski, "Single-antenna co-channel interference cancellation for TDMA cellular radio systems," *IEEE Wireless Commun. Mag.*, vol. 12, no. 2, pp. 30–37, Apr. 2005.

[98] M. Shibahara, T. Fujii, I. Sasase, and T. Saba, "Performance evaluation of adaptive co-channel interference canceling receiver using frequency spread coding and frequency interleaving for OFDM systems," *European Trans. Telecommun.*, vol. 14, pp. 15–24, Jan. 2003.

[99] H. Schoeneich and P. Hoeher, "Iterative semi-blind single-antenna cochannel interference cancellation and tight lower bound for joint maximum-likelihood sequence estimation," *Elsevier Signal Proc.*, vol. 84, no. 11, pp. 1991–2004, 2004.

[100] P. Kaczorek and D. Rutkowski, "A comparison of narrowband and broadband overlay of cellular CDMA on GSM," in *Proc. IEEE Vehic. Technol. Conf. (VTC)*, vol. 3, May 2000, pp. 1859–1863.

[101] R. Sahota and P. Whiting, "On the feasibility of spectrum sharing between GSM and IS-95," in *Proc. IEEE Personal Wireless Commun.*, Mumbai, India, Dec. 1997, pp. 439–443.

[102] I. Guvenc, M.-R. Jeong, F. Watanabe, and H. Inamura, "A hybrid frequency assignment for femtocells and coverage area analysis for co-channel operation," *IEEE Commun. Lett.*, vol. 12, no. 12, pp. 880–882, Dec. 2008.

[103] ECMA International, "High rate ultra wideband PHY and MAC," ECMA-368 Standard, Dec. 2008. [Online]. Available: http://www.ecma-international.org/publications/files/ECMA-ST/ECMA-368.pdf

[104] ——, "High rate 60 GHz PHY, MAC, and HDMI PAL," ECMA-387 Standard, Dec. 2008. [Online]. Available: http://www.ecma-international.org/publications/files/ECMA-ST/ECMA-387.pdf

[105] A. Nasri, R. Schober, and L. Lampe, "Analysis of narrowband communication systems impaired by MB-OFDM UWB interference," *IEEE Trans. Wireless Commun.*, vol. 6, no. 11, pp. 4090–4100, Nov. 2007.

[106] S. M. Mishra, R. W. Brodersen, S. T. Brink, and R. Mahadevappa, "Detect and avoid: an ultra-wideband/WiMAX coexistence mechanism," *IEEE Commun. Mag.*, vol. 45, no. 6, pp. 68–75, June 2007.

[107] P. Ranta, A. Hottinen, and Z.-C. Honkasalo, "Co-channel interference cancelling receiver for TDMA mobile systems," in *Proc. IEEE Int. Conf. Commun. (ICC)*, vol. 1, Seattle, WA, Jun. 1995, pp. 17–21.

[108] H. Schoeneich and P. Hoeher, "Single antenna interference cancellation: iterative semiblind algorithm and performance bound for joint maximum-likelihood interference cancellation," in *Proc. IEEE Global Telecommun. Conf. (GLOBECOM)*, vol. 3, Dec. 2003, pp. 1716–1720.

[109] Y. Kopsinis and S. Theodoridis, "An efficient low-complexity technique for MLSE equalizers for linear and nonlinear channels," *IEEE Trans. Signal Process.*, vol. 51, no. 12, pp. 3236–3248, Dec. 2003.

APPENDICES

150

Appendix A

When BPSK modulation is used, based on (2.18)-(2.26), the mean of $\left|Y_i^{(m)}(k)\right|^2$ can be evaluated as follows

$$
\mathrm{E}\left\{\left|Y_i^{(m)}(k)\right|^2\right\} = \begin{cases} E_{\mathrm{sc},i}\mathrm{E}\left\{I_{2,i}^2(k)\right\}, & \text{if } k \notin \mathbf{\Gamma}_i, \\ E_{\mathrm{sc},i}\left(\mathrm{E}\left\{S_{\mathrm{d},i}^2(k)\right\} + \mathrm{E}\left\{I_{1,i}^2(k)\right\} + \mathrm{E}\left\{I_{2,i}^2(k)\right\}\right), & \text{if } k \in \mathbf{\Gamma}_i, \end{cases}
\tag{A.1}
$$

where,

$$
\mathrm{E}\left\{S_{\mathrm{d},i}^2(k)\right\} = K_{1,i}^2(k) , \quad \mathrm{E}\left\{I_{1,i}^2(k)\right\} = K_{2,i}^2(k) ,
$$
$$
\mathrm{E}\left\{I_{2,i}^2(k)\right\} = \frac{2}{N^2}\sum_{p\in\mathbf{\Gamma}_i, p\neq k} h_i^2(p,k) .
\tag{A.2}
$$

On the other hand, again based on (2.18)-(2.26) (note that (2.19), (2.20) are zero-variance RVs), the variance of $\left|Y_i^{(m)}(k)\right|^2$ can be evaluated as

$$
\mathrm{Var}\left\{\left|Y_i^{(m)}(k)\right|^2\right\} = \begin{cases} E_{\mathrm{sc},i}^2\mathrm{Var}\left\{I_{2,i}^2(k)\right\} , & \text{if } k \notin \mathbf{\Gamma}_i \\ E_{\mathrm{sc},i}^2\left(\mathrm{Var}\left\{I_{2,i}^2(k)\right\} + 4\mathrm{Var}\left\{\mathrm{Re}\left\{S_{\mathrm{d},i}^*(k)I_{1,i}(k)\right\}\right\}\right. \\ \left. + 4\mathrm{Var}\left\{\mathrm{Re}\left\{S_{\mathrm{d},i}^*(k)I_{2,i}(k)\right\}\right\} + 4\mathrm{Var}\left\{\mathrm{Re}\left\{I_{1,i}^*(k)I_{2,i}(k)\right\}\right\}\right), \\ \qquad\qquad\qquad\qquad\qquad\qquad\qquad\qquad \text{if } k \in \mathbf{\Gamma}_i, \end{cases}
\tag{A.3}
$$

151

Appendix A (Continued)

where

$$\mathrm{Var}\big\{I_{2,i}^2(k)\big\} = \frac{4}{N^4}\bigg(\sum_{\substack{p\in\mathbf{\Gamma}_i\\p\neq k}} h_i^4(p,k) + 4\sum_{\substack{p\in\mathbf{\Gamma}_i\\p\neq k}}\sum_{\substack{q\in\mathbf{\Gamma}_i\\q\neq k,q\neq p}} h_i^2(p,k)h_i^2(q,k)\bigg), \qquad (\text{A.4})$$

$$\mathrm{Var}\Big\{\mathrm{Re}\big\{S_{\mathrm{d},i}^*(k)I_{1,i}(k)\big\}\Big\} = K_{1,i}^2(k)K_{2,i}^2(k) \qquad (\text{A.5})$$

$$\mathrm{Var}\Big\{\mathrm{Re}\big\{S_{\mathrm{d},i}^*(k)I_{2,i}(k)\big\}\Big\} = \frac{1}{N^2}K_{1,i}^2(k)\sum_{p\in\mathbf{\Gamma}_i,p\neq k} h_i^2(p,k) , \qquad (\text{A.6})$$

$$\mathrm{Var}\Big\{\mathrm{Re}\big\{I_{1,i}^*(k)I_{2,i}(k)\big\}\Big\} = \frac{1}{N^2}K_{2,i}^2(k)\sum_{p\in\mathbf{\Gamma}_i,p\neq k} h_i^2(p,k) . \qquad (\text{A.7})$$

Similar analysis can be applied to higher-order modulation schemes that have symmetric constellation points with respect to the origin, namely the QPSK, 16-QAM, and 64-QAM, where the constellations are respectively given by

$$\mathcal{M}^{(QPSK)} = \Big\{\frac{[(2\rho-1)+(2\kappa-1)j]\sqrt{E_{\mathrm{sc},i}}}{\sqrt{2}} ,$$
$$\rho = 0,1; \ \kappa = 0,1\Big\}, \qquad (\text{A.8})$$

$$\mathcal{M}^{(16-QAM)} = \Big\{\frac{[(2\rho-3)+(2\kappa-3)j]\sqrt{E_{\mathrm{sc},i}}}{\sqrt{10}} ,$$
$$\rho = 0,1,2,3; \ \kappa = 0,1,2,3\Big\}, \qquad (\text{A.9})$$

$$\mathcal{M}^{(64-QAM)} = \Big\{\frac{[(2\rho-7)+(2\kappa-7)j]\sqrt{E_{\mathrm{sc},i}}}{\sqrt{42}} ,$$
$$\rho = 0,...,7; \ \kappa = 0,...,7\Big\}. \qquad (\text{A.10})$$

Then, using (2.18)-(2.26), it can easily be derived that the mean and the variance of $\left|Y_i^{(m)}(k)\right|^2$ are identical with (A.1) and (A.3) for all the above three constellations of higher-

152

Appendix A (Continued)

order modulation schemes. Hence, the impact of ICI is independent of the modulation order

for constellations that are symmetric with respect to the origin[1].

---

[1]Note that the statistics will change in case different modulation types are used for two consecutive symbols, where one of them is at the end of a certain block and the following symbol is at the beginning of the following block.

Appendix B

$$
\begin{aligned}
P^{(m)}(k) = E_{\mathrm{sc},i} \sum_{l=0}^{L-1} \left|\alpha_i^{(m)}(l)\right|^2 & \left[\left|S_{\mathrm{d},i,l}(k)\right|^2 + \left|I_{1,i,l}(k)\right|^2 + \left|I_{2,i,l}(k)\right|^2 \right. \\
& \left. + 2\mathrm{Re}\Big\{S_{\mathrm{d},i,l}^*(k)I_{1,i,l}(k) + S_{\mathrm{d},i,l}^*(k)I_{2,i,l}(k) + I_{1,i,l}^*(k)I_{2,i,l}(k)\Big\}\right] \\
& + |W(k)|^2 + 2\mathrm{Re}\left\{W^*(k)\sqrt{E_{\mathrm{sc},i}} \sum_{l=0}^{L-1} \alpha_i^{(m)}(l)\Big\{S_{\mathrm{d},i,l}(k) + I_{1,i,l}(k) + I_{2,i,l}(k)\Big\}\right\} \\
& + 2E_{\mathrm{sc},i} \sum_{l_1=0}^{L-2} \sum_{l_2=l_1+1}^{L-1} \alpha_i^{(m)}(l_1)\alpha_i^{(m)}(l_2) \\
& \underbrace{\left[\big(S_{\mathrm{d},i,l_1}(k) + I_{1,i,l_1}(k) + I_{2,i,l_1}(k)\big)\big(S_{\mathrm{d},i,l_2}(k) + I_{1,i,l_2}(k) + I_{2,i,l_2}(k)\big)\right]}_{C_{l_1,l_2}}.
\end{aligned} \tag{B.67}
$$

In a multipath channel, despite some analogies with with the multiuser channel, the statistics of (2.17) will be different than in an AWGN channel. We may re-write (2.17) in a multipath channel as

$$
\begin{aligned}
P^{(m)}(k) = \left|Y^{(m)}(k)\right|^2 &= \left|Y_i^{(m)}(k) + W(k)\right|^2 \\
&= \left|\sqrt{E_{\mathrm{sc},i}} \sum_{l=0}^{L-1} \alpha_i^{(m)}(l) \left\{S_{\mathrm{d},i,l}(k) + I_{1,i,l}(k) + I_{2,i,l}(k)\right\} + W(k)\right|^2,
\end{aligned} \tag{B.1}
$$

where a single-user scenario is considered for analytical tractability. After some manipulation, (B.1) can be written as in (B.67), where other than the last set of terms involving C_{l_1,l_2}, the earlier terms are analogous to the first three terms in (2.17) for the multiuser AWGN channel scenario (i.e., the different MPCs in the multipath channel may be considered as multiuser signals with different delays and attenuations), and their statistics have already been captured through equations (2.18)-(2.30). However, as opposed to the multiuser AWGN channel scenario analogy, the C_{l_1,l_2} term will be non-zero in the multipath channel, since the MPCs corresponding to the same user will be using the same SAS as well

154

Appendix B (Continued)

as the same modulated symbols (as opposed to the last term in (2.17)). The term C_{l_1,l_2} can be expanded for the multipath channel as

$$
\begin{aligned}
&\big(S_{\mathrm{d},i,l_1}(k) + I_{1,i,l_1}(k) + I_{2,i,l_1}(k)\big)\big(S_{\mathrm{d},i,l_2}(k) + I_{1,i,l_2}(k) + I_{2,i,l_2}(k)\big) \\
&= S_{\mathrm{d},i,l_1}(k)S_{\mathrm{d},i,l_2}(k) + S_{\mathrm{d},i,l_1}(k)I_{1,i,l_2}(k) \\
&\quad + S_{\mathrm{d},i,l_1}(k)I_{2,i,l_2}(k) + I_{1,i,l_1}(k)S_{\mathrm{d},i,l_2}(k) + I_{1,i,l_1}(k)I_{1,i,l_2}(k) \\
&\quad + I_{1,i,l_1}(k)I_{2,i,l_2}(k) + I_{2,i,l_1}(k)S_{\mathrm{d},i,l_2}(k) + I_{2,i,l_1}(k)I_{1,i,l_2}(k) \\
&\quad + I_{2,i,l_1}(k)I_{2,i,l_2}(k) \ .
\end{aligned}
\tag{B.3}
$$

In (B.3), only the $S_{\mathrm{d},i,l_1}(k)S_{\mathrm{d},i,l_2}(k)$, $I_{1,i,l_1}(k)I_{1,i,l_2}(k)$, and $I_{2,i,l_1}(k)I_{2,i,l_2}(k)$ terms have a non-zero mean. For example, the first term is equal to

$$
S_{\mathrm{d},i,l_1}(k)S_{\mathrm{d},i,l_2}(k) = \big[X_i^{(m)}(k)\big]^2 K_{1,i,l_1}(k)K_{1,i,l_2}(k)e^{\frac{-j2\pi k(D_{l_1,i}+D_{l_2,i})}{N}}.
\tag{B.4}
$$

If $D_{l_1,i}$ and $D_{l_2,i}$ are considered as known, (B.4) becomes a deterministic variable[1]. Similarly, it may be shown that the other two terms have non-zero means, and it is also straightforward to derive that (B.3) has a non-zero variance. In summary, since the C_{l_1,l_2} terms are non-zero in a multipath channel, there is not a one-to-one analogy between single-user multipath and multi-user AWGN channels, and the former scenario (considering exactly same delays and fading coefficients as in a multiuser AWGN channel) results in worse spectrum opportunities due to larger ICI.

---

[1]If $D_{l_1,i}$ and $D_{l_2,i}$ are considered as random variables that may take any value, on the other hand, the mean of (B.4) would be equal to zero. However, these two variables usually have small values compared to N, and therefore, (B.3) still has a non-negligible mean.

155

ABOUT THE AUTHOR

Mustafa Emin Şahin received his B.S. degree in Electrical and Electronic Engineering from Boğaziçi University, Istanbul, Turkey, in June 2004, and his M.S. degree in Electrical Engineering from the University of South Florida, Tampa, FL, USA, in May 2006. He is a member of the Wireless Communications and Signal Processing Group at University of South Florida and he is working toward his Ph.D. degree. During his Ph.D. study, he has been collaborating with researchers in DOCOMO USA Communications Laboratories, Palo Alto, CA. His research interests include OFDMA-based co-channel femtocells, co-channel interference cancellation in OFDMA, MIMO implementation in WiMAX systems, and spectrum sensing in cognitive radios.